Recent advances in the synthesis, photo-/electrocatalytic properties and applications of MXenes/bismuth-related composites

Dongsheng Li, Guanyu Wang, Yuanfeng Ye, Philippe Boutinaud, Xu Zheng, Jie Xu, Dongzhe Li, Zhiyu He, Wei Huang, Sanshui Xiao, et al.

Recent advances in the synthesis, photo-/electrocatalytic properties and applications of MXenes/bismuth-related composites

Dongsheng Li,[1] Guanyu Wang,[1] Yuanfeng Ye,[1] Philippe Boutinaud,[2] Xu Zheng,[1] Jie Xu,[3] Dongzhe Li,[4] Zhiyu He,[1] Wei Huang,[1] Sanshui Xiao,[5] Fengwen Kang,[1*]

[1] *College of Materials Science and Engineering, Sichuan University, Yihuan Road No. 24 South Section 1, Chengdu 610065, Sichuan, P. R. China*;

[2] *Université Clermont Auvergne, Clermont Auvergne INP, Institut de Chimie de Clermont-Ferrand, 63000 Clermont-Ferrand, France;*

[3] *School of Medical Information and Engineering, Southwest Medical University, Luzhou 646000, P. R. China;*

[4] *CEMES, Université de Toulouse, CNRS, 29 rue jeanne Marvig, F-31055 Toulouse, France;*

[5] *DTU Electro, Department of Electrical and Photonics Engineering, Technical University of Denmark, 2800 Kgs., Lyngby, Denmark.*

***Corresponding authors' Email:**

kangfengwen0597@126.com (F. Kang)

D. Li, **G. Wang**, **Y. Ye**, and *Prof. Dr.* **F. Kang**[*]
College of Materials Science and Engineering, Sichuan University, Chengdu 610065, Sichuan, P. R. China.

Prof. Dr. **P. Boutinaud**,
Clermont Université Auvergne, Clermont Auvergne INP, Institut de Chimie de Clermont-Ferrand, 63000 Clermont-Ferrand, France.

Assoc. Dr. **J. Xu**
School of Medical Information and Engineering, Southwest Medical University, Luzhou 646000, P. R. China.

Dr. **D. Li**
CEMES, Université de Toulouse, CNRS, 29 rue jeanne Marvig, F-31055 Toulouse, France.

Dr. **S. Xiao**
DTU Electro, Department of Electrical and Photonics Engineering, Technical University of Denmark, 2800 Kgs., Lyngby, Denmark.

Abstract

In recent years, many reviews have been made for the design, synthesis, properties, and relevant applications of MXenes and their derivatives, but a systematic overview specifically dedicated to MXenes/bismuth-related composites (*i.e.*, MXenes/Bi-rcs) is still missing. Here we present the recent progress on the design, synthesis, and photo-/electrocatalytic properties of MXenes/Bi-rcs, as well as their applications, aiming to offer new insights and guidance for their future development. We begin by disclosing the synthesis methods of MXenes/Bi-rcs and highlighting the preparation strategies of MXenes that is an important first step in achieving the MXenes/Bi-rcs. Then, we disclose the photo- /electrocatalytic properties and applications of MXenes/Bi-rcs, with a focus of particular concern on the interplay of Bi element with the functional groups of MXenes and for the mechanisms that account for the enhanced photo-/electroactivity and durability. Finally, we show the promising opportunities of MXenes/Bi-rcs associated with the potential challenges of this emerging research branch.

Keywords: MXenes; Bismuth (Bi); MXenes/Bi composites; Photocatalysis; Electrocatalysis

1. Introduction

The successful isolation of two-dimensional (2D) graphene (*i.e.*, the one-atom thin carbon sheet) by Geim *et al*. [1] in 2004 opened the way to the access of many other 2D materials. Beyond 2D graphene and its derivatives, a number of chemical and physical strategies, as exemplarily reviewed by Mannix *et al*. [2] in 2017 and Lu *et al*. [3] in 2020, are now available for obtaining many other 2D materials. As well known, 2D materials feature some basic common structural characteristics that bring about superior, yet unique, chemical reactivity and physical properties [4], including one to a few atoms- or monomer-unit thin thickness, laterally-infinite, and atomically-ordered networks with strong in-plane bonding and weak out-plane bonding [4-7]. As a result, 2D materials can exhibit a variety of optical, optoelectronic, physical, and chemical properties that bulk materials cannot have.

MXenes (to be pronounced "MAXenes"), known as the chemical abbreviation of carbides and nitrides or carbonitrides of transition metals, belong to a new class of "2D materials". The first 2D Ti_3C_2 MXene with graphene-like morphology was reported by Naguib *et al*. [8] in 2011 by extracting the Al atoms from Ti_3AlC_2 through an exfoliation route using hydrofluoric (HF) acid as an etching agent. Since then, more than fifty synthesized compositions and structures, with a variety of outstanding electronic, magnetic, chemical, optical, and photo- /electrocatalytic properties [2, 4-5, 9-10], have been discovered. Special attention, as reviewed by Guan *et al*. [9], has been dedicated to MXenes quantum dots (MQDs) that feature forceful size and quantum confinement effects compared with their 2D counterparts. As an outcome, MXenes and their derivatives were suggested for, *e.g.*, triboelectric energy generators [11], batteries [12], transparent electrodes [13], photo- /electrocatalysts [14-17], supercapacitor [18], biomedicine [19], sensor [20], photodetector [21], additive-free ink [22] *etc*. Although the development history of 2D Ti_3C_2 MXene is young compared to 2D graphene, more than 150 MAX-related compounds and other properties like electronic, physical, electron-phonon coupling, chemical, thermal stability *etc*, have already been predicted, for instance, by Keast *et al*. [23] in 2009, Lofland *et al*. [24] in 2006, and Sokol *et al*. [25] in 2019 based on the first-principles calculations. This to some extent means that the

discovery of MXenes and their derivatives, along with the study of relevant properties and applications is largely underestimated from an experimental viewpoint and will thus continue to be a hot research subject in the future.

Seeking out the archival literature (*i.e.*, reviews, research papers, news, comments, *etc*) from *Thomson Scientific* Web of Science (WOS) with the keyword "MXene" results in huge outputs related (but not limited) to nanotechnology, material science, engineering, photo- /electrochemistry, energy fuels, physics, environmental science, chemistry, optoelectronics, polymer and biological science, crystallography, as well as their subdivisions and multidisciplinary. Noteworthy, it is found that the most popular MXenes are based either on Ti_3C_2 and $Ti_3C_2T_x$ (where T_x is the surface functional group) or on their derivatives. Normally, bulky MXenes always exhibit relatively simple properties due to their relatively simple chemical components (*i.e.*, only two or three elements); thus great efforts and attempts were made to develop composites architectures consisting of bulky MXenes associated with other metals or chemical systems (*e.g.*, $Ti_3C_2T_x$/$NiSe_2$@C [26], $Ti_3C_2T_x$/Sn [27], $Ti_3C_2T_x$/Sn-Ag-Cu [28], $Ti_3C_2T_x$/ZnO [29], Ti_3C_2/MoS_2 [30], Ti_3C_2/$Mn_xCd_{1-x}S$ [31], and Ti_3C_2/TiO_2@C_3N_4 [32]), allowing to reach original, innovative and improved properties. Of special interest are the MXenes/Bi-related composite materials (hereafter abbreviated as MXenes/Bi-rcs) formed by MXenes compounded, for instance, with metallic bismuth (Bi) [33-45, 115], Bi-related oxides [46-92] and non-oxides [93-100], hybrids formed by Bi and other metallic elements (*e.g.*, Na-Bi [101]), and/or other more complex Bi-related compounds, hybrids or composites [39, 102-114, 116-123]. In such MXenes/Bi-rcs, the Bi materials, Bi element or Bi metal play an important role in the applications due to the excellent electronic conductivity and abundant exposed metal sites [20, 124-127], while the MXenes act as an auxiliary material to modify the final output performance.

According to WOS, the first research work dedicated to the synthesis, properties, and applications of MXenes/Bi-rcs was conducted by Cao *et al*. in 2018 [49]. Since then, the research on MXenes/Bi-rcs has been exponentially growing in terms of the number of archival literature and citations (**Figure 1**). Meanwhile, the research scopes (**inset of Figure 1**) combined with the critical development timeline (**Figure 2**) reveal an up-

and-coming development of MXenes/Bi-rcs and the significant and broadening attractiveness of this research branch. However, we can further note from **Tables 1-2** that many MXenes/Bi-rcs were reported for photo- /electrocatalytic purposes, but so far, an overview specifically dedicated to this aspect is still pending. At this stage, disclosing the latest advances on the MXenes/Bi-rcs is useful and necessary to fix the state-of-art in this matter.

In light of the above observations, here we are motivated to make an overview on the recent developments of MXenes/Bi-rcs based on their synthesis methods, photo-/electrocatalytic properties and applications (see **Figure 3**). Specifically, we start this review in **Section 2** with the design consideration of MXenes/Bi-rcs and a summary of the synthesis methods that are reported for preparing MXenes/Bi-rcs. Meanwhile, the advantages, uniqueness and shortcomings of each synthesis method together with the synthetic methods of bulk MXenes and Bi-materials which are an important step in obtaining the MXenes/Bi-rcs, are also introduced in this section. Then, in **Sections 3-4**, we exhibit the photo- /electrocatalytic properties of MXenes/Bi-rcs and their related applications, with a focus of particular concern on the photo- /electroactivities, durability, and interplay of Bi-element, Bi-metal and Bi-compounds with, such as, the functional groups of MXenes. Finally, we summarize this review in **Section 5** and, based on our perspectives and critical thinking, underline some predictable challenges of MXenes/Bi-rcs and possible future developments.

2. Synthesis strategies for MXenes/Bi-rcs

As a part of the MXenes/Bi-rcs, the MXenes component has a deep impact on the formation of MXenes/Bi-rcs, the final output properties and performances, and the relevant practical applications. In general, the role of MXenes in the synthetic process of MXenes/Bi-rcs is to support the adhesion or growth of Bi-materials.

The success of the first MXene (Ti_3C_2) by chemical-etching and Al-extraction from the precursor of Ti_3AlC_2 reported by Naguib *et al*. [8] opened the way to a wide variety of synthesis routes for the MXenes component in the MXenes/Bi-rcs. Depending on the MAX precursors, synthetic routes and experimental conditions like temperature and holding time, these methods, which can be retrieved in the reviews by Dong *et al*. [4] in

2018, Kumbhakar *et al*. [7] in 2021, Guan *et al*. [9] in 2022 and You *et al*. [128] in 2021, and the research articles reported by Dillon *et al*. [129] in 2016, Ma *et al*. [130] in 2021, Xu *et al*. [131] in 2015, Yang *et al*. [132] in 2018 and Wei *et al*. [133] in 2021, include interface-assisted synthesis, hydrofluoric acid etching, molten salt etching, chemical vapor deposition (CVD), and others like the combined electrochemical and urea glass methods (**Tables 1-2**).

The synthesis of MXenes is, in general, the first step towards MXenes/Bi-rcs. The second step involves the preparation of the Bi-based materials (*i.e.*, metals, oxides, hybrids, and composites) and their association with the MXenes. On the other hand, at least two synthetic steps are needed to achieve the MXenes/Bi-rcs. Obviously, it is much more complicated and challenging to obtain MXenes/Bi-rcs than the MXenes or Bi-based materials, because it is necessary to consider the chemical behaviors and the physico-chemical properties of all the used materials, and manage all the possible synergies between them at different scales and especially (but not limited to) the interfacial region, the type and amount of the used reaction solution, the particle size and morphology, the optical and electronic behaviors, *etc*. Therefore, the purpose of the section is to summarize the synthesis strategies that are used for obtaining the MXenes/Bi-rcs. These methods are included in **Tables 1-2**. In a few situations, we will also show the characterization techniques, including X-ray diffraction (XRD), scanning electronic microscopy (SEM), transmission electronic microscopy (TEM), atomic force microscopy (AFM), and energy dispersive X-ray (EDX) spectroscopy.

2.1 Hydrothermal method

Unlike the solid-state reaction and calcination methods that are traditionally used to obtain commercial materials at a large-scale [134], the hydrothermal method is a relatively soft and cost-effective method that ensures complete grain development, controllable particle size and shape, and uniform distribution [135-137]. Meanwhile, this method is also particularly desirable to avoid large-grain growth and the formation of defects /vacancies and impurities [134, 138].

As we learn from **Tables 1-2**, the hydrothermal method is the most frequently-used synthesis strategy for preparing MXenes/Bi-rcs. The synthetic process of Ti_3C_2/$BiVO_4$

composite reported by Sajid *et al.* [65] in 2021 is selected here as a representative illustration. A synoptic description of this process is reproduced, as seen in **Figure 4a**. Specifically, bismuth nitrate $Bi(NO_3)_3 \cdot 5H_2O$ and ammonia metavanadate (NH_4VO_3) were first mixed into nitric acid (HNO_3) and sodium hydroxide solutions. After strong and efficient stirring, the molten mixture was obtained. Then, by adjusting the pH to 2-3, the mixture was transferred into an autoclave for the hydrothermal treatment. Followed by the steps of: (i) washing the as-obtained products with deionized (*i.e.*, D.I.) water and removing the organic and metallic residues with ethanol, and (ii) drying at 80 °C for 6 h, the targeted $Ti_3C_2/BiVO_4$ composite was achieved. The EDX spectrum and SEM images shown respectively in **Figures 4b** and **4c-e** confirm all the elements consisted of $Ti_3C_2/BiVO_4$ and good attachment of $BiVO_4$ on the surface of the Ti_3C_2 MXene. A closer inspection of the SEM images (**Figures 4c-e**) reveals that the Ti_3C_2 MXene contains many non-uniform clusters and forms, after agglomeration with $BiVO_4$, a porous $Ti_3C_2/BiVO_4$. As previously stated by Sajid *et al.* [65], the porosity that develops within this composite is good for boosting the electron transport that enables enhancing the catalytic activity of $BiVO_4$. By use of the hydrothermal reaction method and a mixed solution containing uniformly-dispersed Ti_3C_2 nanosheets and well-dissolved Bi/Mo precursors, Tian *et al.* [139] in 2020 developed a new type of MXene-supported $Bi_2Mo_3O_{12}$ composite ($Ti_3C_2/Bi_2Mo_3O_{12}$). Since an HF solution was used in the etching process of the MAX phase, a large amount of -OH groups were found to be produced onto the Ti_3C_2 surface. Thereby, the Ti_3C_2 MXene featured an excellent hydrophilic character. Besides, the hydrothermal reaction method was also reported by Zhao *et al.* [140] in 2024 to prepare the V_2C/Bi_2O_3 composite from the raw chemicals consisting of flower-like Bi_2O_3 and multilayer 2D V_2C. Notably, this V_2C/Bi_2O_3 not only held a specific surface area larger than bulky V_2C, but also featured heterojunctions, thereby explaining well why such MXenes/Bi-rc had more robust and improved carrier mobility.

Unlike the above MXenes/Bi-rcs that were formed from one MXene and one Bi oxides (which can be called dual-MXenes/Bi-rcs), a hybrid synthesis combining the hydrothermal and calcination methods was developed by Ke *et al.* [110] in 2022 to obtain

the hybridized quaternary Bi_2O_3/C_3N_4-TiO_2-C (BCTC) composite. In such a composite, three precursors $Bi(NO_3)_3 \cdot 5H_2O$, C_3N_4, and Ti_3C_2 were used, and the Ti_3C_2 MXene, as reported by previous works [49, 69, 79, 141-143], was first achieved by etching Al from Ti_3AlC_2 with HF. Such a combined synthesis can be interestingly extended to other MXene/Bi-rcs like Ti_3C_2/Bi_3TaO_7 (that involves the electrostatic adsorption and solvothermal methods) [79] and $Bi_2O_3/C_3N_4/TiO_2$@C (that involves hydrothermal and calcination routes) [110]. This combined strategy is particularly desirable for obtaining the complex multifunctional MXenes/Bi-rcs with complex architecture that cannot be directly achieved by using one type of synthesis method.

2.2 Coprecipitation strategy

Co-precipitation is a very popular method for obtaining materials with regular particle sizes and smooth particle surfaces, such as nanocrystals [144], C-dots [145], 2D materials [146], or multifunctional composites like persistent luminescent materials coupled with photocatalytic materials [134]. The method not only is used as a self-assembly synthesis for obtaining the Bi-precursors and MXenes, but can also be reported for the synthesis of MXene/Bi-rcs (*e.g.*, $Ti_3C_2T_x$/BiNPs in which the NPs denotes nanoparticles [35], Ti_3C_2/Bi_2O_3 [54, 69], $Ti_3C_2/Bi_{0.90}Gd_{0.10}Fe_{0.80}Sn_{0.20}O_3$ [91], and Ti_3C_2/BiFeO$_3$:La,Mn [92]). There are so far, however, only few works involving the coprecipitation method to prepare MXene/Bi-rcs, although this method has the significant advantage to allow the synthesis of MXene/Bi-rcs in one step. Henceforth, small particles with regular distribution of particle size and controllable chemical compositions can be obtained. Although the coprecipitation is similar to the former hydrothermal treatment, it does not need any additional heating step. Taking the $Ti_3C_2T_x$/BiNPs as an example, He *et al.* [35] in 2020 prepared the $Ti_3C_2T_x$ MXene by selectively etching Al from Ti_3AlC_2 in HF solution at room temperature. Then, the targeted composite was obtained following the steps of: (**i**) dispersing 2 mg of $Ti_3C_2T_x$ into 5 mL of ethylene glycol and ultrasonic treatment for 1 h, (**ii**) dissolving 5 mg of $C_6H_5Na_3O_7$ into the dispersed solution, (**iii**) adding $Bi(NO_3)_3 \cdot 5H_2O$ into the mixture and stirring for up to 12 h, (**iv**) adding 0.5 mL of $NaBH_4$ (0.1 M) into the mixture in the step (**iii**) and shaking for 1 h, and (**v**) a final drying in a vacuum oven at 50 °C for 24 h without any further thermal treatment. The

synthesis process is shown in **Figure 5a**. The success of the synthesis was well confirmed by the SEM (**Figures 5b-c**) and TEM images (**Figure 5d**) and relevant EDX elemental analysis (**Figure 5e**). From **Figure 5d**, we note that the BiNPs (the dark dots) feature a non-uniform size with loosely-spaced distance, but they are all well attach to the surface of 2D $Ti_3C_2T_x$ sheets through electrostatic interaction. Besides, we also note from **Figures 5c-d** that the attachment of BiNPs induced a slight change in the $Ti_3C_2T_x$-layered morphology.

2.3 *In-situ* growth

The *in-situ* growth is known to be effective to grow defects /impurities-free materials on a suitable substrate or matrix. The CVD method sometimes falls in the category of *in-situ* growth strategy, and it has been used widely for obtaining ultrathin film like perovskites-typed $MAPbBr_3$ [147], graphene [148], MOFs [149], noble metals [150], CNTs [151], TMDs [152] *etc*. As listed in **Tables 1-2**, several MXene/Bi-rcs were synthesized using an *in-situ* growth method, which include d-Ti_3C_2/Bi [34], Ti_3C_2/Bi_2WO_6 [49], $Ti_3C_2/Bi_2O_2SiO_3$ [50], $Ti_3C_2/TiO_2/BiOI$ [61], $Ti_3C_2T_x/Bi_4Ti_3O_{12}$ [67], Ti_3C_2/2D Bi_2WO_6 [75], $Ti_3C_2T_x$/BiOCl [82], $Ti_3C_2T_x/Bi_2O_3$ [82], $Ti_3C_2T_x/Bi_2S_3$@N-C [153], and MXene/Bi_2S_3 [154]. In fact, *in-situ* growth not only involves pure physical growth but also often covers chemical growth with the help of, such as, *in-situ* hydrothermal solution growth [49, 67, 75, 82-83, 144]. As exemplarily illustrated by the preparation of Ti_3C_2/Bi_2WO_6 composite based on *in-situ* growth [49], the Ti_3C_2 nanosheets were first obtained by etching Al from Ti_3AlC_2 MAX by means of HF solution (**Figure 6a**). Then, the $Bi(NO_3)_3{\cdot}5H_2O$ and a certain amount of Ti_3C_2 nanosheets were added into D.I. water so that the Bi^{3+} ions were electrostatically adsorbed onto the surface of Ti_3C_2 nanosheets to form Bi^{3+}/Ti_3C_2 (solution A). After that, solution A was mixed with a homogeneous solution B formed by dissolving $Na_2WO_4{\cdot}2H_2O$ and Cethyl Trimethyl Ammonium Bromide (CTAB) into 40 mL D.I. water. After a continuous stirring for 1 h, the mixed solution was transferred into a Teflon-lined autoclave, kept at 120 °C for 24 h, and then thoroughly washed with D.I. water and ethanol. The morphology and thickness of Bi_2WO_6 and heterostructured Ti_3C_2/Bi_2WO_6, revealed by the SEM and AFM images and height cutaway view in **Figures 6b-e**, confirm the successfulness of the formation of this 2D/3D MXene/Bi-rcs

by an *in-situ* growth method.

2.4 Others

Besides, a handful of earlier works, as listed in **Tables 1-2**, involve other methods for the synthesis of MXene/Bi-rcs, which include, for instance, one-step electrodeposition (MXene/Sb-Sn-Bi [33]), self-assembly ($Ti_3C_2T_x$/Bi [36], $Ti_3C_2T_x$/$BiVO_4$ [44], Ti_3C_2/BiOBr [58], $Ti_3C_2T_x$/BiOCl [60], Ti_3C_2/BiOBr [81], $Ti_3C_2T_x$/$Cs_2AgBiBr_6$ [93], Ti_3C_2/TiO_2/Bi_2WO_6 [104], PCN/Ti_3C_2/Bi_2MoO_6 [112], Ti_3C_2/Bi_2WO_6/ZnO [113], Ti_3C_2/$BiPO_4$@Ag [119], and $Ti_3C_2T_x$/$Bi_{0.4}Sb_{1.6}Te_3$ [155]), solvothermal (*e.g.*, Ti_3C_2/Bi@BiOI [39], Ti_3C_2/$BiFeO_3$ [56], Ti_3C_2/$Bi_4O_5Br_2$ [62], Ti_3C_2/BiOI [64], $Ti_3C_2T_x$/$Bi_4Ti_3O_{12}$ [67], Ti_3C_2/$BiOCl_{0.25}Br_{0.75}$ [90], and $Ti_3C_2T_x$/(Ti,C)@BiOBr [118]), hydrolysis (Ti_3C_2/Bi_5O_7Br [73]) and alcoholysis (Ti_3C_2/$Bi_4O_5Br_2$ [78]), liquid phase reduction (Ti_3C_2/Bi [78]), solid-state annealing or calcination (V_2C/BiNPs [41], and Ti_3C_2/$Bi_{12}O_{17}Cl_2$ [46]), reflux processing (*e.g.*, Ti_3C_2/BiOBr [41]), and molten-salt flux (C-TiO_2/Bi_4NbO_8Cl [156]) methods. These methods would bring an additional level of flexibility in the choice of a synthesis method to prepare MXenes/Bi-rcs.

3. Photocatalytic properties and applications of MXenes/Bi-rcs

To date, MXene/Bi-rcs have demonstrated great interest in many applications, but they are mainly reported for photo- /electrocatalytic purposes. In fact, this is one of the major reasons why we focus this review on the photo- /electrocatalytic aspects, without involving others. Significantly, the photo- /electrocatalytic applications of MXene/Bi-rcs listed in **Tables 1-2** are all included in the application scopes of bulk MXenes.

The typical photocatalytic applications of MXene/Bi-rcs are disclosed in **Table 1**, which include: (**i**) CO_2 conversion [49-51, 93] and $Cr_{(VI)}$ removal [58, 64, 68]; (**ii**) production of oxygen (O_2) [49], ammonia (NH_3) [72, 81] and hydrogen (H_2) [62, 78, 80]; (**iii**) degradation of gas-phased nitric oxide (de-NO_x) [118]; (**iv**) decomposition of organic materials (*e.g.*, the dyes of bisphenol A (BPA) [39-40], rhodamine B (RhB) [45, 57-59, 61-62, 64, 66-67, 90, 94, 103, 105-106, 108], methylene blue (MB) [53, 59, 105], congo red (CR) [56, 65-66, 91-92, 107], methyl orange (MO) [65, 67], trypan blue (TB) [66], and methyl green (MG) [104]), benzoic acid [47], 2,4-dinitrophenol [58], *p*-nitrophenol [60], medicinal substances (*e.g.*, antipyrine [39], tetracycline and its derivatives [55, 59, 67- 68, 69, 98, 103, 111-112, 114, 116], sodium sulfadiazine

[70], levofloxacin [72, 107, 116], amoxicillin [75], ciprofloxacin [107, 109, 113, 116], sulfamethoxazole [110], and ofloxacin [116]); and (**v**) others (*e.g.*, conversion of organic materials into CO_2 [77]). As indicated by the prefix "photo" in the term "photocatalysis", the related catalytic activity cannot be initiated in the absence of an external light [17, 134, 157-158]. Therefore, the irradiation light sources that are used for sustaining the photocatalytic activities of MXene/Bi-rcs are also compiled in **Table 1**, and they span typically from UV, visible, and to artificial simulated sunlight, opening a flexible selection of light sources for the researchers to reach the targeted photocatalytic applications according to the practical requirement and the MXene/Bi-rc "photocatalytic-towards" materials. Normally, there are three basic steps for a photocatalyst to complete its photocatalytic process. That is, upon irradiation with a suitable light, the photoinduced carriers can be first generated from the Bi-material and then be accumulated on the surface of the MXene who plays the role of an electron acceptor through a heterojunction interface formed between the MXene and Bi-material. The specific photocatalytic properties, mechanisms and applications associated with different MXene/Bi-rcs, along with their respective different and common photocatalytic aspects, have been disclosed below.

3.1 Photocatalytic CO_2 conversion

Four typical MXene/Bi-rcs (*i.e.*, Ti_3C_2/Bi_2WO_6 (TC/BWO), 2D Ti_3C_2/2D $Bi_2O_2SiO_3$ (2D TC/2D BOSO), $Ti_3C_2T_x$/$BiVO_4$ (2D $Ti_3C_2T_x$/2D BVNS) and $Ti_3C_2T_x$/$Cs_2AgBiBr_6$, developed respectively by Cao *et al*. [49], Wang *et al*. [50], Li *et al*. [51], and Zhang *et al*. [93]), were reported for the photocatalytic CO_2 reduction. For the optimal TC/BWO composite (*i.e.*, TB2), the production yield rate of $CO_2 \rightarrow CH_4 + CH_3OH$ under simulated solar irradiation reaches 1.78 $\mu mol \cdot g^{-1} \cdot h^{-1}$ for CH_4 and 0.44 $\mu mol \cdot g^{-1} \cdot h^{-1}$ for CH_3OH, as shown in **Figure 7a(i)** and **Table 1**. Under the same conditions, the total evolution rate of CO_2 into hydrocarbon fuels (*i.e.*, 2.22 $\mu mol \cdot g^{-1} \cdot h^{-1}$ for both CH_4 and CH_3OH) by TB2 amounts to ~4.6 times that (*i.e.*, 0.48 $\mu mol \cdot g^{-1} \cdot h^{-1}$) by the pristine Bi_2WO_6 (TB0) nanosheets. To identify the source of carbon in the reaction products, Cao *et al*. used the gas chromatography-mass spectrometer to detect CH_4 (labeled by ^{13}C and ^{12}C). As shown by the data reproduced in **Figure 7a(ii)**, the reaction products

are all from CO_2 conversion. Differently, the TC/BOSO composite reported by Wang *et al*. [50] contains a Schottky junction [73, 123] and built-in electric field between the Ti_3C_2 and the photoactive BOSO. According to the experimental results compiled in **Figure 7b(i)**, the photocatalytic production yields of CH_3OH and CO as the reduction time of CO_2 extends are continuously increasing, no matter whether the experiments were conducted in the photoactive BOSO or in the TC/BOSO. It produced a yield rate of 17.82 $\mu mol \cdot g^{-1} \cdot h^{-1}$ for CO and 2.07 $\mu mol \cdot g^{-1} \cdot h^{-1}$ for CH_3OH in the case of the optimal TC/BOSO sample (*i.e.*, with a TC:BOSO mass ratio of 2%). which are better than that in the case of the photoactive BOSO material (*i.e.*, 3.45 $\mu mol \cdot g^{-1} \cdot h^{-1}$ for CO and 1.80 $\mu mol \cdot g^{-1} \cdot h^{-1}$ for CH_3OH) and other TC:BOSO mass ratios like 0.5%, 1%, and 4%. These results demonstrate that after being associated with Bi-related materials, the Mxene Ti_3C_2 plays a positive role in enhancing the photocatalytic CO_2 reaction. In addition, the repeated reaction experiments (**Figure 7b(ii)**) revealed good sustainability and repeatability of TC/BOSO towards the photocatalytic CO_2 reduction under simulated solar irradiation.

Unlike the above two situations, the $Ti_3C_2T_x$ Mxenes were used by both Li *et al*. [51] and Zhang *et al*. [93] to fabricate the 2D $Ti_3C_2T_x$/2D BVNS and $Ti_3C_2T_x$/$Cs_2AgBiBr_6$. The photocatalytic yield rates of $CO_2 \rightarrow O_2 + CH_3OH$ by $Ti_3C_2T_x$/BVNS-2 (*i.e.*, the optimized 2D $Ti_3C_2T_x$/2D $BiVO_4$ with a mass of 5 mg for $Ti_3C_2T_x$ and a mass of 0.1 g for $BiVO_4$) and $CO_2 \rightarrow H_2 + CH_4 + CO$ by Ti_3C_2/$Cs_2AgBiBr_6$ are 20.13 and 21.362 $\mu mol \cdot g^{-1} \cdot h^{-1}$, respectively. As shown in **Figures 7c-d(i)** and **Table 1**, these yields are 4.1 and 1.7 times of the photoactive $BiVO_4$ (*i.e.*, 4.92 $\mu mol \cdot g^{-1} \cdot h^{-1}$ for CH_3OH) and $Cs_2AgBiBr_6$ (*i.e.*, 12.415 $\mu mol \cdot g^{-1} \cdot h^{-1}$ that refers to the sum of 0.108 $\mu mol \cdot g^{-1} \cdot h^{-1}$ for CH_4, 8.798 $\mu mol \cdot g^{-1} \cdot h^{-1}$ for CO and 3.509 $\mu mol \cdot g^{-1} \cdot h^{-1}$ for H_2). From these values and the equation describing the CO selectivity = $R(CO) / [R(CO) + R(CH_4) + R(H_2)] \times 100\%$ (hereafter Equation (1)), we evaluate the CO selectivity by the $Cs_2AgBiBr_6$ is ~70.9%. This is greater than that (~52.1%) by the Ti_3C_2/$Cs_2AgBiBr_6$. This can be explained by the fact that upon irradiation with visible light, the electrons are excited from the valence band (VB) of the $Cs_2AgBiBr_6$ to its conduction band (CB), producing the photogenerated electrons. After that, these photogenerated electrons rapidly migrate to

the interface of BVNS/TC, then transfer to the surface of $Ti_3C_2T_x$, and finally get separated from the photogenerated holes. Since these photogenerated holes can be quenched by H_2O to generate O_2, the photogenerated electrons in the $Ti_3C_2T_x$ can largely and effectively react with the adsorbed CO_2 and H_2O to produce the CO, CH_4, and H_2. As calculated by Equation (1), the H_2 and CH_4 selectivity are ~41.8% and ~6.1% for $Ti_3C_2/Cs_2AgBiBr_6$, respectively. They are greater that the selectivity of ~28.2% for H_2 and ~0.9% for CH_4 for the photoactive $Cs_2AgBiBr_6$. Again, this demonstrates benefit of the composite architecture. The scheme depicted in **Figure 7e(iv)** helps to understand the photocatalytic CO_2 reduction mediated by $Ti_3C_2/Cs_2AgBiBr_6$ upon irradiation with visible light. The three other mechanism schemes in **Figure 7e** relate to the photocatalytic processes involving the photoactive Bi_2WO_6, $Bi_2O_2SiO_3$, $BiVO_4$ and $Cs_2AgBiBr_6$. Through these schemes, we can know exactly what roles the photoactive Bi-materials and Mxenes play in the MXene/Bi-rcs, where the photogenerated electrons come from, and where they go finally. In the case of TC/BWO (**Figure 7e(i)**), the photoinduced carriers are generated from BWO, and the role of TC is to act as an electron acceptor for the photocatalytic reaction. Since no signals associated with the photocatalytic products can be detected in the absence of CO_2, photocatalyst, and/or simulated solar irradiation, the photo-induced electrons are concluded to transfer from the BWO to the heterojunction interface of TC/BWO and then accumulate on the surface of TC. In addition, considering the increase of the specific surface area of the photocatalytic MXene/Bi-rcs after introducing the TC, the TC can also play a role in improving the CO_2 adsorption capability prior to its photocatalytic reduction [49]. This, as a matter of fact, is also the possible reason why the TC has a special photothermal conversion characteristic that provides energy to activate the BWO and can largely boost the local photocatalytic reduction of CO_2. Similarly, the energy level diagrams depicted in **Figures 7e(ii-iii)** indicate that the photogenerated electrons can transfer respectively from the photoactive BOSO and BVNS to Ti_3C_2 and $Ti_3C_2T_x$ through the interface of TC/BOSO and $Ti_3C_2T_x$/BVNS, be then accumulated on the surface of Ti_3C_2 and $Ti_3C_2T_x$, and finally react with the adsorbed CO_2 molecules to realize the photocatalytic reduction of CO_2 under a simulated solar lamp irradiation. Besides, we

learn from these energy level diagrams that the CB potentials of the photoactive materials (*i.e.*, BWO in **Figure 7e(i)**, BOSO in **Figure 7e(ii)**, and BVNS in **Figure 7e(iii)**) are more negative than the Fermi level (E_F) of Ti_3C_2 and $Ti_3C_2T_x$. Moreover, we can also note from **Figures 7e(i-iv)**) that the Mxenes (*i.e.*, Ti_3C_2 in TC/BWO and TC:BOSO and the $Ti_3C_2T_x$ in $Ti_3C_2T_x$/BVNS and $Ti_3C_2T_x$/$Cs_2AgBiBr_6$) are all the same, but the photocatalytic CO_2 reduction brings about different by-products (*i.e.*, CH_3OH + CH_4 for TC/BWO, CH_3OH + CO + O_2 for TC/BOSO, CH_3OH + O_2 for $Ti_3C_2T_x$/BVNS, and CH_4 + CO + H_2 + O_2 for $Ti_3C_2T_x$/$Cs_2AgBiBr_6$). From a sustainable viewpoint, the long-term photocatalytic tests of, for instance, 2D $Ti_3C_2T_x$/ 2D BVNS (**Figure 7c(ii)**) and $Ti_3C_2T_x$/$Cs_2AgBiBr_6$ (**Figure 7d(ii)**), reveal that the production yield of the by-products is continuously increased as the reaction time extends and the 2D $Ti_3C_2T_x$/ 2D BVNS recovers its initial photocatalytic activities after three recycled experiments (**Figure 7c(ii)**).

Besides the four above-mentioned works, bulky MXenes and their other (non-Bi) related derivatives have been widely reported for the photocatalytic reduction of CO_2, as seen in the typical reviews made by, for instance, Cao *et al.* [14] in 2024, Li *et al.* [17] in 2024, Tahir *et al.* [159] in 2021, Huang *et al.* [160] in 2020, Li *et al.* [161] in 2021, and Xiang *et al.* [9, 128] in 2021 and 2022, as well as the research literature concerning, such as, the Ti_3C_2/TiO_2 by Low *et al.* [162] in 2018, $CsPbBr_3$/Ti_3C_2 by Zhang *et al.* [163] in 2021, and PDOPA/$Ti_3C_2T_x$ by Gan *et al.* [164] in 2020.

3.2 Production of oxygen (O_2), hydrogen (H_2), and ammonia (NH_3) gases

Efficiently producing gases like O_2, H_2 and NH_3 has become a hot topic with a wide concern in the photocatalytic field, and so do the MXene/Bi-rcs. Gao *et al.* [49] in 2018, Wang *et al.* [50] in 2022, Li *et al.* [51] and Zhang *et al.* [93] in 2022 also observed the photocatalytic production of O_2 gas that results from the oxidization of H_2O molecules mediated using 2D TC/2D BWO, 2D TC/2D BOSO, 2D $Ti_3C_2T_x$/2D BVNS, and $Ti_3C_2T_x$/$Cs_2AgBiBr_6$. Among them, however, only Wang *et al.* [50] quantified the specific production yield of O_2 (*e.g.*, 1.78 $\mu mg \cdot g^{-1}$ by the optimal TC/BOSO-2) upon irradiation with a simulated sunlight lamp for 4 h. Others just mentioned the existence of O_2 after irradiated MXene/Bi-rcs by, such as, simulated sunlight for 2 h upon the CO_2

photoreduction [49], or presented the O_2 as the oxidation product in the schematic mechanisms [51, 93], without the specific quantitative information on the amount of O_2 gas.

Li *et al*. [62] and Xi *et al*. [78] in 2020, as well as Xie *et al*. [80] in 2022 developed the 2D Ti_3C_2/2D $Bi_4O_5Br_2$, 2D Ti_3C_2/2D BiOBr, and Ti_3C_2/Bi_5O_7Br composites for the photoproducing the H_2 gas. As shown in **Figures 8a-c(i)**, the production of H_2 with the optimal Ti_3C_2/Bi_5O_7Br (*i.e.*, TCB4-0.32), Ti_3C_2/BiOBr, and Ti_3C_2/Bi_5O_7Br (*i.e.*, TCB5-10) can be up to 83.5 $\mu mol \cdot g^{-1} \cdot h^{-1}$, 1.34 $mM \cdot g^{-1} \cdot h^{-1}$ and 76.7 $\mu mol \cdot g^{-1} \cdot h^{-1}$, which are ~1.86, ~3.88, and ~1.97 times more efficient than that by bare $Bi_4O_5Br_2$ (*i.e.*, 44.9 $\mu mol \cdot g^{-1} \cdot h^{-1}$), BiOBr (*i.e.*, 0.345 $mM \cdot g^{-1} \cdot h^{-1}$) and Bi_5O_7Br (*i.e.*, 38.9 $\mu mol \cdot g^{-1} \cdot h^{-1}$), respectively. **Figures 8a,c(ii)** disclose the underlying mechanisms proposed for the photoproduction of H_2 gas. The CB potentials (E_{CB}) of Bi-related materials (*i.e.*, -0.89 eV for $Bi_4O_5Br_2$, and -0.86 eV for Bi_5O_7Br) are more negative than the Fermi level (E_F) of MXenes (*i.e.*, -0.53 eV for thin layer-Ti_3C_2, and -0.57 eV for Ti_3C_2), so upon irradiation with visible light, the photo-induced electrons are first excited to the CB of the Bi-related materials from the VB and are transferred to the Ti_3C_2 through an intimate contact at the interface between pristine Bi-related materials and MXenes. This electron transfer is promoted by the electrostatic attraction between Bi^{3+} and the electronegative Ti_3C_2. Given that the E_{CB} potentials of H*/H_2 (*i.e.*, -0.41 eV of H*/H_2 in the energy band structure of Bi_5O_7Br/Ti_3C_2, see **Figure 8c(ii)**), is more positive than the E_{CB} of Bi-related materials, then the photo-induced electrons can react with H*/H_2 on Ti_3C_2 for H_2 evolution. Meanwhile, the holes left in the VB of Bi-related materials like Bi_5O_7Br (right hand of **Figure 8c(ii)**) can be captured and then consumed by CH_3OH. In this frame, the transfer of photo-induced electrons to Ti_3C_2 favors the separation of the photo-induced charge carriers and regulates the electron density at the active sites that cover the surface of Ti_3C_2. This, in turn, accounts for the significantly improved photocatalytic H_2 evolution activity when MXene/Bi-rcs are formed (see **Figure 8a(i)** and the left-hand side of **Figure 8c(i)**). In the case of Ti_3C_2/BiOBr, however, there is no Schottky barrier at the Ti_3C_2-BiOBr interface and the work function of Ti_3C_2 (*i.e.*, -0.09 eV *vs.* NHE) is more negative compared to the CB potentials of BiOBr (**Figure 8b(ii)**).

In this situation, the photo-induced electrons are not allowed to transfer from BiOBr to Ti_3C_2, unlike the two above cases. However, there is a band bending at the depletion layer [165] once the Ti_3C_2/BiOBr composite is formed. This allows the photo-induced electrons at the interface to be more capable of reducing water to photoproduce H_2 due to more negative potentials. In parallel, the reaction of $CH_3OH + H_2O \rightarrow CO_2 + 6H^+ + 6e^- E^0$, denoted by process 3 in **Figure 8b(ii)**, may lead to a higher production of H^+ in the solution, and this can accelerate the photocatalytic H_2 production.

Similarly to the cases of $Ti_3C_2/Bi_4O_5Br_2$ and Ti_3C_2/Bi_5O_7Br, the holes contained in the VB of BiOBr can be transferred to the CB of Ti_3C_2, but the electron transfer from BiOBr to Ti_3C_2 cannot occur because the recombination of photo-generated charge carriers on Ti_3C_2 is not allowed. As a result, the lifetime of the photo-induced charge carriers increases; the separated electrons on the CB of BiOBr reduce either CH_3OH to produce H_2 (process 1) or oxygen to generate superoxide free radicals (process 4). Thereby, it comes out an enhanced photocatalytic oxidization and water splitting and an improved photocatalytic H_2 evolution activity in the Ti_3C_2/BiOBr (**Figure 8b(i)**).

Besides, Zhang *et al*. [93] in 2022 reported that the $Ti_3C_2T_x/Cs_2AgBiBr_6$ composite also promotes the photocatalytic H_2 evolution and can produce a total yield of 8.924 $\mu mol \cdot g^{-1}$ for H_2 after 1 h of photocatalytic CO_2 reduction. This is ~2.59 and 2.54 times the yield of $Ti_3C_2T_x$ (*i.e.*, 3.437 $\mu mol \cdot g^{-1}$) and $Cs_2AgBiBr_6$ (*i.e.*, 3.509 $\mu mol \cdot g^{-1}$), respectively. This means a greater yield of H_2 gas in the $Ti_3C_2T_x/Cs_2AgBiBr_6$ (**Figure 7d**). Going further, these improvements are ascribed to an accelerated absorption of the photo-induced electrons in the CB of $Cs_2AgBiBr_6$ by the $Ti_3C_2T_x$ that can then produce large amounts of H_2 and CH_4 by consuming the water molecules. For the photocatalytic production of NH_3, Chen *et al*. [79] and Fang *et al*. [81] in 2021 prepared the composites of Ti_3C_2/Bi_4O_5Br and Ti_3C_2/BiOBr using solvothermal method and simple electrostatic adsorption coupled with self-assembly route, respectively.

Furthermore, the photoproduction rates of NH_4^+ and NH_3 with 15TCB (*i.e.*, 15wt% Ti_3C_2/Bi_4O_5Br) and 10BTC (*i.e.*, 10wt% BiOBr/Ti_3C_2 fabricated with a theoretical mass ratio of 10wt% for BiOBr to Ti_3C_2) are as high as 277.74 and 234.6 $\mu mol \cdot g^{-1} \cdot h^{-1}$ (**Figure 8d(i)** and **Figures 8e(i-ii)**). They are respectively ~5.44 and ~48.87 times more efficient

than 51.06 μmol·g^{-1}·h^{-1} with pristine Bi_4O_5Br and 4.8 μmol·g^{-1}·h^{-1} with BiOBr. This also means that the MXene/Bi-rcs has led to an improved photocatalytic generation of NH_3. With increasing the mass ratios of Ti_3C_2 to Bi_4O_5Br and BiOBr to Ti_3C_2, the production rates of NH_4^+ and NH_3, as shown in **Figures 8d-e(i)**, experience an initial increase and a subsequent decrease. Based on the positions of the energy band of pristine Ti_3C_2, Bi_4O_5Br, Ti_3C_2/Bi_4O_5Br and Ti_3C_2/BiOBr (**Figures 8d-e(iii)**), the CB maxima values are located at -0.54 V (*vs*. NHE) for Bi_4O_5Br [52] and -0.79 eV for BiOBr [81]. They are thermodynamically favorable for, for instance, the conversion of N_2 to NH_3/NH_4^+ [79]. Because the energy levels of Bi-related materials (right hand of **Figure 8d(iii)** and left hand of **Figure 8e(iii)**) are positioned at higher energy relative to the energy levels of Ti_3C_2, the photoexcited electrons can migrate from the Bi-related materials to the conductive Ti_3C_2 from Bi-materials through a built-in electric field that is generated at the interfaces of the Ti_3C_2 and Bi-materials. Then, a large amount of photoexcited electrons accumulate on the surface of Ti_3C_2, although some amounts are also accumulated around the Fermi energy level (**Figure 8e(iii)**). As a result, an "electron trap" structure can be formed between Ti_3C_2 and Bi-materials, which capture and accumulate the photogenerated electrons. This formed junction is profitable for the reduction of N_2 by cleaving the N≡N bond. Importantly, considering that the MXene/Bi-rcs feature large specific surface area and provide more abundant "reaction sites" than pristine Ti_3C_2 and Bi-materials, the light absorption capacity of the MXene/Bi-rcs can thus be boosted largely in the photocatalytic process, leading to an enhanced photocatalytic production of NH_3 as we show in **Figures 8d-e(ii)**.

Notably, gases other than O_2, H_2, and NH_3 are often detected in the photocatalytic production process of O_2, H_2, and NH_3 gases, and their amounts under the same conditions could be significantly different. For example, the photodegradation of CH_3OH by Ti_3C_2/BiOBr [62] and the photoreduction of CO_2 by Ti_3C_2/Bi_2WO_6 [49] and $Ti_3C_2T_x/Cs_2AgBiBr_6$ [93] photo-produces the mixed gases of CO_2 + H_2, CO + H_2 + CH_4/O_2, and CH_4 + CH_3OH , respectively. Importantly, in terms of the existing works, it seems that the photoproduction of O_2 gas with MXene/Bi-rcs only comes with the photocatalytic evolution of CO_2. Meanwhile, it also seems that even for the MXenes

and their derivatives, there are still few reports dedicated to the photoproduction of O_2 typically when compared to the photoevolution of NH_3 by other photocatalysts like MXene/TiO_2/Co [166], $Ti_3C_2T_x$/TiO_2 [167], CdS@Ti_3C_2 [168], and TiO_2@C/g-C_3N_4 [169].

3.3 Degradation of NO_x (de-NO_x)

Until now, a number of MXenes and their related materials have been reported for the photocatalytic de-NO_x. For example, Hu *et al*. [170] reported a ternary photocatalyst of g-C_3N_4/TiO_2/Ti_3C_2 MXene, and realized a photocatalytic efficiency of the removal of NO as high as 66.3%.

From the research work reported by Hermawan *et al*. [118] in 2021, we learn that the MXene/Bi-rcs (*i.e.*, $Ti_3C_2T_x$/(Ti,C)-BiOBr catalyst) can also be used for removing the gases-phased NO_x pollutants. As shown in **Figures 9a-b**, 1.00 ppm of NO_x gas was used as the initial concentration, and the optimized 0.1$Ti_3C_2T_x$/(Ti,C)-BiOBr sample was irradiated with the light regions of >510 nm, >400 nm, and >290 nm. Under these conditions, >25%, >40%, and >60% of the gas-phased NO_x were converted into less toxic by-products, respectively. These conversion rates exceed those of the pristine BiOBr and P25 (*i.e.*, titania with an average particle size of 25 nm) photocatalysts (see **Figure 9a**) or those obtained using the physically mixed 0.1$Ti_3C_2T_x$/BiOBr and (Ti,C)-BiOBr (**Figure 9b**). Typically, the physically-mixed $Ti_3C_2T_x$/BiOBr, as seen in **Figure 9b**, fails to show an improved photocatalytic NO_x conversion ability compared to BiOBr and (Ti,C)-BiOBr ,and its de-NO_x conversion ability is worse. This means that the physical mixing is not a feasible route relevant to enhance the photocatalytic conversion ability of gas-phased NO_x. In addition, the de-NO_x conversion ability of (Ti,C)-BiOBr is lower than that of the 0.1$Ti_3C_2T_x$/(Ti,C)-BiOBr composite but improved compared to the pristine BiOBr. This suggests the feasibility of the solvothermal route for preparing photocatalytists dedicated to de-NO_x and the importance of improving its photocatalytic performance. Stability and durability tests of 0.1$Ti_3C_2T_x$/(Ti,C)-BiOBr towards NO_x photocatalytic degradation, as reproduced in **Figure 9c**, reveal that there is no severe decrement of the de-NO_x conversion rate even after several cycles of experiments. This confirms the attractiveness and prospect of the $Ti_3C_2T_x$/(Ti,C)-BiOBr for sustaining the long-term stable photodegradation of

poisonous gases-phased NO_x pollutants.

In this situation where Ti_3C_2/Bi_2MoO_6 is used for photodegrading the tetracycline [68], the photogenerated electrons (e^-) and holes (h^+) in Ti_3C_2/(Ti,C)-BiOBr are not involved directly in the de-NO_x process. Instead, the photogenerated electrons (e^-) react with O_2 to form the $O_2^{\bullet-}$ radical, while the photogenerated holes (h^+) react with H_2O to form the $OH^{\bullet-}$ radical. Then, the active-free radicals react with harmful NO_x gas to produce less toxic by-products of NO_3^- and HNO_2. These processes are described in **Figures 9d-e**.

3.4 Degradation of organic dyes

As far as we learn from the database of WOS and the representative compounds listed in **Table 1**, works on the photodegradation of organic materials like dyes take up a large portion of the photocatalytic applications of MXene/Bi-rcs.

3.4.1 Degradation of MO, MG, and MB dyes

Normally, the organic dyes of MO, MG and MB only feature one visible absorption band peaking respectively at 465 nm (**Figures 10a(i-ii)**), 634 nm (**Figures 10b(i-iii)**), and 663 nm (**Figures 10c(i-iii)**). However, when they are placed in the presence of the MXene/Bi-rcs like $Ti_3C_2/Bi_{12}O_{17}Cl_2$ [53], $Ti_3C_2/BiVO_4$ [65], and $Ti_3C_2/TiO_2/Bi_2WO_6$ [104], their absorption intensity decreases as the irradiation time is extended. Meanwhile, the photodegradation rates of these composites always exceed that of pristine Bi-related materials and Mxenes. Specifically, when the MO is photodegraded with, for instance, the $Ti_3C_2/BiVO_4$ under a 300 W Xe lamp irradiation for 130 min (**Figure 10a(iii)**), its degradation rate is 99.1%. This is ~1.91 times that of the rate of the $BiVO_4$ (*i.e.*, 52%) [65]. Although the MG dye shows a photodegradation trend similar to the MO [65, 67] upon exposure to sunlight, their photodegradation rates are significantly different. As presented in **Figure 10b(iv)**, when exposed to sunlight for 80 min, the degradation efficiency of MG in the presence of TiO_2, Bi_2WO_6 (*i.e.*, BWO), and binary Bi_2WO_6-TiO_2 (*i.e.*, BWT, which were prepared by physically mixing the amounts of 10 wt%, 20 wt%, 30 wt% and 40 wt% of TiO_2 with a fixed amount of BWO), amounts to 74%, 86%, 88%, 97%, 78% and 73%, respectively. All these values surpass the degradation rate of photocatalyst-free MG (~11%) in the same irradiation conditions. By coupling the optimal BWT20 with 5 wt% of Ti_3C_2 to form the ternary BWT-Ti_3C_2 (*i.e.*, BWTM05),

the degradation rate of MG reaches 98.5% after 40 min (**Figure 10b(vi)**). This degradation rate is basically comparable to that of BWT20, but only consumes half of the irradiation time. This can be fitted by the pseudo-first-order kinetic equation of $\ln(C/C_0) = kt$ (hereafter Equation (2)), where C_0 and C denote respectively the initial and final concentrations of the MB dye; t is the illumination time and k is the pseudo-first-order reaction rate constant. As a matter of fact, this equation is now widely used to quantify the photocatalytic activity of a photocatalyst. In this study, it was found that the ternary BWTM05 has the highest value of k (*i.e.*, $k = 0.09$ in 40 min), which is not only 2.1 times the binary BWT20 (*i.e.*, $k = 0.09$ in 80 min, **Figure 10b(vi)**) but also 4.3 and 5.5 times the BWO (*i.e.*, $k = 2.1$ in 80 min) and TiO_2 (*i.e.*, $k = 1.6$ in 80 min). Thereby, the improved ability of BWTM05 towards photocatalytic degradation of MG has been well illustrated.

Similarly to MO and MG, the MB placed in the presence of the Ti_3C_2, Bi_2O_3, and Ti_3C_2/Bi_2O_3 [54] and irradiated with visible light shows an absorption depreciation as the photocatalytic reaction time increases to 55 min (**Figures 10c(i-iii)**). No matter the photocatalysts they are placed in and how long the photocatalytic reaction time takes, the absorption peaks are fixed at 664 nm, but the degradation rates of MB with the Ti_3C_2 (31%), Bi_2O_3 (43%), and Ti_3C_2/Bi_2O_3 (80%) after 55 min reaction, are different (**Figure 10c(iv)**). The kinetic rate constant of Ti_3C_2/Bi_2O_3, evaluated from Equation (2), amounts to 0.014 min^{-1} (**Figure 910c(v)**), which is greater than with Ti_3C_2 (*i.e.*, $k = 0.003$) or with Bi_2O_3 (*i.e.*, $k = 0.006$) (**Figures 10c(iv-vi)**). Again, this reveals the superiority of the MXene/Bi-rcs for photodegrading MB.

To the best of our knowledge, the Nb_2CT_x/Bi_2WO_6 heterojunction developed by Cui *et al*. [59] was the first work that involved the MXene/Bi-rc to study the photocatalytic MB degradation. Note that the photocatalytic degradation of RhB was also involved in this work. As shown in **Figures 10d(i-ii)**, the photodegradation efficiency of MB (*i.e.*, 92.7%) and RhB (*i.e.*, 99.8%) in presence of 2wt% Nb_2CT_x/Bi_2WO_6 (*i.e.*,BN-2) reaches respectively 92.7% ($k = 0.0285$ min^{-1}) and 99.8% ($k = 0.072$ min^{-1}) under visible light irradiation for 90 min. This is ~1.3 and ~1.1 times the efficiency of pristine Bi_2WO_6 in the same conditions (*i.e.*, $k = 0.057$ min^{-1} for MB and 0.026 min^{-1} for RhB) (see **Figures**

10d(iii-iv)). This improved photocatalytic performance of Nb_2CT_x/Bi_2WO_6 *vs.* Bi_2WO_6 can be explained based on the mechanism depicted in **Figure 10d(v)**. Similarly to the energy diagrams reproduced in **Figures 8-9**, the CB potential of Bi_2WO_6 is more negative than the E_f of Nb_2CT_x at the Bi_2WO_6-Nb_2CT_x interface. Consequently, the photoinduced electrons (e^-) accumulated at the CB of Bi_2WO_6 can flow to Nb_2CT_x. Additionally, previous works [59, 171] show that the RhB and MB can be degraded by the $^{\bullet}OH$, which can be produced *via* the photoreduction of the $^{\bullet}O^{2-}$ radicals that result from the combination of electrons with O_2 adsorbed at the Nb_2CT_x surface. Meanwhile, the photoinduced holes (h^-) accumulated at the CB of Bi_2WO_6 can, on the one hand, oxidize RhB directly and, on the other hand, oxidize the H_2O to form the $^{\bullet}OH$ radicals that can then degrade the RhB and MB dyes. In this case, as more photoinduced electrons are accumulated at the Nb_2CT_x, more positive charges will be accumulated in the Bi_2WO_6 accordingly. As a result, a space charge layer forms and brings about a Schottky junction at the Bi_2WO_6-Nb_2CT_x interface. Due to this space charge layer, the photogenerated electrons cannot come back from Nb_2CT_x to Bi_2WO_6 [172]. In this frame, the Schottky junction not only captures the photoinduced electrons accumulated at the CB of Bi_2WO_6, but can also delay the electron-hole recombination in Bi_2WO_6.

Unlike the $Ti_3C_2T_x/Bi_2O_3$ [54], Nb_2CT_x/Bi_2WO_6 [59] and $BiOBr/Ti_3C_2/MMT_{ex}$ [105] that involved the photocatalytic degradation of other organic materials like RhB and BA, Cui *et al*. [53], only focused on the photodegradation of Cl-terminated $Ti_3C_2/Bi_{12}O_{17}Cl_2$ (*i.e.*, CTC/BOC) heterojunction on the MB dye. As displayed in **Figure 10e(i)**, the UV-Vis absorption intensity of Cl-terminated Ti_3C_2 (*i.e.*, CTC) is decreased more than the absorption intensity of $Bi_{12}O_{17}Cl_2$ (*i.e.*, BOC), possibly due to the electromagnetic wave absorption ability and local surface plasmon resonance effect [53, 173]. When compared to the BOC, the enhanced absorption intensity, as witnessed by the change of body color from yellow for BOC to black for CTC (see the inset of **Figure 10e(i)**), is observed in the CTC/BOC heterojunction. Meanwhile, the CTC/BOC exhibits a photocurrent density stronger than the pristine BOC and the physically-mixed BOC-CTC (**Figure 10e(ii)**). This indicates that it is more efficient to separate the photoinduced charge carriers in the CTC/BOC composite. Thus, the photodegradation rates of MB with BOC

and BOC-CTC BOC, as expected, are worse than those with CTC/BOC (**Figure 910e(iii)**). Besides, the photodegradation rate constants (k) of the CTC/BOC amount to 9.7 and 3.9 times that of the BOC and of the physically mixed BOC-CTC (**Figure 10e(iv)**), respectively. However, because the Ti_3C_2 used by Cui *et al*. [53] was prepared by Lewis acidic etching method, the Ti_3C_2 is terminated with chlorine groups to form the Cl-terminated Ti_3C_2 (CTC). Owing to the surface grafting of Cl-terminated groups, an intimate interfacial contact forms between BOC and Ti_3C_2 through a "Bi-Cl-Ti" bridge (**Figure 10e(v)**). This is similar to the space charge layer formed in the Nb_2CT_x/Bi_2WO_6 [59]. Moreover, since the Cl-terminated groups also act as a photoinduced electron transport channel [174], the separation and migration rates of the photoinduced holes (h^-) and electrons (e^-) are enhanced. As a result, when the CTC is introduced to couple with BOC to form the CTC/BOC MXene/Bi-rc, an improved photocatalytic activity of the BOC is observed.

3.4.2 Degradation of Rhodamine B (RhB)

The photodegradation of RhB has been the subject of extensive investigations in the photocatalytic field. Similar to the MO, MG and MB, the RhB dye also features an absorption band in the visible spectral range. As we can note from **Figure 11a(i)**, the shape of this absorption band is unchanged upon irradiation with a 300W Xe lamp for 50 min [57], but shows an hypsochromic shift as the irradiation time is raised. As summarized in **Table 1**, the works involving the photocatalytic degradation of RhB by MXene/Bi-rcs [45, 57-59, 60-64, 66-67, 90, 94, 103, 105-106, 108] represent more than half of the total reports. Although the experimental conditions, like the reaction time, are different from each other, the photodegradation efficiency of RhB by most of MXene/Bi-rcs (i.e.,$Ti_3C_2T_x/BiOBr_{0.5}I_{0.5}$ [45], $Ti_3C_2/BiOBr$ [58, 62], Nb_2CT_x/Bi_2WO_6 [59], $Ti_3C_2/TiO_2/BiOI$ [61], $Ti_3C_2/BiOI$ [64], $Ti_3C_2T_x/Bi_2O_2CO_3$ [66], $Ti_3C_2T_x/Bi_4Ti_3O_{12}$ [67], $Ti_3C_2/BiOCl_{0.25}Br_{0.75}$ [90], $TTi_3C_2T_x/Cs_2AgBiBr_6$ [94], $Ti_3C_2/TiO_2/BiOCl$ [103], $BiOBr/Ti_3C_2/MMT_{ex}$ [105], $Ti_3C_2T_x/TiO_2/Bi_2S_3$ [106], and g-C_3N_4/Carbon black/$BiOBr/Ti_3C_2/MoS_2$ [108]), is greater than 90%, and even reaches ≈100% in some cases. For instance, $Ti_3C_2/BiOBr$ [57] (*i.e.*, BTC-8) removes more than 89.3% of RhB upon illumination with the visible light for 50 min. This is greater than that (*i.e.*, 79.5% in **Figure 11a(ii)**) by BiOBr. Such

improvement of the photodegradation rate of RhB is also demonstrated in other dual MXenes/Bi-rcs developed by coupling MXenes with Bi-related materials [45, 58-59, 62, 64, 66-67, 90, 94], and the ternary MXenes/Bi-rcs developed by combining dual MXenes/Bi-rc with the TiO_2 photocatalyst [61, 103, 106] or other materials such as MMT_{ex} (exfoliated montmorillonite) [105] and g-C_3N_4/Carbon [108]. For example, Ke *et al.* [61] reported the ternary MXene/Bi-rc of Ti_3C_2/(001)TiO_2/BiOI (hereafter BTT, and (001) denotes the facet that is involved in the Ti_3C_2 carbonaceous heterojunction). On this ground, the optimized ternary BTT-32 composite, designed by adding 32 mg of (001)TiO_2/BiOI, was demonstrated to degrade >99% of RhB after being exposed to a 500 W Xe lamp for 80 min (**Figure 11b(i)**). The degradation rate, as seen in **Figure 11b(i-ii)**, surpasses that of BiOI, Ti_3C_2, TiO_2 (*i.e.*, P_{25}), (001)TiO_2/BiOI, the hybrids of BiOI/Ti_3C_2 (*i.e.*, BT) and BiOI/TiO_2 (*i.e.*, BTO), and the BTT samples produced with other added amounts of (001)TiO_2/Ti_3C_2.

Similarly to the mechanisms reproduced in **Figures 7-10** and **Figure 12**, the energy level schemes depicted in **Figures 11c-d**) account for the photodegradation process of RhB in the presence of dual Ti_3C_2/BiOBr and ternary Ti_3C_2/(001)TiO_2/BiOI. These composite architectures also contain a Schottky junction. Under light irradiation, the Bi-related materials (*i.e.*, BiOBr [57] and BiOI [61]) are first excited to generate the photogenerated electrons that can then migrate to the Ti_3C_2 due to their narrower bandgap and finally react with O_2 molecule to produce active radical $\bullet O_2^-$ species for the RhB degradation. Typically, Ti_3C_2, once coupled with, for instance, the BiOBr to form Ti_3C_2/BiOBr [57], serves not only as an electron trap but also as shuttling sites that are beneficial for the decrease of the charge recombination at the surface of BiOBr and for the promotion of the charge separation and transfer to the BiOBr. In the case of the Ti_3C_2/TiO_2/BiOI composite, the contact between p-type BiOI and n-type TiO_2 forms a Schottky p-n junction, where the fundamental band edges of TiO_2 are located below those of BiOI. The BiOI absorbs the incoming visible light and generates the charge carriers. Then, the photogenerated electrons migrate to the CB of TiO_2 and transfer to Ti_3C_2 due to its lower work function relative to TiO_2 (**Figure 11d**). The junction that forms between TiO_2 and Ti_3C_2 not only suppresses backward charge diffusion but also

facilitates the separation of photogenerated electron-hole pairs. Meanwhile, it also extends the lifetime of the active electron. All of these are good for generating $\bullet O^{2-}$ when O_2 molecules enter in contact with the Ti_3C_2 surface. These active radical $\bullet O_2^-$ species contribute to the degradation of RhB. On the other side, the photogenerated holes that were left in the VB of BiOI react with RhB and then degrade it. Besides, partial photogenerated holes produced in the Bi-related materials of BiOBr [57] and BiOI [61] also react with RhB, while the remaining holes oxidize H_2O into O_2 but not into •OH.

3.4.3 Degradation of Bisphenol A (BPA) and Congo red (CR) dyes

Two MXene/Bi-rcs of Ti_3C_2/Bi@BiOI and MXeBOTs/Bi@Fe_2O_3 (where the symbol @ indicates a grafting of Bi-related materials onto the surface of another of material) were reported by Gao *et al*. [39] and Lukas *et al*. [40] as novel photocatalysts to degrade respectively the BPA . Specifically, Ti_3C_2/Bi@BiOI was prepared by a solvothermal route, involving typically the removal of Al layers from the Ti_3AlC_2 MAX precursor through an HF solution etching, followed by a dissolution of the Ti_3C_2 dispersion and subsequent drop-by-drop addition of KI of ethylene glycol solution in $Bi(NO_3)_3{\cdot}5H_2O$ solution. In this composite, the Bi^{3+} ions are adsorbed at the surface of Ti_3C_2 by means of effective electrostatic interaction. Differently, the Bi/MXeBOTs were produced by the solid-state annealing method that allows to graft Bi nanoparticles (BiNPs) onto the surface of the V_2C. Then, the Fe_2O_3 NPs were attached to form the composite. The synthesis process is duplicated in **Figure 12a(i)**. When placed in the optimal TCB-10 (*i.e.*, the Ti_3C_2/Bi@BiOI formed by 10% weight ratio of Ti_3C_2), 88.8% of the BPA was photodegraded with a 500 W Xenon lamp for 80 min (**Figure 12a(ii)**). This is 6.8 times the degradation rate of pristine BiOI (13.1%). Fitting with Equation (1) (**Figure 12a(iii)**) produces the degradation rate constant (k) of 0.0261 min^{-1} for TCB-10. This is 18.6 times that of pristine BiOI (0.0114 min^{-1}). While V_2C MXene and Fe_2O_3/V_2C only were demonstrated to degrade only 48% and 56% of BPA upon irradiation with visible light for 60 min, the degradation rate of the BPA with MXeBOTs/Bi@Fe_2O_3 was 97%, thus showing an enhanced photocatalytic BPA removal (**Figure 12a(iv)**).

More concerns have been paid to the photocatalytic removal of organic CR dye using MXene/Bi-rcs like $Ti_3C_2/BiFeO_3$ [56], $Ti_3C_2/BiVO_4$ [65], $Ti_3C_2T_x/Bi_2O_2CO_3$ [66],

Mxene/$Bi_{0.9}Gd_{0.1}Fe_{0.8}Sn_{0.2}O_3$ [91], Ti_3C_2/$BiFeO_3$:La,Mn [92] and Ti_3C_2/Bi_2MoO_6@BiOBr [107]. As for Ti_3C_2/$BiFeO_3$ [56] and Mxene/$Bi_{0.9}Gd_{0.1}Fe_{0.8}Sn_{0.2}O_3$ [91], their composite formation also involves the attachment of Bi-related materials onto the surface of the Mxene (**Figures 12b-c(i)**). This is like the case of MXeBOTs/Bi@Fe_2O_3 [40]. Iqbal *et al*. reported that after being exposed to visible irradiation for 42 min, ~100% of the CR was degraded by the Ti_3C_2/$BiFeO_3$ (*i.e.*, BFO-MXENE). Comparatively, only ~33% of the CR was removed with pure $BiFeO_3$ (*i.e.*, BFO) (see **Figure 12b(ii)**). Noteworthy, the Ti_3C_2/$BiFeO_3$, as shown in **Figure 12b(iii)**, sustains its photocatalytic capability after four cyclic experiments. The Mxene/$Bi_{0.9}Gd_{0.1}Fe_{0.8}Sn_{0.2}O_3$ developed by Tariq *et al*. [91] using coprecipitation was demonstrated to remove ~100% of the CR after exposed to visible light for 120 min. This photocatalytic degradation efficiency, as expected, is better than with pure MXene (~80%). Note that the control test without irradiation appears as the black line in **Figure 12b(iii)**. This enhanced photocatalytic performance was also observed in Ti_3C_2/$BiFeO_3$:La,Mn [92] (*i.e.*, BLFO/Ti_3C_2, **Figure 12d(i)**) and Ti_3C_2/$BiVO_4$ [65] (**Figure 12d(ii)**). Similarly to the case of Ti_3C_2/$BiFeO_3$, there is no obvious depreciation of the degradation rate in Ti_3C_2/$BiVO_4$ after three runs of the experiment (see **Figure 12d(iii)**), thereby showing the great potential of these MXene/Bi-rcs as photocatalysts for the removal of the CR dye. The mechanisms involved in the photocatalytic removal of the CR with these MXene/Bi-rcs are quite similar to each other. As exemplified in **Figures 12b-c(i)**), when this MXene/Bi-rc is exposed to visible light, electrons (e^-) and holes (h^+) that can interact respectively with O_2 by a reduction reaction and H_2O by oxidation reaction to produce free radical ions like $\bullet O_2^-$ and OH^- [56, 65, 91-92, 107], are formed. These radicals are highly reactive species for photodegrading the CR from water and producing harmless by-products like CO_2 and H_2O.

3.5 Degradation of medicinal substances

Besides the above organic molecules, tetracycline and its derivatives [55, 59, 67-69, 98, 103, 111-112, 114, 116] are often used to evaluate the photodegradation of MXene/Bi-rcs. For example, the photocatalytic removal rate of tetracycline placed in the Ti_3C_2/Bi_2MoO_6

heterojunction [68], as shown in **Figure 13a**, is up to 99% upon irradiation with a 50 W LED light for 30 min. This is much higher than with Bi_2MoO_6 (~37%) in the same conditions. In addition, the same Ti_3C_2/Bi_2MoO_6 composite was also demonstrated for the photoreduction of Cr(VI). As shown by the C_t/C_0 intensity change in **Figure 13b**, the UV-vis absorption intensity decreases as the photocatalytic reaction time increases (**Figure 13c**). Moreover, the Ti_3C_2/Bi_2O_3 composite developed by Lai *et al*. [69] in 2021, was reported for the photodegradation of tetracycline. Similarly, the pristine Bi_2O_3, as indicated in **Figure 13d**, only degrades 14% of tetracycline upon illumination with the visible light for 90 min, whereas the removal rate related to Ti_3C_2/Bi_2O_3 reaches 82% in the same conditions. Further, this composite placed in different wastewater was shown to sustain respectively >76% and ~70 % of its initial degradation rate after four repeated experiments (**Figures 13e-f**). These results demonstrate the stability and practicability of the Ti_3C_2/Bi_2O_3 composite towards the tetracycline photodegradation. Besides, as disclosed in **Table 1**, we also realize that the MXene/Bi-rcs can be used for photodegrading other medicinal substances including antipyrine [39], sodium sulfadiazine [70], levofloxacin [72, 107, 116], amoxicillin [75], ciprofloxacin [107, 109, 113, 116], sulfamethoxazole [110], and ofloxacin [116], although their photodegradation effects are greatly dependent on the type of medicinal substances and MXene/Bi-rcs, and the experimental conditions.

4. Electrocatalytic properties and applications of MXenes/Bi-rcs

Mxenes and their derivatives have been widely reported for electrocatalytic purposes, but we only found seven works associated with the electrocatalytic performances of MXene/Bi-rcs. Their amounts are few as compared with the MXene/Bi-rcs-related photocatalysis. All these were reported in the last two years and concerned nitrogen reduction reaction (NRR) or hydrogen evolution reaction (HER). This new research branch leaves an open and exciting room for future developments.

4.1 Properties and applications of NRR

The electrocatalytic performances of MXenes/Bi-rcs can typically be assessed by means of UV-vis absorption spectra, the analysis of which enables determining the resulting by-products like indophenol assays with NH_4^{4-} and N_2H_4 produced during the

electrocatalytic process of $Ti_3C_2T_x$/BiNPs [36]. Normally, MXenes possess their own NRR activity, but in the MXenes/Bi-rcs, they usually serve as the support or substrate to load the Bi-related materials like metallic BiNPs, Bi oxides and Bi hybrids or composites. The large specific surface area of MXenes exposes more electrochemically active surface areas and sites, which can thereby allow, for instance, $Ti_3C_2T_x$/BiOCl [82] to have specific capacitance larger than pristine BiOCl or $Ti_3C_2T_x$ and limit well aggregation of Bi-related materials. An additional advantage of MXenes/Bi-rcs is related to the formation of strong interaction between the Bi 6*p* band and the N 2*p* orbitals, as revealed by Wang *et al*. [82] and Zhang *et al*. [83], as well as the theoretical DFT calculations by Luo *et al*. [95]. This restrains the HER activity of MXenes and consequently improves the competing NRR activity of this composite. The other advantage is that MXenes, as reported by Wang *et al*. [82] in $Ti_3C_2T_x$/BiOCl and Li *et al*. [175] in $Ti_3C_2T_x$/Bi composites, favor rapid electron mobility of Bi-related materials during the electrochemical NRR process because of their excellent metallic character. The third advantage is that MXenes prevent the structure of MXenes/Bi-rcs to change during the electrochemical NRR process. In **Table 2**, We have collected the electrochemical NRR properties of MXenes/Bi-rcs.

It must be noted that the mechanisms and analysis of MXenes/Bi-rcs towards NRR, as reported by Yu *et al.* [36], Liu *et al.* [38], Wang *et al.* [82] and Akir *et al* [41], are based on the experimental data. In particular, their approach do not involve theoretical aspects and do not take into account the influence of defects /vacancies generated in MXenes, Bi-related materials and/or MXene/Bi-rcs during the NRR activity. In fact, the NRR mechanisms that are discussed in these reports are based on MXenes rather than on the MXene/Bi-rcs. For example, the electrocatalytic mechanism proposed for the hydrogenation of nitroarenes over the sponge-confined Bi/$Ti_3C_2T_x$ [36] was established by referencing that of Au/Fe_3O_4 and PtO_2/ZnO catalysts that were developed respectively by Yang *et al.* [176] in 2018 and Zhang *et al.* [177] in 2020 for the reduction of 4-nitrophenol to 4-aminophenol. Clearly, there is no direct relationship between the sponge-confined Bi/$Ti_3C_2T_x$ and the two electrocatalysts. Additionally, the raw reagents used for illustrating the NRR activity and the “electrocatalytic NRR toward” products

were also different from each other. The 4-nitrophenol was selected for the Au/Fe_3O_4 and PtO_2/ZnO catalysts, while the 4-nitroaniline (4-NA) was used for the Bi/$Ti_3C_2T_x$. In this case, it should not directly force the mechanisms of Au/Fe_3O_4 and PtO_2/ZnO to explain the NRR process of Bi/$Ti_3C_2T_x$.

As a step beyond, Zhang *et al*. [83] and Luo *et al*. [95] carried out DFT calculations to identify the NRR chemical reaction path in $Ti_3C_2T_x$/Bi_2O_3 and $Ti_3C_2T_x$/Bi_2S_3, and evaluate the free energy of intermediates corresponding to the Bi-related materials (*i.e.*, Bi_2O_3 and Bi_2S_3). It should be, however, noted that the works done by Luo *et al*. and Zhang *et al*. were published in 2022 and 2023, respectively, but the manuscript submitted by Zhang *et al*. was Oct.-2022, which is late a year of time compared to that (Jul.-2021) by Luo *et al*. In view of this, we first introduce the NRR chemical reaction mechanism that was used for illustrating the the conversion of NO_3 to NH_3 in the $Ti_3C_2T_x$/Bi_2O_3 system. In this NRR (*i.e.*, an abbreviation of "nitrate reduction") process, the authors proposed the Gibbs free energy change diagram on the (-112) crystal plane of Bi_2O_3 by means of the DFT calculations (**inset of Figure 14b**) and demonstrated that this plane is the dominated crystal plane and contains the dominant active sites for nitrate adsorption and electroreduction. In other word, nitrate is more inclined to convert ammonia with the ONH pathway on the (-112) plane /surface of Bi_2O_3. However, the energy barrier (*i.e.*, 2.17 eV) of HER, which was evaluated by the DFT calculations, is greater than the DFT-calculated energy generating *ONH_2 and/or *NOH. This indicates the suppression of HER by Bi_2O_3. Moreover, they also show that the hydrogenation of *NO contained two possible pathways (the NOH and ONH pathways, as shown in **Figure 14b**). The reaction pathway of *ONH → *ONH_2 (*i.e.*, pathway (**1**)) involves an energy barrier of 0.42 eV (the rate-determined-step of ONH pathway); while the reaction pathway of *NO → *ONH (pathway (**2**)) involves an energy barrier of 1.32 eV (the rate-determined-step of NOH pathway).

However, the work reported by Zhang *et al*. [83] did not consider the possible defects /vacancies that are generated in MXenes, Bi-related materials and/or MXene/Bi-rcs, but this was done by Luo *et al*. [95] in 2022 who employed the DFT calculations to evaluate the impact of S-vacancies on the electronic structure of $Ti_3C_2T_x$/Bi_2S_{3-x} composite and,

thereby, to reveal the observed NRR activities ("**4.2 Electrocatalysis**" section) and relevant NRR chemical reaction pathway. The DFT calculations come out that the $Ti_3C_2T_x/Bi_2S_{3-x}$ feature S-vacancy formation energy (E_v) of 1.26 eV, which is lower than that (2.43 eV) of pristine Bi_2S_{3-x} without the $Ti_3C_2T_x$ substrate (**Figure 14c(i)**). This indicates that the formation of S-vacancies in the $Ti_3C_2T_x/Bi_2S_{3-x}$ is much easier than that in pristine Bi_2S_{3-x}. Moreover, the work function that was calculated by DFT for $Ti_3C_2T_x$ (5.256 eV), as shown in **Figures 14c(ii-iii)**, is much higher than that of bare Bi_2S_3 (*i.e.*, 4.007 eV), meaning that the electrons spontaneously flow from Bi_2S_3 to $Ti_3C_2T_x$ after that the $Ti_3C_2T_x/Bi_2S_3$ composite is formed. Consequently, the electrons transported from Bi_2S_3 to $Ti_3C_2T_x$ promote the formation of abundant S-vacancies on $Ti_3C_2T_x/Bi_2S_{3-x}$ by lowering their formation energy. As we can note from differential charge density and relevant electron location function (see **Figures 14c(vi-v)**), a considerable amount of electrons are accumulated both at the S-vacancy sites and at the interface region of $Ti_3C_2T_x/Bi_2S_{3-x}$. These S-vacancies and interface are preferentially involved to serve as the electron-trapping centers for N_2 adsorption and activation. Besides, the enhanced conductivity of $Ti_3C_2T_x/Bi_2S_{3-x}$, as reflected by the density of states (DOS) and confirmed by the DFT-calculated NRR activities (**Figures 14c(vi)-d**), accelerates the charge transfer and boosts the catalytic kinetics of NRR. In terms of the optimized structural change of N_2 adsorption on the Bi site of $Ti_3C_2T_x/Bi_2S_3$ and the S-vacancy and interfacial Bi sites of $Ti_3C_2T_x/Bi_2S_{3-x}$, the calculated adsorption of N_2 on Bi site shows a very small N-N elongation (1.115 Å) and negligible Bi-to-$^*N_2$ electron transfer (-0.02 |e|) (**Figure 14d(i)**). These results therefore demonstrate the weak adsorption and activation of N_2 in the S-vacancy-free $Ti_3C_2T_x/Bi_2S_3$. Such situation can, however, be reversed when there is one S-vacancy in the $Ti_3C_2T_x/Bi_2S_{3-x}$ and N_2, as seen in **Figure 14d(ii)**, can be trapped and stored in the S-vacancy site where $^*N_2$ is bonded with three surrounding Bi atoms. In particular, the Bi-to-$^*N_2$ electron transfer (-0.37 |e|) and N=N bond elongation (1.276 Å) in the $Ti_3C_2T_x/Bi_2S_{3-x}$ are larger compared to (*i.e.*, -0.02 |e| for Bi-to-$^*N_2$, and 1.115 Å for N-N bond) of $Ti_3C_2T_x/Bi_2S_3$. This demonstrates the improvement of N_2 adsorption on the S-vacancy site. Besides, the strong $^*N_2$-Bi electronic interactions (-0.29 |e|) coupled with the large N=N bond

stretching (1.223 Å) reveal that N_2 is also adsorbed on the Bi atom at the $Ti_3C_2T_x$-Bi_2S_3 interface. This enables an electron transfer from interfacial Bi atoms to adsorbed N_2 (**Figure 14d**(**iii**)).

By combining DFT calculations and experimental results, Luo *et al*. proposed Gibbs free energy diagrams to analyze and discuss the possible chemical reaction path of NRR in the $Ti_3C_2T_x/Bi_2S_{3-x}$ composite. Two calculations were achieved depending on whether N_2 is adsorbed at the S-vacancy site or at interfacial Bi site. In both cases, two pathways, as depicted in **Figures 14d**(**iv-v**), were considered. In the former situation, an exothermic hydrogenation process was demonstrated for the $*N_2 \rightarrow *NH$ step that releases energy of 0.12 eV. At this stage, an alternating mode and the hydrogenation of $*NHNH_2$ into $*NH_2NH_2$ come, with a reduced energy barrier (RDS) of 1.15 eV due to the enhanced NRR activity over the S-vacancy site. In the second situation, however, the interfacial Bi site reduces the energy barrier (0.71 eV) in the step of $*N_2 \rightarrow *NH$, in which the energetically favored distal pathway shows the rate-determining step for the fifth hydrogenation step of $*N \rightarrow *NH$ with 1.24 eV uphill (**Figure 14d**(**v**)). This means that the NRR process in the $Ti_3C_2T_x/Bi_2S_{3-x}$ composite is an energetic-favorable process over the interfacial-B site. Thus, it comes that the NRR process of $Ti_3C_2T_x/Bi_2S_{3-x}$ features a dual-active-center mechanism, in which both S-vacancy and interfacial-Bi sites serve as active centers to activate the $*N_2$ synergistically, stabilize the $*N_2H$, and jointly reduce energy barriers for efficient NRR. Significantly, such improved NRR activity predicted by the DTF calculations is consistent with the improved conversion yield rate of $N_2 \rightarrow NH_3$ and FE as reproduced in **Figures 17g-h**.

With the NRR properties and relevant mechanisms based either on the experimental results or on the DFT calculations, we can note that in the existing six research works, the NRR process involves continuous proton-electron pairs that interact with N_2 [41]. However, different NRR raw reagents in the presence of different MXene/Bi-rcs often lead to different NRR properties and different mechanisms. Besides, we should also realize that when compared with MXenes and their other derivatives, there still lacks sufficient theoretical DFT works specially performed for studying the NRR process of MXene/Bi-rcs. In this case, here we reproduce a lot of DFT calculations pioneered by

Luo *et al*. [95], hoping that it attracts the researcher's significant attention to establish a reliable mechanism to reveal the intrinsic working principle of the NRR activities in the MXene/Bi-rcs.

In 2021, Yu *et al*. [36] prepared a monolithic catalyst (*i.e.*, $Ti_3C_2T_x$/Bi) *via* an initial photo-assisted deposition of BiNPs onto the surface of the $Ti_3C_2T_x$ and a subsequent electrostatic self-assembly between the negatively charged $Ti_3C_2T_x$/Bi and a positively charged sponge. The synthesis process is reproduced in **Figure 15a**. The SEM images shown in **Figure 15b(i)** confirm the formation of the sponge-confined $Ti_3C_2T_x$/Bi composite. The catalytic capability of this composite was assessed by catalyzing $NaBH_4$ during the transformation of 4-nitroaniline (4-NA) into p-phenylenediamine (PPD). The sponge-confined 1.0%$Ti_3C_2T_x$/Bi composite basically completes the transformation of the 4-NA into PPD within 6 min (**Figure 15c(i)**, while pristine Bi only converts 58.21%. This is an obvious electrocatalytic capability enhancement that can be explained by the fact that the $Ti_3C_2T_x$ strengthens the conversion of Bi towards the reduction of 4-NA. The 1.0%$Ti_3C_2T_x$/Bi/sponge composite, as revealed by the fitted pseudo-first-order kinetic in **Figure 15c(ii)**, features the greatest reaction rate constant of 0.41 min^{-1}, amounting to three times that of pristine Bi. Under the same experimental conditions, a sponge-confined Bi-1.0% reduced-graphene oxide (rGO) composite prepared by the same method converts ~80.6% of 4-NA to PPD (**Figure 15c(iii)**), which is ~20% less with respect to the sponge-confined 1.0%$Ti_3C_2T_x$/Bi composite. Moreover, compared to the rGO-based composite, the sponge-confined 1.0%$Ti_3C_2T_x$/Bi also demonstrated excellent catalytic sustainability and durability, as revealed by ten cyclic conversion tests of 4-NA, 3-NA and 2-NA with ten recyclable experiments (**Figures 15d(i-iii)**). The sponge-confined Bi-1.0% rGO composite, however, showed an electrocatalytic activity depreciation as the cyclic experiments increase, which is ascribed to the loss of Bi-1.0% rGO (see the body color change of samples in **Figures 15b(ii-iii)**).

One year later (*i.e.*, 2022), Liu *et al*. [38] developed a simple liquid phase reduction procedure to obtain the Ti_3C_2/BiNPs composite by depositing metallic BiNPs on the Ti_3C_2 nanosheets (**Figure 16a**). We can learn from the relevant SEM and TEM images

(**Figure 16b**) that the nanocomposites feature an irregular flocculent structure due to the metallic BiNPs distributed within the interlayers and at the outer surfaces of Ti_3C_2 (**Figure 16(ii)**). The morphology of such an architecture differs greatly from the loosely arranged accordion-like configuration of Ti_3C_2 Mxene (**Figure 16b(i)**). With regard to the electrocatalytic performance of the Ti_3C_2/BiNPs composite towards the conversion of N_2 to NH_3 (**Figure 16c**), a maximum conversion rate as high as 28.3 $\mu g \cdot h^{-1} \cdot cm^{-2}$ was obtained in correspondence with a Faraday Efficiency (FE) of 27.2% at -0.4 V *vs*. RHE (*i.e.*, the abbreviation of reversible hydrogen electrode). As known, one of the feasible routes for the sustainable synthesis of NH_3 is the electrocatalytic conversion reaction of N_2. Moreover, we can also learn from **Figure 16d** that the $N_2 \rightarrow NH_3$ conversion rates and the FE fluctuated little with the increase of the number of cycled experiments, indicating good stability of the Ti_3C_2/BiNPs composite.

Also in 2022, Wang *et al*. [82] used an *in-situ* hydrothermal growth of BiOCl on the $Ti_3C_2T_x$, and successfully achieved the BiOCl-modified $Ti_3C_2T_x$ (*i.e.*, $Ti_3C_2T_x$/BiOCl) with microstructural morphologies similar to that of $Ti_3C_2T_x$/BiNPs (**Figures 17a-b**). At the best catalytic potential (*i.e.*, -0.10 V *vs*. RHE), the $Ti_3C_2T_x$/BiOCl composite coated on carbon cloth (hereafter CC) electrocatalytically converts N_2 to NH_3 with a maximum yield rate of 4.06 $\mu g \cdot h^{-1} \cdot cm^{-2}$ and a FE of 11.98% (**Figures 17c-d**), which is ~3.9 and ~1.8 times more efficient than pristine BiOCl/CC (1.05 $\mu g \cdot h^{-1} \cdot cm^{-2}$) and $Ti_3C_2T_x$/CC (2.26 $\mu g \cdot h^{-1} \cdot cm^{-2}$), respectively. Similarly to the Ti_3C_2/BiNPs composite, the $Ti_3C_2T_x$/BiOCl/CC composite, as seen in **Figures 17e-f**, also features excellent electrochemical sustainability and repeatability. Still in 2022, Luo *et al*. [95] prepared the $Ti_3C_2T_x/Bi_2S_{3-x}$ composite and demonstrated a $N_2 \rightarrow NH_3$ conversion yield rate of 68.3 $\mu g \cdot h^{-1} \cdot mg^{-1}$ at -0.6 V and FE as high as 22.5% at -0.4 V, which are all far better than pristine Bi_2S_3 and bulky $Ti_3C_2T_x$ (**Figures 17g-h**). The durability test as shown in **Figure 17i**, did not show obvious depreciation of the $N_2 \rightarrow NH_3$ conversion yield rates and FEs, indicating the good electrochemical stability and sustainability of the $Ti_3C_2T_x/Bi_2S_{3-x}$ composite.

In the year of 2023, Zhang *et al*. [83] and Akir *et al*. [41] used the *in-situ* hydrothermal growth, facile hydrothermal and solid-state annealing methods to prepare 2D

$Ti_3C_2T_x/Bi_2O_3$, 2D V_2C/2D $BiVO_4$, and 2D V_2C/0D BiNPs by associating Bi_2O_3 $BiVO_4$, and BiNPs with $Ti_3C_2T_x$ and V_2C Mxenes (**Figures 18-19a**), respectively. In the case of $Ti_3C_2T_x/Bi_2O_3$, $Bi(NO_3)_3$ was used as the Bi^{3+} source that is adsorbed onto the surface of 2D $Ti_3C_2T_x$ *via* electrostatic attraction. The TEM and HAADF-STEM images of this so-formed composite confirm that the original 2D $Ti_3C_2T_x$ structure was maintained, while the element mapping results revealed the uniform distribution of the Bi, O, Ti, C, and F elements (**Figures 18a-c**). By conducting in an H-type cell using a conventional three-electrode system under ambient conditions and then detecting the reactant and products (nitrate, nitrite and ammonia) with colorimetric method, the 11% Bi_2O_3/MXene composite exhibited the maximum current density (**Figure 18d**), nitrate removal amount (~430.00 $mg \cdot L^{-1}$) (**Figure 18e**), and ammonia formation rate (~7.00 $mg \cdot h^{-1} \cdot cm^{-2}$) and FE (~91.1%) at -1.8 V (*vs*. SCE) (**Figure 18f**). Extending the reaction time results in the gradual decrease of the concentration of nitrate and the gradual increase of the concentration of ammonia (**Figure 18g**), with sustaining the concentration of toxic NO_2 at a relatively low level. Similarly to the FE for ammonia of different electrodes (**Figure 18f**), by increasing the applied potential from -1.4 to -2.2 V (*vs*. SCE) (**Figure 18h**), the FE of ammonia experiences a volcano-shaped process, with a maximum FE value of ~91.1% at -1.8 V (*vs*. SCE), while the ammonia formation rate continuously increases. In addition, both the ammonia yield rate and FE were almost completely restored after 6 cycles of stability experiments tested at -1.8 V (**Figure 18i**), indicating the excellent durability of this 11% Bi_2O_3/MXene composite for electrocatalytic NITR.

For the 2D V_2C/2D $BiVO_4$ and 2D V_2C/0D BiNPs composites, their formation was directly confirmed by the SEM and TEM images reproduced in **Figures 19b-c**. As **Figure 19b**(**i**) shows, the $BiVO_4$ featured flaky morphology, with uniformly wrapping onto the V_2C sheets. It is clearly evidenced by the TEM image in **Figure 19b**(**ii**) that the so-formed $V_2C/BiVO_4$ composite consisted of 2D ultrathin nanosheets. For the 2D V_2C/0D BiNPs composite, the V_2C Mxenes maintained well the layered structure, with the BiNPs spread over the surface of V_2C sheets (**Figure 19c**). Although the two works reported by Zhang *et al*. [83] and Akir *et al*. [41] were all conducted in an H-cell for

measuring NRR, the ammonia production rates and FE values, as seen in **Table 2**, were different from each other. The 2D V_2C/0D BiNPs composite produced the highest NH_3 yield rate (~88.6 $\mu g \cdot h^{-1} \cdot cm^{-2}$) and FE value (~8%) at -0.5 V (*vs*. RHE) (**Figures 19d-e**). These values are all greater than the highest NH_3 yield rate (40.5 $\mu g \cdot h^{-1} \cdot cm^{-2}$) and FE value (5.45%) obtained with 2D V_2C/2D $BiVO_4$ and the highest NH_3 yield rate (46.8 $\mu g \cdot h^{-1} \cdot cm^{-2}$) and FE value (3.4%) obtained with pristine 2D V_2C. Moreover, we reproduce the chronoamperometric results (**Figure 19f**) of 2D V_2C/0D BiNPs that were tested at -0.5 V (*vs*. RHE in N_2-saturated KOH aqueous solution) for 24 h. The obtained data show a very steady current density, sustaining 90.5% of the initial NH_3 yield rate, and an almost unchanged FE.

At this stage, we wish to highlight the nice NRR results reported by Hu *et al*. [42] in December 15, 2023. They developed an electrode by using Bi/$Ti_3C_2T_x$ composite and demonstrated an NRR specific capacity of 68.5 $mAh \cdot g^{-1}$ at a current density of 1 $A \cdot g^{-1}$. Besides, here we also wish to emphasize that the ammonia FE reached a maximum *vs.* potential in *refs*. [36], [41], [82], and [83], but this situation is not seen in *ref*. [95]. In this report, the FE increased continuously upon raising the potential (see the purple curve in **Figure 18g**), without having a maximum value. There is to date no clear, however, understanding of this discrepancy, which means that further experimental and theoretical works are, in this concern, highly welcomed. To date, the use of MXenes/Bi-rcs for the NRR is still limited to the above six works, but considering the short history of its development, the attractiveness of MXene/Bi-rcs towards electrocatalytic NRR will surely motivate researchers to go deeper in this field.

4.2 Properties and applications of HER

As previously studied by Liu *et al*. [38], Akir *et al*. [41], Wang *et al*. [82], and Zhang *et al*. [83], the electrocatalytic HER is the main competitive reaction of NRR. In this concern, suppressing or limiting the HER activity during the NRR process is a critical factor to obtain low overpotentials, high yield rates of NH_3, and high FE values. Coming back to the ammonia yield rates and FE values that were obtained by Liu *et al*. [38] with Ti_3C_2/BiNPs (**Figure 17c**), by Wang *et al*. [82] with $Ti_3C_2T_x$/BiOCl (**Figure 17c**), and by Akir *et al*. [41] with V_2C/BiNPs (**Figures 19d-e**), we can see that when the applied

potential is more negative than a certain applied voltage (*vs*. RHE or SCE), the HER gradually and dominantly competes with NRR. This trend is clearly evidenced when the potentials (*vs*. RHE) exceeds, for instance, -0.4 V with Ti_3C_2/BiNPs, -0.1 V with $Ti_3C_2T_x$/BiOCl, and -0.5 V with V_2C/BiNPs. Here, it is worth noting that the research work conducted by Liu *et al*. [38] is the first work that realized high production rate of ammonia with bismuth-based materials at a potential of -0.1 V. Additionally, due to the competitive HER, the yield rate of NH_3 and FE value increased as the applied potentials became more positive. However, we can learn from **Figure 18g** that the applied potentials dependent ammonia yield rate and FE value of $Ti_3C_2T_x/Bi_2O_3$ [83] are different from that of Ti_3C_2/BiNPs [38], V_2C/BiNPs [41], and $Ti_3C_2T_x$/BiOCl [82]. With increasing the applied potentials from -1.4 V to -2.2 V (*vs*. SCE), the ammonia formation rate continuously increases, but the FE experiences a volcano-shaped curve, showing its maxima (~91.1%) at -1.8 V. The applied potentials dependent FE values for different products (**Figure 20a**) reveal that this is due to the fact that the reduction current is insufficient to meet the requirement of the NRR process with eight electrons transfer when the voltage is more positive than -1.8 V. In other words, the HER is pronounced gradually when the applied voltage is more negative than -1.8 V.

To the best of our knowledge, only Akir *et al*. [41] have introduced the MXene/Bi-rc relayed catalytic HER. Other MXene/Bi-rc related works involving, for instance, $Ti_3C_2T_x$/BiNPs [36], Ti_3C_2/BiNPs [38], V_2C/BiNPs [41], $Ti_3C_2T_x$/BiOCl [82], $Ti_3C_2T_x/Bi_2O_3$ [83], and $Ti_3C_2T_x/Bi_2S_{3-x}$ [95], did not show the HER activity, otherwise than mentioning the word "HER or hydrogenation" occurring in the NRR process when hydrogen containing chemical groups like (**i**) *OH, *NOH, *ONH, $*ONH_2$, *NHOH, $*ONH_3$, $*NH_2OH$ and $*NH_2$ for reducing NO_3^- to NH_3 on the (-112) crystal plane of Bi_2O_3 in $Ti_3C_2T_x/Bi_2O_3$ [83], and (**ii**) $*N_2H$, *NHNH, $*N_2H_2$, *NH, $*NHNH_2$ and $*NH_2NH_2$ in $Ti_3C_2T_x/Bi_2S_{3-x}$ [95], were involved. Obviously, these chemical groups are not H_2 gas.

For H_2 gas, it is a worldwide used carbon-free energy material that has played a vital role in industry, agriculture, and energy storage. A variety of Mxenes and other metal-based derivatives beyond MXene/Bi-rcs, such as those associated with the metals (*e.g.*, Cu [179], Cu [179], Co [180], Pd [181], Pt [182]) and non-metals (*e.g.*, N [183], S [184] *etc*), are

now available for HER. Meanwhile, many works it have proved that both NRR and HER can appear in a given Mxene or Mxene-based derivatives. However, only scarce reports relate to MXenes/Bi-rcs for electrocatalytic HER. The works conducted by Yu *et al*. [36] and Wang *et al*. [82] involved "hydrogen" in the word "hydrogenation" and HER, but did not show any specific HER-related experimental or theoretical results. In this concern, the first report was of Zhang *et al*. [83] in 2023. This work, with that of Akir *et al*. [41] at the end of 2023, represents the only two reports related to the application of MXenes/Bi-rcs towards electrocatalytic HER. We learn from Zhang *et al*. [83] that HER was demonstrated by $Ti_3C_2T_x/Bi_2O_3$, and it pronounced gradually once the voltage was more negative than -1.8 eV (**Figure 20a**). However, no detailed descriptions of HER was provided. Differently, Akir *et al*. studied the electrocatalytic HER activity by use of V_2C/BiNPs and $V_2C/BiVO_4$ composites [41]. As displayed in **Figure 20b**, the $V_2C/BiVO_4$ operated at 10 $mA \cdot cm^{-2}$ features an overpotential of 384 mV, and shows a greater HER performance than V_2C/BiNPs (663 mV) and pristine V_2C (823 mV). In comparison to the Tafel slope of V_2C/BiNPs (173 $mV \cdot dec^{-1}$) and pristine V_2C (204 $mV \cdot dec^{-1}$), the lower Tafel slope (160 $mV \cdot dec^{-1}$) of $V_2C/BiVO_4$ (**Figure 20c**) reveals that the Volmer-Heyrovsky mechanism governs the HER process in the $V_2C/BiVO_4$ composite and the Volmer step is the rate-determining step [185-186]. Meanwhile, in comparison to the current measured for pristine V_2C (**Figure 20d**) and V_2C/BiNPs (**Figure 20f**), the higher current measured for $V_2C/BiVO_4$ (**Figure 20e**) reveals that more accessible active sites that are advantageous for HER activity are created after the hydrothermal synthesis of $V_2C/BiVO_4$. Besides, the smaller arc radius of $V_2C/BiVO_4$ displayed in **Figure 20g** also indicates faster charge transfer at the electrode /electrolyte interface, which leads to an enhanced HER performance. These results reveal that BiNPs have a negative effect on HER, but favor the competing NRR to increase the ammonia yield. Importantly, the double layer capacitance (C_{dl}) of $V_2C/BiVO_4$, as shown in **Figure 20h**, is 6.66 $mF \cdot cm^{-2}$, surpassing that of V_2C/BiNPs (C_{dl} = 3.23 $mF \cdot cm^{-2}$) and that of pristine V_2C (C_{dl} = 1.56 $mF \cdot cm^{-2}$). This is attributed to the fact that the larger specific surface area (SSA) of the 2D V_2C/2D $BiVO_4$, compared to V_2C/BiNPs and pristine V_2C, offers more accessible active sites for the HER and

diffusion of electrocatalytic active species. At last, Akir *et al*. [41] also studied the influence of the time on the applied potential (V *vs.* RHE) (*i.e.*, chronopotentiometry test) by using $V_2C/BiVO_4$, and found that the low voltage increased over 8 h at a constant current density of 10 $mA \cdot cm^{-2}$ operation (**Figure 20i**). This, combined with the undamaged multilayer structural appearance reflected by the SEM images before and after the HER stability test (**Figure 19b**, and the **inset of Figure 20i**), reveals their long-term stability and high structural sustainability towards electrocatalytic HER.

Since the HER related works are all reported in 2023, one can therefore understand why there are still no available reviews specifically dedicated to the recent progress of MXenes/Bi-rcs towards HER.

5. Conclusion and perspectives

Since the first discovery of MXene in 2011 by Naguib *et al*. [16], it has been just +13 years, but the last decade has witnessed significant advances in both the fundamental understanding and practical applications of MXenes and their derivatives. Still, the MXenes and their derivatives have now become an indispensable part of the "2D materials" family. Importantly, with the unprecedented development of design and synthesis methods such as the preparation methods reported by Chen *et al*. [188] (*i.e.*, supercritical etching method for the large-scale manufacturing of MXenes), Ding *et al*. [189] (*i.e.*, Chemical scissor-mediated structural editing for layered transition metal carbides), and Wang *et al*. [190] (*i.e.*, direct synthesis and chemical vapor deposition for 2D carbide and nitride MXenes), advanced characterization techniques, and *ab initio* calculations, as well as more and more *in-depth* study in, such as, the covalent functionalization of MXenes [191] with other chemical groups, the type and number of MXenes-related materials, compounds, and composites, along with their new properties and applications, will certainly continue to be increased in the future. With this context, here we disclosed the comprehensive review specifically focused on the development of the synthesis, photo- /electrocatalytic properties, and applications of MXenes/Bi-rcs. We first summarized the primary synthetic methods of bulk MXenes, with focusing on those that are the first step for the MXenes/Bi-rcs. Then, we showed the design consideration and the reported preparation strategies of MXenes/Bi-rcs, among which

the advantages, uniqueness, shortcomings, characteristics and principles of each synthesis method were also disclosed. After that, we reviewed the photo-/electrocatalytic properties and applications of MXenes/Bi-rcs, which include but not limited to: photocatalytic CO_2 conversion and $Cr_{(VI)}$ removal, photoproduction of O_2, NH_3 and H_2, de-NO_x, photodecomposition of organic materials and medicinal substances, as well as NRR and HER. Besides, we can also conclude from this review that the formation of MXenes/Bi-rcs usually improves the photo- /electrocatalytic properties and performances of bulky MXenes or Bi-related materials towards better applications.

However, coming back to the WOS data shown in **Figure 1**, the current research in the MXenes/Bi-rcs just started in 2018 and there are only three works at that time, which means that this research branch are still its fancy and thus leaves a timely and vast playground for studying sophisticated and/or hitherto unnoticed aspects in this emerging area towards MXenes/Bi-rcs. For example, most previous works would like to concentrate on studying the properties and emerging applications of MXenes/Bi-rcs, without an *in-depth* involvement in device characteristics analysis. This means that they are still in "academic study" status at the present time, being far from the practical applications of MXenes/Bi-rcs. In addition, the theoretical explanation and the mechanism construction of the observed photo- and electrocatalytic properties are still very limited in the MXenes/Bi-rcs. Moreover, it is well known that the thickness of 2D materials has a significant impact on their properties and performances, but it seems that such consideration still have not been involved in the MXenes/Bi-rcs. Noted here that the study of the influence of the 2D thickness on the performances of MXenes have been studied by some previous works. In this case, it is necessary to take into account this aspect in the future research. Furthermore, we should also know that it is impossible for a review work to cover everything, and so does this review. For the present review work, it is very the truth that this is the first time to disclose the recent developments of the MXenes/Bi-rcs with specifically focusing on the photo-/electrocatalysis. Besides, several works have demonstrated the potential applications of MXenes/Bi-rcs in other emerging fields like photodetectors (*e.g.*, $Ti_3C_2T_x/Cs_3Bi_2I_9$

[192]), biosensors (*e.g.*, CaF_2@Ag@Bi_2Te_3/$Ti_3C_2T_x$ [193]) and/or nanomedicine (*e.g.*, Ti_3C_2/$BiVO_4$ [194]), but they are not included in the present review work, because we would like to focus this review on the MXenes/Bi-rcs. Last but not the least, as listed in **Tables 1-2**, the majority of MXene/Bi-rcs were obtained by growing Bi-materials on the surface of MXenes in a suitable solution. This makes the control difficulty in the MXene-related terminal groups and the properties of MXene/Bi-rcs accordingly. Obviously, a lot of challenging work still remain on the MXene/Bi-rcs, but we believe that as more and more scientists with different backgrounds in different fields pay more and more attention to the MXenes/Bi-rcs, more and more new synthesis routes, along with the related previously-unnoticed properties and emerging applications of MXenes/Bi-rcs, will be explored and discovered, not limited to the existing reported aspects. In a word, the MXenes/Bi-rcs will continue to be active and therefore show a bright future.

Declaration of Competing Interest

The authors declare they have no known competing financial interests or personal relationships that can influence the work we reported.

Acknowledgment

Prof. Dr. F. Kang financially thanks for the support of the European Union's Seventh framework programme (FP7) and Horizon 2020 research and innovation program (H2020, grant no. 609405) under the Marie Sklodowska-Curie grant (grant no. 713683) (COFUNDfellowsDTU), the "Double Hundred Talent" project and "the Fundamental Research Funds for the Central Universities".

References

[1] Novoselov K. S., Geim A. K., Morozov S. V., Jiang D., Zhang Y., Dubonos S. V., Grigorieva I. V., Firsov A. A., *Science*, **2004**, 306, 666-669.

[2] Mannix A. J., Kiraly B., Hersam M. C., Guisinger N. P., *Nat. Rev. Chem.*, **2017**, 1, 0014.

[3] Lu Z. Y., Neupane G. P., Jia G. H., Zhao H. T., Qi D. C., Du Y. P., Lu Y. R., Yin Z. Y., *Adv. Funct. Mater.*, **2020**, 30, 2001127.

[4] Dong R. H., Zhang T., Feng X. L., *Chem. Rev.*, **2018**, 118, 6189-6235.

[5] Chhowalla M., Liu Z. F., Zhang H., *Chem. Soc. Rev.*, **2015**, 44, 2584-2586.

[6] Lv R., Robinson J. A., Schaak R. E., Sun D., Sun Y. F., Mallouk T. E., Terrones M., *Acc. Chem. Res.*, **2015**, 48, 56-64.

[7] Kumbhakar P., Gowda C. C., Mahapatra P. L., Mukherjee M., Malviya K. D., Chaker M., Chandra A., Lahiri B., Ajayan P. M., Jariwala D., Singh A., Tiwary C. S., *Mater. Today*, **2021**, 45, 142-168.

[8] Naguib M., Kurtoglu M., Presser V., Lu J., Niu J. J., Heon M., Hultman L., Gogotsi Y., Barsoum M. W., *Adv. Mater.*, **2011**, 23, 4248-4253.

[9] Guan C., Yue X. Y., Fan J. J., Xiang Q. J., *Chinese J. Catal.*, **2022**, 43, 2484-2499.

[10] Li K. N., Zhang S. S., Li Y. H., Fan J. J., Lv K. L., *Chinese J. Catal.*, **2021**, 42, 3-14.

[11] Wyatt B. C., Rosenkranz A., Anasori B., *Adv. Mater.*, **2021**, 33, 2007973.

[12] Ming F. W., Liang H. F., Huang G., Bayhan Z., Alshareef H. N., *Adv. Mater.*, 2020, 33, 2004039.

[13] Chen J. X., Li Z. L., Ni F. L., Ouyang W. X., Fang X. S., *Mater. Horiz.*, **2020**,7, 1828-1833.

[14] Cao J. -M., Zatovsky I. V., Gu Z. -Y. , Yang J. -L., Zhao X. -X., Guo J. -Z., Xu H. Y., Wu X. -L., *Prog. Mater. Sci.*, **2023**, 135, 101105.

[15] Jiang J. Z., Zou Y. L., Arramel, Li F. Y., Wang J. M., Zou J., Li N., *J. Mater. Chem. A*, **2021**, 9, 24195-24214.

[16] Morales-García Á., Calle-Vallejo F., Illas F., *ACS Catal.*, **2020**, 10, 13487-13503.

[17] Li D. S., Zheng X., Boutinaud P., Hu Y. H., Xiao S. S., Xu J., Wang C. L., Hou Y. D., He Z. Y., Huang W., Kang F. W., *Responsive Mater.*, **2024**, Accepted paper // DOI: 10.1002/rpm.20240015.

[18] Hu M. M., Zhang H., Hu T., Fan B. B., Wang X. H., Li Z. J., *Chem. Soc. Rev.*, **2020**, 49, 6666-6693.

[19] Lin H., Chen Y., Shi J. L., *Adv. Sci.*, **2018**, 5, 1800518.

[20] Hantanasirisakul K., Gogotsi Y., *Adv. Mater.*, **2018**, 30, 1804779.

[21] Xu H., Ren A. B., Wu J., Wang Z. M., *Adv. Funct. Mater.*, **2020**, 30, 2000907.

[22] Zhang C. F., McKeon L., Kremer M. P., Park S., Ronan O., Seral-Ascaso A., Barwich S., Gogosti Y., Nicolosi V., *Nat. Commun.*, **2019**, 10, 1795.

[23] Keast V. J., Harris S., Smith D. K., *Phys. Rev. B*, **2009**, 80, 214113.

[24] Lofland S. E., Hettinger J. D., Meehan T., Bryan A., Finkel P., Gupta S., Barsoum M. W., Hug G., *Phys. Rev. B*, **2006**, 74, 174510.

[25] Sokol M., Natu V., Kota S., Barsoum M. W., *Trends Chem.*, **2019**, 1, 210-223.

[26] Yuan Z. X., Guo H. N., Huang Y. K., Li W. Q., Liu Y. F., Chen K., Yue M. Y., Wang Y. J., *Chem. Eng. J.*, **2022**, 429, 132394.

[27] Wu Z. Y., Zhu S., Bai X. G., Liang M., Zhang X., Zhao N. Q., He C. N., *Electrochim. Acta*, **2022**, 407, 139916.
[28] Xu L. M., Shi X. L., Xue Y. W., Zhang K. P., Huang Q. P., Wu C. H., Ma J., Shu J. P., *J. Mater. Eng. Perform.*, **2023**, 32, 1275-1291.
[29] Hou C. L., Yu H. Z., *Chem. Eng. J.*, **2021**, 407, 127192.
[30] Xu X. M., Guo T. C., Hota M. K., Kim H., Zheng D. X., Liu C., Hedhili M. N., Alsaadi R. S., Zhang X. X., Alshareef H. N., *Adv. Mater.*, **2022**, 34, 2107370.
[31] Jiang Z. M., Chen Q., Zheng Q. Q., Shen R. C., Zhang P., Li X., *Acta Phys. -Chim. Sin.*, **2021**, 37, 2010059.
[32] He F., Zhu B. C., Cheng B., Yu J. G., Ho W. K., Macyk W., *Appl. Catal. B -Environ.*, **2020**, 272, 119006.
[33] Tian Y., An Y., Xiong S., Feng J., Qian Y., *J. Mater. Chem. A*, **2019**, 7, 9716-9725.
[34] Zhu X. L., Liu B. C., Li L., Wu L. S., Chen S. J., Huang L., Yang J. K., Liang S., Xiao K. K., Hu J. P., Hou H. J., *Microchim. Acta*, **2019**, 186, 776-783.
[35] He Y., Ma L., Zhou L. Y., Liu G. H., Jiang Y. J., Gao J., *Nanomaterials*, **2020**, 10, 866-876.
[36] Yu C. Q., Peng L. F., Zhu Y. S., Xie G. S., Wu Z. J., Xie X. Q., Zhang N., *J. Mater. Chem. A*, **2021**, 9, 19847-19853.
[37] Zhang Y., Xu Y., Gao L., Liu X., Fu Y., Ma C., Ge Y., Cao R., Zhang X., Al-Hartomy O. A., Wageh S., Al-Ghamdi A., Algarni H., Shi Z., Zhang H., *Mater. Today Phys.*, **2021**, 21, 100479.
[38] Liu A. M., Liang X. Y., Zhu H. D., Ren X. F., Gao L. G., Gao M. F., Yang Y. N., Li G. X., Ma T. L., *Chemcatchem*, **2022**, 14, e202101683.
[39] Gao P., Zhang Z. J., Feng L., Liu Y. Z., Du Z. W., Zhang L. Q., *Chem. Eng. J.*, **2021**, 426, 130764.
[40] Dekanovsky L., Huang H., Akir S., Ying Y. L., Sofer Z., Khezri B., *Small Methods*, **2023**, 7, 2201547.
[41] Akir S., Azadmanjiri J., Antonatos N., Děkanovský L., Roy P. K., Mazánek V., Fomekong R. L., Regner J., Sofer Z., *Nanoscale*, **2023**, 15, 12648-12659.
[42] Hu F., Wei J. H., Shen X., Chen L., Wang Z. M., Peng X., Lv C. L., Ouyang Q. Y., *J. Alloy. Compd.*, **2023**, 968, 171902.
[43] Gong S. Q., Liu H. B., Zhao F., Zhang Y. N., Xu H. T., Li M., Qi J. J., Wang H. H., Li C. L., Peng W. C., Fan X. B., Liu J. P., *ACS Nano*, **2023**, 17, 4843-4853.
[44] Zhao F., Zhang Y. N., Gong S. Q., Xu H. T., Qi J. J., Wang H. H., Li C. L., Peng W. C., Liu J. P., *J. Colloid Interf. Sci.*, **2023**, 652, 2139-2146.
[45] Li Z. R., Wang P. L., Liang Z. H., Wang D. Y., Nie Y. X., Ma Q., *Anal. Chem.*, **2023**, 95, 9706-9713

[46] Hu A. G., Zhou D., Shi Y. Q., Xiao Z. B., *J. Power Sources*, **2024**, 592, 233921.
[47] Sun Z. C., Amrillah T., *Nanoscale*, **2024**, 6, 5079-5106.
[48] Sattar K., Tahir R., Huang H. B., Akinwande D., Rizwan S., *Carbon*, **2024**, 221, 118931.
[49] Cao S. W., Shen B. J., Tong T., Fu J. W., Yu J. G., *Adv. Funct. Mater.*, **2018**, 28, 1800136.
[50] Wang K., Wang Q. P., Zhang K. J., Wang G. H., Wang H. K., *J. Mater. Sci. Technol.*, **2022**, 124, 202-208.
[51] Liang Li L.,Yang Y., Zhou B. Y., Zhou Y., Zou Z. G., *Mater. Lett.*, **2022**, 306, 130937.
[52] Shi X., Wang P. Q., Lan L., Jia S. L., Wei Z. Y., *J. Mater. Sci.-Mater. El.*, **2019**, 30, 19804-19812.
[53] Cui S. S., Liu X., Shi Y. B., Ding M. Y., Yang X. F., *Rare Met.*, **2022**, 41, 2405-2416.
[54] Munir S., Baig M. M., Zulfiqar S., Saif M. S., Agboola P. O., Warsi M. F., Shakir I., *Ceram. Int.*, **2022**, 48, 21676-21689.
[55] Zhao D. X., Cai C., *Mater. Chem. Front.*, **2019**, 3, 2521-2528.
[56] Iqbal M. A., Tariq A., Zaheer A., Gul S., Ali S. I., Iqbal M. Z., Akinwande D., Rizwan S., *ACS Omega*, **2019**, 4, 20530-20539.
[57] Liu C., Xu Q. X., Zhang Q. F., Zhu Y. S., Ji M. W., Tong Z. W., Hou W. H., Zhang Y., Xu J. G., *J. Mater. Sci.*, **2019**, 54, 2458-2471.
[58] Huang Q. S., Liu Y. T., Tao Cai T., Xia X. N., *J. Photoch. Photobio. A*, **2019**, 375, 201-208.
[59] Cui C., Guoa R. H., Xiao H. Y., Ren E. H., Song Q. S., Xiang C., Lai X. X., Lan J. W., Jiang S. X., *Appl. Surf. Sci.*, **2020**, 505, 144595.
[60] Wang C. J., Shen J., Chen R. G., Cao F., Jin B., *Appl. Surf. Sci.*, **2020**, 519, 146175.
[61] Ke T., Shen S. Y., Kun Yang K., Lin D.H., *Nanotechnology*, **2020**, 31, 345603.
[62] Li Z. Z., Zhang H. G., Liang Wang L., Meng X. C., Shi J. J., Qi C. X., Zhang Z. S., Feng L. J., Li C. H., *J. Photoch. Photobio. A*, **2020**, 386, 112099.
[63] Yan D. J., Fu X. C., Shang Z. C., Liu J. L., Luo H. A., *Chem. Eng. J.*, **2019**, 361, 853-861.
[64] Zhang H. L., Li M., Wang W., Zhang G. H., Tang Q. J., Cao J. L., *Sep. Purif. Technol.*, **2021**, 272, 118911.
[65] Sajid M. M., Khan S. B., Javed Y., Amin N., Zhang Z. J., Shad N. A., Zha H. F., *Environ., Sci. Pullut. R.*, **2021**, 28, 35911-35923.
[66] Lin Q. Q., Zeng G. Y., Yan G. L., Luo J. Q., Cheng X. J., Zhao Z. Y., Li H., *Chem. Eng. J.*, **2022**, 427, 131668.

[67] Wang Y. Y., Jin Chen J., Que M. D., Wu Q. Z., Wang X. L., Zhou Y. X., Ma Y. Z., Li Y. J., Yang X. F., *Appl. Surf. Sci.*, **2023**, 639, 158270.
[68] Zhao D. X., Cai C., *Inorg. Chem. Front.*, **2020**, 7, 2799-2808.
[69] Lai C., An Z. W., Yi H., Huo X. Q., Qin L., Liu X. G., Li B. S., Zhang M.M ., Liu S. Y., Li L., Fu Y. K., Zhou X. R., Wang Z. H., An N., Shi X. X., *J. Colloid Interf. Sci.*, **2021**, 600, 161-173.
[70] Li K. S., Lu X. Y., Zhang Y., Liu K. L., Huang Y. C., Liu H., *Environ. Res.*, 2020, 185, 109409.
[71] Sha X. F., Huang H. Z., Sun S. Y., Huang H. Y., Huang Q., He Z. Y., Liu M. Y., Zhou N. G., Zhang X. Y., Wei Y., *J. Environ. Chem. Eng.*, **2020**, 8, 104261.
[72] Zhang L., Tan L., Yuan Z. X., Xu B. Q., Chen W. R., Tang Y. M., Li L. S., Wang J., *Chem. Eng. J.*, **2023**, 452, 139327.
[73] Ye C., Wu Z., Ma K. Y., Xia Z. H., Pan J., Wang M. Q., Ye C. H., *J. Alloy. Compd.*, **2021**, 859, 157787.
[74] Fan J. H., Gao J., Lv H., Jiang L., Qin F. J., Fan Y. H., Sun B. H., Wang J., Ikram M., Shi K. Y., *J. Mater. Chem. A*, **2022**, 10, 25714-25724.
[75] Xu D. X.,Ma Y. H., Wang J., Chen W. R., Tang Y. M., Li X. K., Li L .S., *Chem. Eng. J.*, **2021**, 426, 131246.
[76] Wang Q. Q., Guo L. N., Gao W., Li S. F.,Hao L., Wang Z.,Wang C., Wu Q. H., *Anal. Chim. Acta*, **2022**, 1233, 340511.
[77] Huang G. M., Li S. Z., Liu L. J., Zhu L. F., Wang Q., *Appl. Surf. Sci.*, **2020**, 503, 144183.
[78] Qing Xi Q., Yue X. P., Feng J. Q., Liu J. X., Zhang X. C., Zhang C. M., Wang Y. W., Wang Y. F., Lv Z. P., Li R., Fan C. M., *J. Solid State Chem.*, **2020**, 289, 121470.
[79] Chen X., Li Y. F., Wu Z. S., Xu X. L., Zhu W., Gao X. M., *J. Colloid Interf. Sci.*, **2021**, 602, 553-562.
[80] Xie F. X., Xi Q., Li H. F., Jian X., Liu J. X., Zhang X. C., Wang Y. W., Li R., Fan C. M., *J. Colloid Interf. Sci.*, **2022**, 617, 53-64.
[81] Fang Y., Cao Y., Tan B. H., Chen Q. L., *ACS Appl. Mater. Interfaces*, **2021**, 36, 42624-42634.
[82] Wang Y., Batmunkh M., Mao H., Li H., Jia B. H., Wu S. Y., Liu D. L., Song X. M., Sun Y., Ma T. Y., *Chinese Chem. Lett.*, **2022**, 33, 394-398.
[83] Zhang H. Y., Li L. X., Sun W. J., He J. H.,Xu Q. F., Lu J. M., *ChemElectroChem*, **2023**, 10, e202201001.
[84] Xiao W., Xu W. J., Huang W. J., Zhou Y., Jin Z. H., Wei X. P., Li J. P., *ACS Appl. Nano Mater.*, **2022**, 5, 18168-18177.

[85] Bai W. H., Zhou Y., Peng G., Wang J. N., Li A. M., François P., Corvini X., *Appl. Catal. B -Environ.*, **2022**, 315, 121606.
[86] Reghunath B. S., Devi K. R. S., Rajasekaran S., Saravanakumar B., William J. J., Pinheiro D., *Electrochim. Acta*, **2023**, 461, 142685.
[87] Sanga P., Wang J. J., Li X., Chen J., Qiu H. D., *Molecules*, **2023**, 28, 1541.
[88] [Liu B., Zhang X., Chu J. L., Li F., Jin C. X, Fan J., *Appl. Surf. Sci.*, **2023**, 618, 156565.
[89] Ling L. Y., Yuan C., Xu Q. Y., Li T. H., Zhu M. S., Zhai C. Y., *Surf. Interfaces*, **2023**, 36, 102483.
[90] Wu D. N., Zeng L. Y., Liu Y. W., Yuan C. L., Xue X. G., Zhang X. W., *Colloid. Surface. A*, **2023**, 663, 131010.
[91] Tariq A., Irfan Ali S. I., Akinwande D., Rizwan S., *ACS Omega*, **2018**, 3, 13828-13836.
[92] Iqbal M. I., Ali S. I., Amin F., Tariq A., Z. Iqbal M. Z., Rizwan S., *ACS Omega*, **2019**, 4, 8661-8668.
[93] Zhang Z. P., Wang B. Z., Zhao H. B., Liao J. -F., Zhou Z. C., Liu T. H., He B. C., Wei Q., Chen S., Chen H. -Y., Kuang D. -B., Li Y., Xing G. H., *Appl. Catal. B -Environ.*, **2022**, 312, 121358.
[94] Cheng S. S., Chen X., Wang M., Li G. Q., Qi X. F., Tian Y. T., Jia M. C., Han Y. B., Wu D., Li X. J., Shi Z. F., *Appl. Surf. Sci.*, **2023**, 621, 156877.
[95] Luo Y. J., Shen P., Li X. C., Guo Y. L., Chu K., *Nano Res.*, **2022**, 15, 3991-3999.
[96] Li J. F., Li Z. Y., Liu X. M., Li C. Y., Zheng Y. F., Yeung K. W. K., Cui Z. D., Liang Y. Q., Zhu S. L., Hu W. B., Qi Y. J., Zhang T. J., Wang X. B., Wu S. L., *Nat. Commun.*, **2021**, 12, 1224.
[97] Li Q. L., Tao Song T., Zhang Y. P., Wang Q., Yang Y., *ACS Appl. Mater. Interfaces*, **2021**, 13, 27323-27333.
[98] Qiu Z. L., Fan D. C., Xue X. H., Guo S. J., Lin Y. X., Chen Y. T., Tang D. P., *Chemosensors*, **2022**, 10, 252-267.
[99] Sun Y. X., Zhu Y. K., Wu H., Qu N., Xie L. J., Zhu J. B., Liu Z. H., Zhang Q., Cai W., Guo F. K., Sui J. H., *Energy Environ. Sci.*, **2024**, 17, 738-747.
[100] Liu B., Feng X. X., Long M. Q., Cai M. -Q., Yang J. L., *Phys. Rev. Appl.*, **2022**, 18, 054036.
[101] Ma H., Li J. B., Yang J., Wang N., Liu Z. G., Wang T. Y., Su D. W., Wang C. Y., Wang G. X., *Chem. Asian J.*, **2021**, 16, 3774-3780.
[102] Meija R., Lazarenko V., Rublova Y., Felsharuk A., Andzane J., Gogotsi O., Baginskiy I., Zahorodna V., Dutovs A., Voikiva V., Lohmus R., Viksnae A., Erts D., *Mater. Chem. Front.*, **2024**, 8, 1651-1664.

[103] Liu H. H., Cai Yang C., Jin X. Y., Zhong J. B., Li J. Z, *Colloid. Surface. A*, **2020**, 603, 125239.
[104] Kumar A., Singla Y., Sharma M., Bhardwaj A., Krishnan V., *Chemosphere*, **2022**, 308, 136212.
[105] Liu K., Zhang H. B., Fu T., Wang L. X., Tang R., Tong Z. F., Huang X. J., *Chem. Eng. J.*, **2022**, 438, 135609.
[106] Huang H. M., Xu Y. Y., Lu Z. Y.,Zhang A. H., Zhang D. F., Xue H. P., Dong P., Zhang J. F., Goto T., *J. Mater. Res. Technol.*, **2022**, 18, 4156-4168.
[107] Yang Z. M., Lin Q. Q., Zeng G. Y., Zhao S. M., Yan G. L., Marie Yap Ang M. B., Chiao Y. -H., Pu S. Y., *J. Membrane Sci.*, **2023**, 669, 121329.
[108] Guo H. L., Yu T. T., Zhao L., Qian J., Yu J. H., Zhang Y., Teng Y. Y., Zhu C. S., Yang T., Chen W. B., Gong P. C., Jiang C. S., Gao C. F., Yang B., Chenyu Yang C. Y., *Carbon Lett.*, **2023**, 33, 847-862.
[109] Wu S. S., Su Y. M., Zhu Y., Zhang Y. M., Zhu M. S., *Appl. Surf. Sci.*, **2020**, 520, 146339.
[110] Ke T., Shen S. Y., Yang K., Lin D. H., *Appl. Surf. Sci.*, **2022**, 580, 152302.
[111] Sharma G., Kumar A., Sharma S, Naushad M., Dai-Viet N. V., Ubaidullah M., Shaheen S. M., Stadler F. J., *Environ. Pollut.*, **2022**, 308, 119597.
[112] Bao Y. C., Liu Y. C., Pan J. K., Chen P. Y., Liu X. Y., Yang Li Y., Tang X. X., Zhang W. A., Liu B. F., Liu J., *Appl. Surf. Sci.*, **2022**, 589, 152883.
[113] Vishal S., Ajay K., Ashish K., Venkata K., *Chemosphere*, **2022**, 287, 132119.
[114] Bao Y. C., Pan J. K., Wu H., Zhang Z. S., Li Y. J., Wang Z. L., Hui T. T., Yang B., Li J. N., Hu H. T., Jiang J. L., Liu J., *J. Alloy. Compd.*, **2023**, 948, 169762.
[115] Niu K. F., Chen L., Rosen J., Björk J., *ACS Catal.*, **2024**, 14, 1824-1833.
[116] Liu K., Wang L. X., Fu T., Zhang H. B., Lu C. M., Tong Z. F., Yang Y., Peng Y., *Chem. Eng. J.*, **2023**, 457, 141271.
[117] Bai Y., Zhang K., Shi X., Li X., J. *Mater. Sci. - Mater. El.*, **2020**, 31, 1183-1190.
[118] Hermawan A., Hasegawa T., Asakura Y., Yin S., *Sep. Purif. Technol.*, **2021**, 270, 118815.
[119] Li, S.; Lin, F. X.; Zheng, H. S.; Zheng, Y. J.; Zhang, B. G.; Ma, J.; Nan, J. *Chem. Eng. J.*, **2023**, 452, 139298.
[120] Huang H. M., Zhang J. F., Tang C. M., Li A. Y., Zhang T. M., Xue H. P., Zhang D. F., *J. Environ. Chem. Eng.*, **2022**, 10, 108654.
[121] Mao Z. P., Hao W., Wang W., Ma F. B., Ma C. C., Chen S. G., *J. Colloid Interf. Sci.*, **2023**, 633, 836-850.
[122] Razium A. S., Sana J., Nazar H. K., Mawada T., Selcan K., Ayben K., Magnus W., *Biosens. Bioelectron.*, **2020**, 166, 112439.

[123] Ghosh K., Giri P. K., *Carbon*, **2024**, 216, 118515.
[124] Naguib M., Barsoum M. W., Gogotsi Y., *Adv. Mater.*, **2021**, 33, 2103393.
[125] Zhang K., Li D. Q., Cao H. Y., Zhu Q. H., Trapalis C., Zhu P. F., Gao X. H., Wang C. Y., *Chem. Eng. J.*, **2021**, 424, 130340.
[126] Bai S. H., Yang M. Q., Jiang J. Z., He X. M., Zou J., Xiong Z. G., Liao G. D., Liu S., *npj 2D Mater. Appl.*, **2021**, 5, 78.
[127] Wang Q., Wang M. J., Wen L., Zeng W., Ge B. H., Zhang C. F., Yue Y., Wang S. L., *Adv. Funct. Mater.*, **2024**, 34, 2214506.
[128] You Z. Y., Liao Y. L., Li X., Fan J. J., Xiang Q. J., *Nanoscale*, **2021**, 13, 9463-9504.
[129] Dillon A. D., Ghidiu M. J., Krick A. L., Griggs J., May S. J., Gogotsi Y., Barsoum M. W., Fafaman A. T., *Adv. Funct. Mater.*, **2016**, 26, 4162-4168.
[130] Ma G. L., Shao H., Xu J., Liu Y., Huang Q., Taberna P., Simon P., Lin Z. F., *Nat. Commun.*, **2021**, 12, 5085.
[131] Xu C., Wang L. B., Liu Z. B., Chen L., Guo J. K., Kang N., Ma X. L., Cheng H. M., Ren W. C., *Nat. Mater.*, **2015**, 14, 1135-1141.
[132] Yang S., Zhang P. P., Wang F. X., Ricciardulli A. G., Lohe M. R., Blom P. W. M., Feng X. L., *Angew. Chem. Int. Edit.*, **2018**, 130, 15717-15721.
[133] Wei Y., Zhang P., Soomro R. A., Zhu Q., Xu B., *Adv. Mater.*, **2021**, 33, 2103148.
[134] Kang F. W., Sun G. H., Philippe B., Wu H. Y., Ma F. X., Lu J., Gan J. L., Bian H. D., Gao F., Xiao S. S., *Chem. Eng. J.*, **2021**, 403, 126099.
[135] Gan Y. X., Jayatissa A. H., Yu Z., Chen X., Li M. H., *J. Nanomater.*, **2020**, 8917013.
[136] Yang G. J., Park S., *Materials*, **2019**, 12, 1177.
[137] Shi W. D., Song S. Y., Zhang H. J., *Chem. Soc. Rev.*, **2013**, 42, 5714-5743.
[138] Wang C., Zhang G., Fan S., Li Y., *J. Phys. Chem. Solids*, **2001**, 62, 1957-1960.
[139] Tian K., Lu H., Bu L. M., Huang X., Chiang C., Yang S. Q., Zhao Y., Lin Y., Zhao J. Q., Gao L. J., *Batteries Supercaps*, **2020**, 3, 1296-1305.
[140] Zhao R., Liu J. Y., Nie Y. H., Wang H. M., *Environ. Technol.*, **2024**, 45, 1748-1759.
[141] Wang F., Yang C. H., Duan M., Tang Y., Zhu J. F., *Biosens. Bioelectron.*, **2015**, 74, 1022-1028.
[142] Zhou L. Y., Zhang X. N., Ma L., Gao J., Jiang Y. J., *Biochem. Eng. J.*, **2017**, 128, 243-249.
[143] Feng A. H., Yu Y., Wang Y., Jiang F., Yu Y., Mi L., Song L. X., *Mater. Design*, **2017**, 114, 161-166.

[144] Lin H., Hu T., Huang Q. M., Cheng Y., Wang B., Xu J., Wang J. M., Wang Y. S., *Laser Photonics Rev.*, **2017**, 11, 1700148.
[145] Khajuria D. K., Kumar V. B., Gigi D., Gedanken A., Karasik D., *ACS Appl. Mater. Interfaces*, **2018**, 10, 19373-19385.
[146] Jiao Z. B., Luan J. H., Miller M. K., Chung Y. W., Liu C. T., *Mater. Today*, **2017**, 20, 142-154.
[147] Chang S., Bai Z. L., Zhong H. Z., *Adv. Optical Mater.*, **2018**, 6, 1800380.
[148] Kong D. Q., Bi S., Wang Z. H., Xia J. F., Zhang F. F., *Anal. Chem.*, **2016**, 88, 10667-10674.
[149] Ji H., Hwang S., Kim K., Kim C., Jeong N. C., *ACS Appl. Mater. Interfaces*, **2016**, 8, 32414-32420.
[150] [141] Rostamzadeh T., Khan M. S. I., Riche K., Lvov Y. M., Stavitskaya A. V., Wiley J. B., *Langmuir*, **2017**, 33, 13051-13059.
[151] Zhang Y., Zhang L. Y., Zhou C. W., *Acc. Chem. Res.*, **2013**, 46, 2329-2339.
[152] Lu F., Wang J. G., Sun X. L., Chang Z. J., *Mater. Design*, **2020**, 189, 108503.
[153] Zhang W. W., Jiang H. L., Li Y. H., Ma W. J., Yang X. Y., Zhang J. F., *J. Alloy. Compd.*, **2021**, 883, 160881.
[154] Zou Z. G., Wang Q., Zhu K., Ye K., Wang G. L., Cao D. X., Yan J., *Small*, **2022**, 18, 2106673.
[155] Lu X. F., Zhang Q. H., Liao J. C., Chen H. Y., Fan Y. C., Xing J. J., Gu S. J., Huang J. L., Ma J. X., Wang J. C., Wang L. J., Jiang W., *Adv. Energy Mater.*, **2020**, 10, 1902986.
[156] Jiang D. X., Sun X., Wu X. L., Zhang S., Qu X. F., Shi L., Zhang Y. L., Du F. L., *Nanophotonics*, **2020**, 9, 2077-2088.
[157]Abe R., *J. Photoch. Photobio. C*, **2010**, 11, 179-209.
[158] Li Z. W., Xu L. L., Babar Z. U. D., Raza A., Zhang Y. F., Gu X. R., Miao Y. -X., Zhao Z., Li G., *Nano Res.*, **2024**, 17, 4729-4736.
[159] Tahir M., Khan A. A., Tasleem S., Mansoor R., Fan W. K., *Energy Fuels*, **2021**, 35, 10374-10404.
[160] Huang K. L., Li C. H., Li H. Z., Ren G. M., Wang L., Wang W. T., Meng X. C., *ACS Appl. Nano Mater.*, **2020**, 3, 9581-9603.
[161] Li, X., Bai Y., Shi X., Su N., Nie G. Z., Zhang R. M., Nie H. B., Ye L. Q., *Mater. Adv.*, **2021**, 2, 1570-1594.
[162] Low J. X., Zhang L. Y., Tong T., Shen B. J., Yu J. G., *J. Catal.*, **2018**, 361, 255-266.
[163] Zhang Y. Y., Chen W., Zhou M., Miao G. B., Liu Y. L., *ACS Appl. Energy Mater.*, **2021**, 4, 9154-9165.

[164] Gan D. F., Huang Q., Dou J. B., Huang H. Y., Chen Y. Y., Liu M. Y., Wen Y. Q., Yang Z. Y., Zhang X. Y., Wei W., *Appl. Surf. Sci.*, **2020**, 504, 144603.
[165] Zhang Z., John T. Yates Jr., *Chem. Rev.*, **2012**, 112, 10, 5520-5551.
[166] Gao W. G., Li X. M., Luo S. J., Luo Z. L., Zhang X., Huang R., Luo M., *J. Colloid Interf. Sci.*, **2021**, 585, 20-29.
[167] Hou T. T., Li Q., Zhang Y. D., Zhu W. K., Yu K. F., Wang S. M., Xu Q., Liang S. Q., Wang L. B., *Appl. Catal. B*, **2020**, 273, 119072.
[168] Sun B. T., Qiu P. Y., Liang Z. Q., Xue Y. J., Zhang X. L., Yang L., Cui H. Z., Tian J., *Chem. Eng. J.*, **2021**, 406, 127177.
[169] Liu Q. X., Ai L. H., Jiang J., *J. Mater. Chem. A*, **2018**, 6, 4102-4110.
[170]Hu X. S., Wang Y. W., Ling Z., Song H. R., Cai Y., Li Z., Zu D. Y., Li C. P., *Appl. Surf. Sci.*, **2021**, 556, 149817.
[171] Wang H. L., Zhang L. S., Chen Z. G., Hu J. Q., Li S. J., Wang Z. H., Liu J. S., Wang X. C., *Chem. Soc. Rev.*, **2014**, 43, 5234-5244.
[172] Su T. M., Rui Peng R., Hood Z. D., Naguib M., Ivanov I. N., Keum J. K., Qin Z. Z., Guo Z. H., Wu Z. L., *ChemSusChem*, **2018**, 11, 688-699.
[173] Zhang W. D., Dong X. A., Liang Y., Sun Y. J., Dong F., *Appl. Surf. Sci.*, **2018**, 455, 236-243.
[174] Sarfraz B., Mehran M. T., Baig M. M., Naqvi S. R., Khoja A. H., Shahzad F., *Int. J. Energy Res*., **2022**, 46, 10942-10954.
[175] Li Q., Dongyang Pei D. Y., Zhang X. D., Sun H., *Electrochim. Acta*, 2024, 473, 143439.
[176] Yang Y. T., Jiang K. D., Guo J., Li J., Peng X. L., Hong B.,Wang X. Q., Ge H. L., *Chem. Eng. J.*, **2020**, 381, 122596.
[177] Yang X. Y., Li Y., Zhang P., Zhou R. M., Peng H. L., Liu D., Gui J. Z., *ACS Appl. Mater. Interfaces*, **2018**, 10, 23154-23162.
[178] Chang X., Wu Q., Wu Y. Y., Xi X., Cao J. R., Chu H. Y., Liu Q. H., Li Y. Y., Wu W., Fang X. D., Chen F. F., *Nano Lett.*, **2022**, 22, 8321-8330.
[179] Ali S. R., Praveen C. S., Kang S. G., Nair L., Bhamu K. C., Kumar P., *Appl. Surf. Sci.*, **2023**, 641, 158439.
[180] Lv Z. P., Ma W. S., Wang M., Dang J., Jian K. L., Liu D., Huang D. J., *Adv. Funct. Mater.*, **2021**, 31, 2102576.
[181] Sun Y. Y., J., Kwon N. H., Lim J., Jin X. Y., Gogotsi Y., Hwang S. -J., *ACS Nano*, **2024**, 18, 6243-6255.
[182] Zhang X. B., Shao B. Y., Sun Z. M., Gao Z., Qin Y., Ce C., Cui F. M., Yang X. J., *Ind. Eng. Chem. Res.*, **2020**, 59, 1822-1828.

[183] Yu L. H., Fan Z. D., Shao Y. L., Tian Z. N., Sun J. Y., Liu Z. F., *Adv. Energy Mater.*, **2019**, 9, 1901839.
[184] Yuan W. Y., Cheng L. F., An Y. R., Lv S. L., Wu H., Fan X. L., Zhang Y. N., Guo X. H., Tang J. W., *Adv. Sci.*, **2018**, 5, 1700870.
[185] Wei T., Liu W., Zhang S., Liu Q., Luo J., Liu X., *Chem. Commun.*, **2023**, 59, 442-445.
[186] Chen H.,Zhang S , Liu Q., Yu P., Luo J., Hu G., Liu X., *Inorg. Chem. Commun.*, **2022**, 146, 110170.
[187] Li R. Q., Wen H., Niu M. M., Guo L., Huang X., Yang C. M., Wang D. J., *J. Colloid Interf. Sci.*, **2024**, 659, 139-148.
[188] Chen N. J., Duan Z. Y., Cai W. R., Wang Y. B., Pu B., Huang H. C., Xie Y. T., Tang Q., Zhang H. T., Yang W. Q., *Nano Energy*, **2023**, 107, 108147.
[189] Ding H. M., Li Y. B., Li. M., Chen K., Liang K., Chen G. X., Lu J., Palisaitis J., Persson P. O. Å., Eklund P., Hultman L., Du S. Y., Chai Z. F., Gogotsi Y., Huang Q., *Science*, **2023**, 379, 1130-1135.
[190] Wang D., Zhou C. K., Filatov A. S., Cho W. J., Lagunas F., Wang M. Z., Vaikuntanathan S., Liu C., Flie R. F., Talapin D. V., *Science*, **2023**, 379, 1242-1247.
[191] Parra-Muñoz N., Soler M., Rosenkranz A., *Adv. Colloid Interfac.*, **2022**, 309, 102792.
[192] Wei S. Y., Tie S. J., Shen K., Sun H., Zheng X. J., Wang H., Liang W. Q., Zou J. H., Huang Y. X., Luo L. Z., Zhou X. Y., Zeng T. X., Ren A., Zhao D.W., Wu J. G., *Adv. Optical Mater.*, **2022**, 10, 2201585.
[193] Jiang D., Zhang Y. D., Du X. J., Zhang L. H., Shan X. L., Wang W. C., Shiigi H., Chen Z. D., *Chem. Commun.*, **2023**, 59, 1185-1188.
[194] Nagubandi L. A.1 Geetha A., Vasugi S., Balachandran S., Ilangovar I. G. K., *Cureus*., **2024**, 16, e61492.

Figure captions

Figure 1. Number and citations of MXenes/Bi-rcs-related archival literature and their involved field scopes (**inset**). Note that the statistical data are obtained basing on *Thomson Scientific* web of science (WOS) from 2018 to 2023.

Figure 2. Key development timeline of MXenes/Bi-rcs since 2018.

Figure 3. Schematic organization, each section heading and its subdivision headings of this review.

Figure 4. **a-e**): **a**) The hydrothermal synthesis routes of $BiVO_4/Ti_3C_2$. **b**) EDX (energy dispersive X-ray spectroscopy) elemental mapping of $BiVO_4/Ti_3C_2$. SEM (scanning electron microscope) images of **c**) Ti_3C_2 sheets, **d**) $BiVO_4$ and **e**) $BiVO_4/Ti_3C_2$-rcs.

Reproduced with permission.[65] Copyright 2021, Springer Berlin Heidelberg.

Figure 5. **a-e**): **a**) The preparation routes of BiNPs/$Ti_3C_2T_x$. **b-c**): SEM images of **b**) $Ti_3C_2T_x$ and **c**) BiNPs/$Ti_3C_2T_x$. **d**) TEM (transmission electron microscope) image of BiNPs/$Ti_3C_2T_x$. **e**) EDX elemental mapping of BiNPs/$Ti_3C_2T_x$. Reproduced with permission.[35] Copyright 2020, MDPI (Basel, Switzerland).

Figure 6. **a-e**): **a**) The synthesis process of Ti_3C_2/Bi_2WO_6 nanosheets. **b**): **i**) FESEM (field emission scanning electron microscope) image and **ii**) AFM (atomic force microscope) image of Bi_2WO_6. **c**) The height cutaway view of Bi_2WO_6. **d**) The **i**) FESEM (field emission scanning electron microscope) image and **ii**) AFM (atomic force microscope) image of TB2 (2 wt% Ti_3C_2 modified Bi_2WO_6 nanosheets). **e**) The height cutaway view of TB2. Reproduced with permission.[49] Copyright 2018, Wiley-VCH Verlag.

Figure 7. **a**): **i**) Photocatalytic CH_4 and CH_3OH production of as-prepared samples under visible irradiation. **ii**) GC·MS (gaschromatography-mass spectrometry) analysis of reaction products with ^{12}C and ^{13}C as carbon sources, respectively. Reproduced with permission.[49] Copyright 2018, Wiley-VCH Verlag. **b**): **i**) Photocatalytic CO and CH_3OH production of as-prepared samples (BOSO ($Bi_2O_2SiO_3$) and BOSO/TC-2 ($Bi_2O_2SiO_3$/Ti_3C_2, 2 represent MXene content)) under visible light irradiation, **ii**) photocatalytic CO and CH_3OH production of BOSO/TC-2 for 10 cycles. Reproduced with permission.[50] Copyright 2022, Elsevier. **c**): **i**) Photocatalytic CH_3OH production of as-prepared samples (BVNS ($BiVO_4$ nanosheets), BVNS/TC-1 ($BiVO_4$/ 2 mg $Ti_3C_2T_x$), BVNS/TC-2 (5 mg $Ti_3C_2T_x$) and BVNS/TC-3 (10 mg $Ti_3C_2T_x$)) under visible irradiation, **ii**) photocatalytic CH_3OH production of BVNS-TC3 for 3 cycles. Reproduced with permission.[51] Copyright 2022, Elsevier. **d**): **i**) Photocatalytic H_2, CO and CH_4 production of as-prepared samples ($Cs_2AgBiBr_6$, $Cs_2AgBiBr_6$/$Ti_3C_2T_x$ and $Ti_3C_2T_x$) under visible irradiation, **ii**) photocatalytic H_2, CO and CH_4 production of $Cs_2AgBiBr_6$/$Ti_3C_2T_x$ heterostructures for 5 h. Reproduced with permission.[93] Copyright 2022, Elsevier. **e**): The related photocatalytic mechanism diagram of **i**) TB,[49] **ii**) BOSO/TC,[50] **iii**) BVNS-TC [51] and **iii**) $Cs_2AgBiBr_6$/$Ti_3C_2T_x$.[93]

Figure 8. **a**): **i**) Photocatalytic H_2 production of as-prepared samples (Ti_3C_2, $Bi_4O_5Br_2$, and TCB4-*x* ($Bi_4O_5Br_2$ combined with 4 mL x wt% thin layered Ti_3C_2 (TL-Ti_3C_2)) under visible irradiation, **ii**) Photocatalytic H_2 production of $Bi_4O_5Br_2$/TL-Ti_3C_2. Reproduced with permission.[78] Copyright 2020, Elsevier. **b**): **i**) Photocatalytic H_2 production of as-prepared samples (Ti_3C_2, Ti_3C_2/BiOBr and BiOBr) under visible light irradiation, **ii**) schematic band alignment and charge flows at Ti_3C_2/BiOBr. Reproduced with permission.[62] Copyright 2020, Elsevier. **c**): **i**) Photocatalytic H_2 production of as-prepared samples (Ti_3C_2, Bi_5O_7Br, TCB5-*x* (x wt%Ti_3C_2/Bi_5O_7Br) under visible irradiation, **ii**) photocatalytic H_2 production of TCB5-10 (the optimal) for 5 cycles, **iii**) energy band structure of Bi_5O_7Br/Ti_3C_2, **iv**) mechanism diagram of photocatalytic H_2 production over the Bi_5O_7Br/Ti_3C_2. Reproduced with permission.[80] Copyright 2022,

Elsevier. **d**): **i**) Photocatalytic NH_4^+ production of as-prepared samples (Ti_3C_2, $Bi_4O_5Br_2$, and xTCB ($Bi_4O_5Br_2$/x wt% Ti_3C_2)) under xenon lamp irradiation, **ii**) Photocatalytic N_2 fixation of as-prepared samples (Ti_3C_2, $Bi_4O_5Br_2$, 5TCB, 10TCB and 15TCB) under xenon lamp irradiation, **iii**) energy band structure of $Bi_4O_5Br_2$, **iv**) energy band structure of Ti_3C_2/$Bi_4O_5Br_2$. Reproduced with permission.[79] Copyright 2021, Elsevier. **e**)**: i-ii**) Photocatalytic NH_3 production of BiOBr/Ti_3C_2 under visible light irradiation, **iii**) energy band structure of BiOBr/Ti_3C_2, **iv**) mechanism diagram of photocatalytic NH_3 production over the BiOBr/Ti_3C_2. Reproduced with permission.[81] Copyright 2021, American Chemical Society.

Figure 9. **a-b**) Photocatalytic de-NO_x of as-prepared samples (BiOBr, BiOBr/$Ti_3C_2T_x$, (Ti,C)-BiOBr and (Ti,C)-BiOBr/$Ti_3C_2T_x$) under different wavelength light irradiation, **c**) Photocatalytic de-NO_x of (Ti,C)-BiOBr/0.10$Ti_3C_2T_x$ for 7 cycles under >290 nm light irradiation, **d-e**) energy band structure of BiOBr, (Ti,C)-BiOBr, BiOBr/$Ti_3C_2T_x$ and (Ti,C)-BiOBr/$Ti_3C_2T_x$. Reproduced with permission.[118] Copyright 2021, Elsevier.

Figure 10. **a**): **i-ii**) Absorption graph of MO dye under visible light over **i**) $BiVO_4$ and **ii**) $BiVO_4$/MXene, **iii**) photocatalytic MO dye degradtion of as-prepared samples under different wavelength light irradiation (the black, yellow and purple line represent no-catalyst, $BiVO_4$ and $BiVO_4$/MXene, respectively). Reproduced with permission.[65] Copyright 2021, Springer Berlin Heidelberg. **b**): **i-iii**) Time dependent adsorption spectra of MG degradation by ternary nanocomposites **i**) BWTM01 (Bi_2WO_6/TiO_2 (20wt%)/Ti_3C_2 (1 wt%)), **ii**) BWTM05 (BWTM with 5 wt% Ti_3C_2) and **iii**) BWTM10 (BWTM with 10 wt% Ti_3C_2), **iv-vi**) photocatalytic MO dye degradtion of **iv**) Bi_2WO_6, **v**) TiO_2 and **vi**) BWTM01 under visible light irradiation. Reproduced with permission.[104] Copyright 2022, Elsevier. **c**): UV-visible absorption spectra of **i**) Ti_3C_2 nanosheets, **iii**) Bi_2O_3 nanoflower and **v**) Ti_3C_2/Bi_2O_3 nanohybrids for methylene blue. Kinetic study of all the prepared samples **ii**) kinetic rate, **iv**) linear kinetics and **vi**) percentage degradation for methylene blue. Reproduced with permission.[54] Copyright 2022, Elsevier. **d**): **i**) Photocatalytic RhB degradation of as-prepared samples (Bi_2WO_6, BN-*x* (Bi_2WO_6/x wt%Nb_2CT_x)) under visible light irradiation and **ii**) corresponding first-order kinetic plots, **iii**) photocatalytic MB degradation of as-prepared samples under visible light irradiationand and **iv**) corresponding first-order kinetic plots, **v**) mechanism diagram of photodegradation of Bi_2WO_6/Nb_2CT_x. Reproduced with permission.[59] Copyright 2020, Elsevier. **e**): **i**) UV-Vis diffuse reflectance spectra of $Bi_{12}O_{17}Cl_2$ nanosheets/Cl-terminated Ti_3C_2 (*i.e.*, BOC/CTC), CTC MXene and BOC samples, **ii**) transient photocurrent responses of as-prepared BOC, BOC + CTC (physical mixed) and BOC-CTC samples, **iii**) photocatalytic MB degradation of as-prepared samples under visible light irradiation and **iv**) corresponding In(C_0/C) versus reaction time plots, **v**) mechanism diagram of photocatalytic performance over the $Bi_{12}O_{17}Cl_2$/Ti_3C_2. Reproduced with permission.[53] Copyright 2022, Nonferrous Metals Society of China.

Figure 11. **a**) **i**) UV-Vis spectral change of RhB over BTC-8 (BiOBr/Ti_3C_2, 8 represent

8 mg Ti_3C_2 was added) under visible-light irradiation, **ii**) photocatalytic RhB degradation of as-prepared samples (BiOBr, BTC-2, BTC4, BTC8 and BTC12) under visible light irradiation. Reproduced with permission.[57] Copyright 2019, Springer. **b**) **i-ii)** photocatalytic RhB degradation of as-prepared samples (Ti_3C_2, (001)TiO_2/Ti_3C_2, BiOI, BTO-*x* (BiOI/x mg TiO_2), BT-*x* (BiOI/x mg Ti_3C_2) and BTT-x (BiOI/(x mg (001)TiO_2/Ti_3C_2)) under visible light irradiation. Reproduced with permission.[61] Copyright 2020, IOP Publishing Ltd. **c**) mechanism diagram of photocatalytic performance of BiOBr/Ti_3C_2. **d**) mechanism diagram of RhB photodegradation of Ti_3C_2/TiO_2/BiOI.

Figure 12. **a**): **i**) The synthesis route of V_2C/Bi/Fe_2O_3, **iv**) photocatalytic BPA (bisphenol A) degradation of as-prepared samples (V_2C, Fe_2O_3/V_2C and Bi/Fe_2O_3/V_2C) under visible light irradiation. Reproduced with permission.[40] Copyright 2023, Wiley-VCH GmbH. **a**) **ii**) photocatalytic BPA degradation of as-prepared samples (BiOI and TCB-10 (OVs-BiOI/10 wt% Ti_3C_2)) under visible light irradiation and **iii**) corresponding -ln(C/C_0) *vs*. reaction time. Reproduced with permission.[39] Copyright 2021, Elsevier. **b**): **i**) Mechanism diagram of the CR photodegradation of BGFO-Sn/MXene (Gd^{3+}- and Sn^{4+}-codoped bismuth ferrite/MXene), **ii**) photocatalytic CR degradation of as prepared samples (pure MXene,and BGFO-*x*Sn/MXene ($Bi_{0.9}Gd_{0.1}Fe_{1-0.01x}Sn_{0.01x}$/MXene)) under visible light irradiation. Reproduced with permission.[91] Copyright 2018, American Chemical Society. **c**): **i**) Mechanism diagram of CR (Congo red) photodegradation of BFO/MXene, **ii**) photocatalytic CR degradation of as prepared samples, **iii**) photocatalytic CR degradation of BFO/MXene for 4 cycles. Reproduced with permission.[56] Copyright 2019, American Chemical Society. **d**): **i**) Photocatalytic CR degradation of as prepared samples. Reproduced with permission.[56] Copyright 2019, American Chemical Society. **d**): **ii**) Photocatalytic CR degradation of as prepared samples ($BiVO_4$ (red line) and $BiVO_4$/MXene (blue line)) under visible light irradiation, **iii**) photocatalytic CR degradation of $BiVO_4$/MXene for 3 cycles with different time. Reproduced with permission.[65] Copyright 2021, Springer Berlin Heidelberg.

Figure 13. **a-c**): **a**) Photocatalytic TC (tetracycline hydrochloride) degradation by the as-prepared samples Bi_2MoO_6, BT-*x* (Bi_2MoO_6/Ti_3C_2 with weight ratio of Bi_2MoO_6 and Ti_3C_2 was set as 500 : *x*) and LBT (BT with layered Ti_3C_2)), **b**) photocatalytic Cr removal of as-prepared samples and **c**) corresponding UV-vis absorption spectral changes of Cr(VI) solution over the BT-30 sample (pH = 2.0). Reproduced with permission.[68] Copyright 2020, Royal Society of Chemistry. **d-f**): **d**) Photocatalytic TC degradation of as-prepared samples (Bi_2O_3 and BiOTiC-*x* (Ti_3C_2 QDs/Bi_2O_3, *x* ml Ti_3C_2 QDs), **e**) photocatalytic TC degradation of BiOTiC-75 for 4 cycles and **f**) photocatalytic degradation of different waste water over BiOTiC-75. Reproduced with permission.[69] Copyright 2021, Elsevier.

Figure 14. **a**) Mechanism diagram of 4-NA (4-nitroaniline) over sponge-confined Bi/$Ti_3C_2T_x$. Reproduced with permission.[36] Copyright 2021, Royal Society of

Chemistry. **b**) Gibbs free energy change diagram for NO_3 reduction to NH_3 on the (112) crystal plane of Bi_2O_3 and the structural models of intermediates (Insert figure: Gibbs free energy change diagram for HER (hydrogen evolution reaction) on the (-112) crystal plane of Bi_2O_3). Reproduced with permission.[83] Copyright 2022, Wiley-VCH GmbH. **c-d**) **c**) Optimized structures of N_2 adsorption on **i**) Bi site of pristine $Bi_2S_3/Ti_3C_2T_x$ (S_v-free), **ii**) S-vacancy site of $Bi_2S_{3-x}/Ti_3C_2T_x$ and **iii**) interfacial-Bi site of $Bi_2S_{3-x}/Ti_3C_2T_x$, Gibbs free energy change diagram of NRR (nitrogen reduction reaction) over **iv**) S-vacanvy and **v**) interfacial Bi of $Bi_2S_{3-x}/Ti_3C_2T_x$ at zero potential. **d**) **i-ii**) Calculated S_v formation energies of Bi_2S_{3-x} and $Bi_2S_{3-x}/Ti_3C_2T_x$, respectively. Average potential profiles of **iii**) Bi_2S_3 and **iv**) $Ti_3C_2T_x$. **v**) Charge density difference (isosurface value is 0.005 eV·Å) and **vi**) corresponding electron location function image. **vii**) DOS (density of state) of Bi_2S_3, Bi_2S_{3-x}, $Bi_2S_{3-x}/Ti_3C_2T_x$. Reproduced with permission.[95] Copyright 2022, Springer.

Figure 15. **a**) The preparation route of sponge-confined $Bi/Ti_3C_2T_x$. **b**) **i**) SEM image of sponge-confined $Bi/Ti_3C_2T_x$, and photographs of the total **ii**) Bi-1.0% $Ti_3C_2T_x$ and **iii**) Bi-1.0% rGO gathered from the resultant solutions after each cycle with the sponge-confined Bi-1.0% $Ti_3C_2T_x$ and sponge-confined Bi-1.0% rGO being successively used for ten times, respectively. **c**) **i**) Catalytic hydrogeneration of 4-NA over different $Ti_3C_2T_x$ content of $Bi/Ti_3C_2T_x$ and **ii**) corresponding pseudo-first-order kinetic plots, and **iii**) the time on-line conversion curves of 4-NA over Bi-1.0%$Ti_3C_2T_x$ and Bi-1.0% rGO. **d**) Catalytic hydrogeneration of **i**) 4-NA, **ii**) 3-NA and **iii**) 2-NA over Bi-1.0%$Ti_3C_2T_x$ and Bi-1.0% rGO. Reproduced with permission.[36] Copyright 2021, Royal Society of Chemistry.

Figure 16. **a-d**) **a**) The synthesis route of Bi@MXene. **b**) SEM images of **i**) Ti_3C_2, **ii**) $Bi@Ti_3C_2$ and **iii**) TEM image of $Bi@Ti_3C_2$ composite. **c**) Catalytic NH_3 yield and faradaic efficiency of $Bi@Ti_3C_2$ at different potentials. **d**) Catalytic NH_3 yield and faradaic efficiency of $Bi@Ti_3C_2$ at -0.4 V *vs*. RHE for 5 cycles. Reproduced with permission.[38] Copyright 2022, Wiley-VCH-GmbH.

Figure 17. **a- f**) SEM image of **a**) $Ti_3C_2T_x$ and **b**) $Ti_3C_2T_x$/BiOCl. **c**) Catalytic NH_3 yield and faradaic efficiency of $Ti_3C_2T_x$/BiOCl/CC at different potentials. **d**) Catalytic NH_3 yield and faradaic efficiency of different electrodes at -0.10 V after 2 h electrolysis under ambient conditions. **e**) Catalytic NH_3 yield and faradaic efficiency of $Ti_3C_2T_x$/BiOCl/CC with alternating 2 h cycles between Ar- and N_2-saturated electrolytes. **d**) Catalytic NH_3 yield and faradaic efficiency of $Ti_3C_2T_x$/BiOCl/CC at -0.10 V for 5 cycles. Reproduced with permission.[82] Copyright 2022, springer. **g**) Catalytic NH_3 yield and faradaic efficiency of $Bi_2S_{3-x}/Ti_3C_2T_x$ at different potential. **h**) Catalytic NH_3 yield of Bi_2S_3, Bi_2S_{3-x}, $Bi_2S_{3-x}/Ti_3C_2T_x$ and annealed $Bi_2S_{3-x}/Ti_3C_2T_x$. **i**) Catalytic NH_3 yield and faradaic efficiency of $Bi_2S_{3-x}/Ti_3C_2T_x$ at -0.6 V for 7 cycles. Reproduced with permission.[95] Copyright 2022, Springer.

Figure 18. **a-i**): **a**) The synthesis route of Bi_2O_3/MXene. **b**) TEM image of

Bi_2O_3/MXene and **c**) corresponding elemental mapping images of Ti, C, F, Bi and O. **d**) LSV (linear sweep voltammetry) curves of MXene, Bi_2O_3 and Bi_2O_3/MXene with different molar ratios in the presence of KNO_3. **e**) Catalytic nitrate removal amount after 6 h electrolysis at -1.2V. **f**) Catalytic ammonia production and faradaic efficiency of different electrodes. **g**) Time-dependent changes in the concentrations of NO_3^--N, NO_2^--N and NH_4^+-N over 11% Bi_2O_3/MXene at 1.8 V *vs*. SCE. **h**) Catalytic ammonia production and faradaic efficiency at different potential. **i**) Catalytic ammonia production and faradaic efficiency of 11% Bi_2O_3/MXene for 6 cycles. Reproduced with permission.[83] Copyright 2022, Wiley-VCH GmbH.

Figure 19. **a-f**): **a**) The synthesis routes of $V_2C/BiVO_4$ and V_2C/Bi. **b**) SEM images of $V_2C/BiVO_4$ (left) and V_2C/Bi (right). **c**) TEM (left) and HRTEM (right) of V_2C/Bi. **d**) Catalytic ammonia production of V_2C/Bi, $V_2C/BiVO_4$ and V_2C at different potential. **e**) Catalytic ammonia production faradaic efficiency of V_2C/Bi, $V_2C/BiVO_4$ and V_2C at different potential. **f**) Chronoam-perometric test of V_2C/Bi at -0.5 V for 24 h (insert: corresponding NH_3 yields and faradaic efficiency after stability test). Reproduced with permission.[41] Copyright 2023, Royal Society of Chemistry.

Figure 20. **a**) Faradaic efficiency for various products of different electodes. Reproduced with permission.[83] Copyright 2023, Royal Society of Chemistry. **b-i**): **b**) Onset overpotential at j = 10 mA·cm^{-2} of different electrocatalysis (Pt/C, $V_2C/BiVO_4$, V_2C/Bi, V_2C, and GC (glassy carbon)) and **c**) corresponding Tafel plots. Cyclic voltammograms obtained from the non-Faradic Region of **d**) V_2C, **e**) $V_2C/BiVO_4$ and **f**) V_2C/Bi at different scan rates in 0.5 M H_2SO_4. **g**) EIS Nyquist plots of $V_2C/BiVO_4$, V_2C/Bi and V_2C. **h**) capacitive Δj as a function of scan rates for different samples. **i**) Chronoamperometric measurement for V_2C/BVO at a constant current density of -10 mA·cm^{-2} (insert: SEM image before (top) and after (bottom) stability test). Reproduced with permission.[41] Copyright 2023, Royal Society of Chemistry.

Table 1 Irradiation light (λ_{irr}) and "photocatalytic-towards" materials (PTMs) used for illustrating the photocatalytic activities of MXene/Bi-rcs, where the photocatalytic efficiency (FEs) of Mxenes, Bi-materials (Bi-Ms), and MXenes/Bi-rcs, are also shown in this table. Meanwhile, this table further lists the synthesis method and some key reaction conditions used for obtaining Mxenes, Bi-materials (Bi-Ms), and MXenes/Bi-rcs, including, for instance, the synthesis temperature and time, and the photocatalytic time. The symbol "~" denotes that the specific values are not found in the related works, which thus are evaluated based on the Figure data.

MXene/Bi-rcs	Synthesis method and reaction conditions	MXene	Etchant	Bi-Ms	Synthesis method and reaction conditions	λ_{irr}	PTMs	Behavior	C_{PTMs}	$C_{Catalyst}$	PEs (MXene)	PEs (Bi-Ms)	PEs (MXene/Bi-rcs)	*Refs.*
2D Ti_3C_2/2D Bi_2WO_6	Hydrothermal (120 °C, 24 h)	Ti_3C_2	HF	Bi_2WO_6	---	Simulated solar	CO_2	CH_4 production	- -	- -	- -	0.41 μmol·g^{-1}·h^{-1}	1.78 μmol·g^{-1}·h^{-1}	[49]
							CO_2	CH_3OH production	- -	- -	- -	0.07 μmol·g^{-1}·h^{-1}	0.44 μmol·g^{-1}·h^{-1}	
2D Ti_3C_2/2D $Bi_2O_2SiO_3$	*In-situ* growth + Hydrothermal (180 °C, 48 h)	Ti_3C_2	HF	$Bi_2O_2SiO_3$	---	300 W Xe lamp	CO_2	CO production	- -	- -	- -	3.45 μmol·g^{-1}·h^{-1}	17.82 μmol·g^{-1}·h^{-1}	[50]
							CO_2	CH_3OH production	- -	- -	- -	1.80 μmol·g^{-1}·h^{-1}	2.07 μmol·g^{-1}·h^{-1}	
2D $Ti_3C_2T_x$/2D $BiVO_4$	Electrostatic self-assembly	$Ti_3C_2T_x$	HF	$BiVO_4$	Hydrotheramal (120 °C, 12 h) + Calcination (300 °C, 1 h)	300 W Xe lamp	CO_2	CH_3OH production	- -	- -	- -	4.92 μmol·g^{-1}·h^{-1}	20.13 μmol·g^{-1}·h^{-1}	[51]
$Ti_3C_2T_x$/$Cs_2AgBiBr_6$	Self-assembly	$Ti_3C_2T_x$	HF	$Cs_2AgBiBr_6$	Hydrothermal (200 °C, 5 s) + Ice quenching	Xe lamp	CO_2	CO production	- -	- -	- -	8.80 μmol·g^{-1}·h^{-1}	11.1 μmol·g^{-1}·h^{-1}	[93]
							CO_2	CH_4 production	- -	- -	- -	0.11 μmol·g^{-1}·h^{-1}	1.3 μmol·g^{-1}·h^{-1}	
Ti_3C_2/Bi@BiOI	*In-situ* growth + Solvothermal (120 °C, 12 h)	Ti_3C_2	HF	BiOI	Solvothermal (120 °C, 12 h)	500 W Xe lamp	Bisphenol A	Degradation	5 mg·L^{-1}	0.2 g·L^{-1}	- -	13.1% in 80 min	88.8% in 80 min	[39]
V_2C/Bi/Fe_2O_3 (MXeBOTs)	*In-situ* growth + Solid-state annealing (500 °C, 24 h)	V_2C	NaF + HCl	--	--	300 W Xe lamp	Bisphenol A	Degradation	1 ppm	0.5 g·L^{-1}	48% in 60 min	- -	~97% in 60 min	[40]
$Ti_3C_2T_x$/$BiOBr_{0.5}I_{0.5}$	*In-situ* growth+ Hydrothermal (180 °C, 12 h)	$Ti_3C_2T_x$	HF	$BiOBr_{0.5}I_{0.5}$	Chemical bath	Visible light	Rhodamine B	Degradation	20 mg·L^{-1}	0.5 g·L^{-1}	- -	32% in 40 min	~100% in 40 min	[52]
							Phenol	Degradation	10 mg·L^{-1}	0.5 g·L^{-1}	- -	23% in 5 h	~50% in 5 h	
2D Ti_3C_2/2D $Bi_{12}O_{17}Cl_2$	Calcination (450 °C, 12 h)	Ti_3C_2	HF	---	Calcination (450 °C, 12 h)	300 W Xe lamp	Methyl blue	Degradation	10 mg·L^{-1}	4 g·L^{-1}	- -	~15% in 180 min	>90% in 180 min	[53]
Ti_3C_2/Bi_2O_3	Assembly	Ti_3C_2	HF	Bi_2O_3	Chemical reaction	Sunlight	Methylene blue	Degradation	12 mg·L^{-1}	40 mg·L^{-1}	31% in 55 min	43% in 55 min	80% in 55 min	[54]
							Benzoic acid	Degradation	12 mg·L^{-1}	40 mg·L^{-1}	17% in 45 min	27% in 45 min	45% in 45 min	
2D Ti_3C_2/2D Bi_2WO_6	*In-situ* growth + Hydrothermal (180 °C, 12 h)	Ti_3C_2	HF	Bi_2WO_6	Hydrothermal (180 °C, 12 h)	15 W LED	Rhodamine B	Degradation	10 mg·L^{-1}	0.4 g·L^{-1}	- -	~45% in 30 min	99.9% in 20 min	[55]
							Methylene blue	Degradation	10 mg·L^{-1}	0.4 g·L^{-1}	- -	- -	80% in 100 min	
							Methyl orange	Degradation	10 mg·L^{-1}	0.4 g·L^{-1}	- -	- -	86% in 100 min	
Ti_3C_2/$BiFeO_3$	Solvothermal (160 °C, 2 h)	Ti_3C_2	HF	$BiFeO_3$	Sol-gel	300 W Xe lamp	Congo red	Degradation	- -	0.1 g·L^{-1}	12% in 2 h	33% in 42 min	100% in 42 min	[56]
Ti_3C_2/BiOBr	Reflux process	Ti_3C_2	LiF + HCl	BiOBr	Reflux process	300 W Xe lamp	Rhodamine B	Degradation	20 mg·L^{-1}	0.5 g·L^{-1}	- -	79.5% in 50 min	89.3% in 50 min	[57]
Ti_3C_2/BiOBr	Electrostatic self-assembly	Ti_3C_2	NaF + HCl	BiOBr	Chemical reaction	300 W Xe lamp	Rhodamine B	Degradation	20 mg·L^{-1}	0.2 g·L^{-1}	- -	~98% in 24 min	99.4% in 24 min	[58]
							2,4-Dinitrophenol	Degradation	10 mg·L^{-1}	0.2 g·L^{-1}	- -	- -	45% in 60 min	
2D Nb_2CT_x/2D Bi_2WO_6	Hydrothermal (120 °C, 24 h)	Nb_2CT_x	HF	Bi_2WO_6	---	500 W Xe lamp	Rhodamine B	Degradation	15 mg·L^{-1}	0.5 g·L^{-1}	- -	90.1% in 90 min	99.8% in 50 min	[59]
							Methylene blue	Degradation	15 mg·L^{-1}	0.5 g·L^{-1}	- -	71.1% in 90 min	92.7% in 50 min	
2D $Ti_3C_2T_x$/2D BiOCl	Electrostatic self-assembly	$Ti_3C_2T_x$	HF	BiOCl	Hydrothermal (160 °C, 12 h)	300 W Xe lamp	*p*-nitrophenol	Degradation	20 mg·L^{-1}	0.6 g·L^{-1}	- -	69.48% in 50 min	97.86% in 50 min	[60]
Ti_3C_2/TiO_2/BiOI	*In-situ* growth + Hydrothermal	$Ti_3C_2T_x$	HF	---	---	500 W Xe lamp	Rhodamine B	Degradation	50 mg·L^{-1}	0.4 g·L^{-1}	- -	- -	0.0513 min^{-1}	[61]
Ti_3C_2/BiOBr	Hydrothermal (160 °C, 18 h)	Ti_3C_2	HF	BiOBr	Hydrothermal (160 °C, 18 h)	300 W Xe lamp	Rhodamine B	Degradation	10 mg·L^{-1}	1 g·L^{-1}	26% in 90 min	69% in 90 min	100% in 30 min	[62]
(3D) Ti_3C_2/BiOI	*In-situ* growth + Solvothermal (160 °C, 6 h)	Ti_3C_2	HF	---	---	300 W Xe lamp	Rhodamine B	Degradation	10 mg·L^{-1}	0.4 g·L^{-1}	- -	- -	99.8% in 30 min	[64]
Ti_3C_2/$BiVO_4$	Hydrothermal (150 °C, 3 h)	Ti_3C_2	--	$BiVO_4$	Hydrothermal (180 °C, 24 h)	300 W Xe lamp	Methyl orange	Degradation	10 mg·L^{-1}	0.1 g	- -	52% in 130 min	99.1 % in 130 min	[65]
							Congo red	Degradation	10 mg·L^{-1}	0.1 g	- -	64% in 60 min	99.5% in 60 min	
(2D) $Ti_3C_2T_x$/N-$Bi_2O_2CO_3$/PES	Self-assembly	$Ti_3C_2T_x$	LiF + HCl	N-$Bi_2O_2CO_3$	Chemical modified	Visible light	Congo red	Degradation	100 mg·L^{-1}	--	--	- -	99.9% in 8 h	[66]
							Rhodamine B	Degradation	10 mg·L^{-1}	--	--	- -	98.4% in 8 h	
							Trypan blue	Degradation	10 mg·L^{-1}	--	--	- -	98% in 8 h	

$Ti_3C_2T_x/Bi_4Ti_3O_{12}$	*In-situ* growth + solvothermal (180 °C, 18 h)	$Ti_3C_2T_x$	HF	---	---	500 W Xe lamp	Rhodamine B	Degradation	5 mg·L^{-1}	1 g·L^{-1}	19.8% in 50 min	- -	100% in 5 min	[67]
							Methyl orange	Degradation	5 mg·L^{-1}	1 g·L^{-1}	- -	- -	100% in 5 min	
2D Ti_3C_2/0D Bi_3TaO_7	*In-situ* growth + Hydrothermal (180 °C, 24 h)	Ti_3C_2	HF	Bi_3TaO_7	Hydrothermal (180 °C, 24 h)	420 nm LED lamp	Methylene blue	Degradation	10 mg·L^{-1}	0.5 g·L^{-1}	- -	40% in 2 h	90% in 2 h	[70]
$BiOIO_3/Ti_3C_2$	*In-situ* growth + Solvothermal (150 °C, 5 h)	Ti_3C_2	LiF + HCl	$BiOIO_3$	Solvothermal (150 °C, 5 h)	500 W Xe lamp	Rhodamine B	Degradation	5 mg·L^{-1}	0.5 g·L^{-1}	- -	67.7% in 3 h	97.6% in 3 h	[88]
2D Ti_3C_2/2D $BiOCl_{0.25}Br_{0.75}$	*In-situ* growth + Solvothermal (160 °C, 12 h)	Ti_3C_2	HF	$BiOCl_{0.25}Br_{0.75}$	Solvothermal (160 °C, 12 h)	300 W Xe lamp	Rhodamine B	Degradation	10 mg·L^{-1}	0.2 g·L^{-1}	- -	97.5% in 1 h	99% in 18 min	[90]
$Ti_3C_2T_x/Bi_{0.9}Gd_{0.1}Fe_{0.8}Sn_{0.2}O_3$	Co-precipitation	$Ti_3C_2T_x$	HF	$Bi_{0.9}Gd_{0.1}Fe_{0.8}Sn_{0.2}O_3$	Sol- gel technology + Calcination (600 °C, 3 h)	Visible light	Congo red	Degradation	- -	1 g·L^{-1}	80% in 2 h	- -	100% in 2 h	[91]
Ti_3C_2/$BiFeO_3$:La, Mn	Sol-gel technique	Ti_3C_2	HF	$BiFeO_3$:La, Mn	Sol- gel technology + Calcination (600 °C, 3 h)	300 W Xe lamp	Congo red	Degradation	10 mg·L^{-1}	1 g·L^{-1}	12% in 2 h	40% in 90 min	100% in 20 min	[92]
$Ti_3C_2T_x/Cs_2AgBiBr_6$	Hydrothermal + Ice water quenching (30 s)	$Ti_3C_2T_x$	LiF + HCl	$Cs_2AgBiBr_6$	Thermal injection (150°C)	300 W Xe lamp	Rhodamine B	Degradation	30 mg·L^{-1}	~0.67 g·L^{-1}	- -	~95% in 70 min	~100% in 70 min	[94]
Ti_3C_2/TiO_2/BiOCl	*In situ* growth + Hydrothermal (180 °C, 24 h)	Ti_3C_2	(purchased)	BiOCl	Hydrothermal (180 °C, 24 h)	500 W Xe lamp	Rhodamine B	Degradation	10 mg·L^{-1}	1 g·L^{-1}	<7% in 2 h	~45% in 2 h	78.36% in 35 min (pH = 2)	[103]
(2D Ti_3C_2/TiO_2/Bi_2WO_6	Electrostatic self-assembly	Ti_3C_2	HF	Bi_2WO_6	Solvohtermal (160 °C, 27 h)	Sunlight	Methyl green	Degradation	0.00005 M	0.5 g·L^{-1}	- -	- -	98.5% in 40 min	[104]
BiOBr/Ti_3C_2/MMT_{ex} (exfoliated montmorillonite)	Hydrothermal (170 °C, 2 h)	Ti_3C_2	HF	BiOBr	Microwave hydrothermal (170 °C, 2 h)	300 W Xe lamp	Rhodamine B	Degradation	10 mg·L^{-1}	0.6 g·L^{-1}	- -	- -	99% in 2 h	[105]
							Methylene blue	Degradation	10 mg·L^{-1}	0.6 g·L^{-1}	- -		99% in 2 h	
$Ti_3C_2T_x/TiO_2/Bi_2S_3$	Assembly	$Ti_3C_2T_x$	LiF + HCl	Bi_2S_3	Hydrotheraml (160 °C, 18 h)	300 W Xe lamp	Rhodamine B	Degradation	20 mg·L^{-1}	- -	- -	~70 %	93.7%	[106]
Ti_3C_2/Bi_2MoO_6/BiOBr	Hydrothermal	Ti_3C_2	LiF + HCl	Bi_2MoO_6	Acohol thermal (160 °C, 12 h)	70W Metal halide lamp	Congo red	Degradation	- -	- -	- -		98.89% in 6 h	[107]
				BiOBr	Acohol thermal (160 °C, 12 h)			Degradation			- -			
Ti_3C_2/AgBr/BiOBr@Ag	Co-precipitation	Ti_3C_2	HF	$BiOIO_3$	Solvothermal (160 °C, 16 h)	300 W Xe lamp	Rhodamine B	Degradation	20 mg·L^{-1}	0.5 g·L^{-1}	- -	~75% in 50 min	99.5% in 4 h	[117]
							Phenol	Degradation	10 mg·L^{-1}	0.5 g·L^{-1}	- -		~27% in 4 h	
Ti_3C_2/Bi@BiOI	*In-situ* growth + Solvothermal (120 °C, 12 h)	Ti_3C_2	HF	BiOI	Solvothermal (120 °C, 12 h)	500 W Xe lamp	Antipyrine	Degradation	3 mg·L^{-1}	0.2 g·L^{-1}	- -	10.32% in 140 min	71.09% in 140 min	[39]
2D Ti_3C_2/2D Bi_2WO_6	*In-situ* growth + Hydrothermal (180 °C, 12 h)	Ti_3C_2	HF	Bi_2WO_6	Hydrothermal (180 °C, 12 h)	15 W LED	Tetracycline hydrochloride	Degradation	20 mg·L^{-1}	0.4 g·L^{-1}	- -	~40% in 60 min	97% in 60 min	[55]
2D Nb_2CT_x/2D Bi_2WO_6	*In-situ* growth + Hydrothermal (120 °C, 24h)	Nb_2CT_x	HF	Bi_2WO_6	---	500 W Xe lamp	Tetracycline hydrochloride	Degradation	20 mg·L^{-1}	0.5 g·L^{-1}	- -	74.5% in 2 h	83.1% in 2 h	[59]
$Ti_3C_2T_x/Bi_4Ti_3O_{12}$	*In-situ* growth + Solvothermal (180 °C, 18 h)	$Ti_3C_2T_x$	HF	---	---	500 W Xe lamp	Tetracycline hydrochloride	Degradation	10 mg·L^{-1}	1 g·L^{-1}	- -	- -	100% in 2.5 min	[67]
(2D) Ti_3C_2/Bi_2MoO_6	*In-situ* growth + Hydrothermal (180 °C, 16 h)	Ti_3C_2	HF	Bi_2MoO_6	Hydrotheraml (180 °C, 16 h)	50 W white LED	Tetracycline	Degradation	15 mg·L^{-1}	0.5 g·L^{-1}	- -	37% in 30 min	99% in 30 min	[68]
Ti_3C_2 QDs/Bi_2O_3	*In-situ* growth + Hydrothermal (N_2, 180 °C, 16 h)	Ti_3C_2	NaF + HCl	Bi_2O_3	Hydrothermal (N_2, 80 °C, 24 h)	Visible light	Tetracycline	Degradation	20 mg·L^{-1}	0.2 g·L^{-1}	- -	14% in 90 min	82% in 90 min	[69]
$Ti_3C_2T_x/Bi_2O_2CO_3$	*In-situ* growth + Hydrothermal (150 °C, 12 h)	$Ti_3C_2T_x$	LiF + HCl	$Bi_2O_2CO_3$	Hydrothermal (150°C, 12 h)	300 W Xe lamp	Levofloxacin	Degradation	20 mg·L^{-1}	0.5 g·L^{-1}	- -	~65% in 80 min	95.4% in 80 min	[72]
2D Ti_3C_2/2D Bi_2WO_6	Electrostatic adsorption + *In-situ* hydrothermal (120 °C, 24 h)	Ti_3C_2	HF	Bi_2WO_6	Hydrothermal (120 °C, 24 h)	300 W Xe lamp	Amoxicillin	Degradation	20 ppm	0.4 g·L^{-1}	- -	~50%	100% within 40 min	[75]
$BiOIO_3/Ti_3C_2$	*In-situ* growth + Hydrothermal (150 °C, 5 h)	Ti_3C_2	LiF + HCl	$BiOIO_3$	Hydrothermal (150 °C, 5 h)	500 W Xe lamp	Tetracycline hydrochloride	Degradation	10 mg·L^{-1}	0.5 g·L^{-1}	- -	- -	93.4% in 3 h	[88]
							Diclofenac soidum	Degradation	20 mg·L^{-1}	0.5 g·L^{-1}	- -	- -	87.6% in 3 h	
							Levofloxacin hydrochloride	Degradation	10 mg·L^{-1}	0.5 g·L^{-1}	- -	- -	77.4% in 3 h	
							4-nitrophenol	Degradation	10 mg·L^{-1}	0.5 g·L^{-1}	- -	- -	44.3 in3 h	
Ti_3C_2/TiO_2/BiOCl	*In-situ* growth + Hydrothermal (180 °C, 24 h)	Ti_3C_2	- -	BiOCl	Hydrothermal (180 °C, 24 h)	500 W Xe lamp	Tetracycline	Degradation	20 mg·L^{-1}	1 g·L^{-1}	- -	~75% in 120 min	~90% in 120 min	[103]
BiOBr/Ti_3C_2/MMT_{ex} (exfoliated montmorillonite)	Hydrothermal (170 °C, 2 h)	Ti_3C_2	HF	BiOBr	Microwave hydrothermal (170 °C, 2 h)	300 W Xe lamp	Ciprofloxacin	Degradation	10 mg·L^{-1}	0.6 g·L^{-1}	34% in 2 h	61% in 2 h	96% in 2 h	[105]
Ti_3C_2/Bi_2MoO_6/BiOBr	*In-situ* growth + Hydrothermal (160 °C, 12 h)	Ti_3C_2	LiF + HCl	Bi_2WO_6	Alcohol thermal (160 °C, 12 h)	70W Metal halide lamp	Ciprofloxacin	Degradation	- -	- -	- -	- -	≥90% in 8 h	[107]
Ti_3C_2/Bi@BiOCl	*In-situ* growth + Hydrothermal (180 °C, 12 h)	Ti_3C_2	HF	Bi/BiOCl	Hydrothermal (180 °C, 12 h)	Visible light	Ciprofloxacin	Degradation	20 mg·L^{-1}	1 g·L^{-1}	- -	71% in 100 min	89% in 100 min	[109]
Ti_3C_2/BiOCl/g-C_3N_4	Ultrasonication + Stirring	Ti_3C_2	HF	---	---	500 W Xe lamp	Tetracycline	Degradation	10 mg·L^{-1}	0.2 g·L^{-1}	- -	- -	97% in 90 min	[111]
2D PCN/2D Ti_3C_2/2D Bi_2MoO_6	*In-situ* growth + Hydrothermal (180 °C, 24 h)	Ti_3C_2	HF	Bi_2MoO_6	Hydrothermal (180 °C, 24 h)	300 W Xe lamp	Tetracycline hydrochloride	Degradation	10 mg·L^{-1}	0.5 g·L^{-1}	- -	36.9% in 90 min	~81.3% in 90 min	[112]
2D Ti_3C_2/2D Bi_2WO_6/2D ZnO	Electrostatic self-assembly	Ti_3C_2	Purchased	Bi_2WO_6	Hydrothermal (160 °C, 27 h)	Natural sunlight	Ciprofloxacin	Degradation	0.00005 M	0.5 g·L^{-1}	- -	47% in 160 min	77% in 160 min	[113]
2D Bi_2WO_6/2D Ti_3C_2/2D $SnNb_2O_6$	*In-situ* growth + Anaerobic hydrothermal (195 °C, 48 h)	Ti_3C_2	HF	Bi_2WO_6	Hydrothermal (160 °C, 24 h)	300 W Xe lamp	Tetracycline hydrochloride	Degradation	10 mg·L^{-1}	0.5 g·L^{-1}	- -	~65% in 90 min	84% in 90 min	[114]

				BiOBr	Alcohol thermal (160 °C, 12 h)	- -	- -	Degradation			- -	- -		
$BiOBr/Bi_2MoO_6/Ti_3C_2/MMT_{ex}$	*In-situ* growth + Solvothermal (180 °C, 2.5 h)	Ti_3C_2	LiF + HCl	BiOBr	Solvothermal (160 °C, 2.5 h)	500 W Xe lamp	Levofloxacin	Degradation	5 $mg·L^{-1}$	- -	- -	~70% in 2 h	99% in 2 h	[116]
				Bi_2MoO_6	Solvothermal (160°C, 2.5 h)	- -	- -	- -			- -	~45% in 2 h	- -	
				$BiOBr/Bi_2MoO_6$	*In-situ* growth + Solvothermal (160 °C, 2.5 h)	- -	- -	- -			- -	~80% in 2 h	- -	
							Tetracycline	Degradation	20 $mg·L^{-1}$	- -	- -	- -	86% in 2 h	
							Ciprofloxacin	Degradation	20 $mg·L^{-1}$	- -	- -	- -	91% in 2 h	
							Ofloxacin	Degradation	20 $mg·L^{-1}$	- -	- -	- -	97% in 2 h	
Ti_3C_2/Bi_2WO_6	Electrostatic assembly	$Ti_3C_2T_x$	HF	Bi_2WO_6	Hydrothermal (120 °C, 24 h)	300 W Xe lamp	HCHO	Removal (CO_2)	5 μL		- -	11 $μmol·g^{-1}·h^{-1}$	72.8 $μmol·g^{-1}·h^{-1}$	[77]
							CH_3COCH_3	Removal (CO_2)	5 μL		- -	44.2 $μmol·g^{-1}·h^{-1}$	85.3 $μmol·g^{-1}·h^{-1}$	
$Ti_3C_2T_x$/(Ti,C)-BiOBr	Solvothermal (120 °C, 10 h)	$Ti_3C_2T_x$	HF	BiOBr	Solvothermal (120 °C, 10 h)	450 W Mercury lamp	NO_x	Removal	1 ppm		- -	~29% in 10 min	41% in 10 min	[118]
2D Ti_3C_2/2D Bi_2WO_6	*In-situ* growth + Hydrothermal (120 °C, 24 h)	Ti_3C_2	HF	Bi_2WO_6	Hydrothermal (120 °C, 24 h)	Simulated solar	- -	O_2 production	- -	- -	- -		---	[49]
2D Ti_3C_2/2D BiOBr	*In-situ* growth + Hydrothermal (160 °C, 18 h)	Ti_3C_2	HF	BiOBr	Hydrothermal (160 °C, 18 h)	300 W Xe lamp	Methanol	HER	0.25 $mL·L^{-1}$	1 $g·L^{-1}$	- -	2.07 $mM·g^{-1}$	8.04 $mM·g^{-1}$	[62]
2D Ti_3C_2/2D $Bi_4O_5Br_2$	*In-situ* growth + Alcoholysis	Ti_3C_2	LiF + HCl	$Bi_4O_5Br_2$	Alcoholysis	300 W Xe lamp	CH_3OH	HER	40 vol%	1.25 $g·L^{-1}$	- -	44.9 $μmol·g^{-1}·h^{-1}$	83.5 $μmol·g^{-1}·h^{-1}$	[78]
2D Ti_3C_2/2D $Bi_4O_5Br_2$	*In-situ* growth + Solvothermal (180 °C, 16 h)	Ti_3C_2	LiF + HCl	$Bi_4O_5Br_2$	Solvothermal (180 °C, 16 h)	300 W Xe lamp	N_2	NH_3 production	- -	0.5 $g·L^{-1}$	- -	51.06 $μmol·g^{-1}·h^{-1}$	277.74 $μmol·g^{-1}·h^{-1}$	[79]
2D Ti_3C_2/2D Bi_5O_7Br	*In-situ* growth + Hydrolysis	Ti_3C_2	LiF + HCl	Bi_5O_7Br	Chemical reaction	300 W Xe lamp	CH_3OH	HER	40 vol%	1.25 $g·L^{-1}$	- -	38.9 $μmol·g^{-1}·h^{-1}$	76.7 $μmol·g^{-1}·h^{-1}$	[80]
Ti_3C_2/BiOBr	Electrostatic adsorption + Self-assembly (160 °C, 10 h)	Ti_3C_2	HF	BiOBr	---	Xenon lamp	N_2	NH_3 production	35 $mL·min–1$	0.4 $g·L^{-1}$	4.47 $μmol·g^{-1}·h^{-1}$	4.8 $μmol·g^{-1}·h^{-1}$	234.6 $μmol·g^{-1}·h^{-1}$	[81]
Bi_2O_3/V_2C	--						NO	Removal						[140]
(2D) Ti_3C_2/Bi_2O_3	Co-precipitation	Ti_3C_2	HF	Bi_2O_3	Chemical reaction	Simulated sunlight	Klebsiella pneumonia	Bacteriostasis			8 mm in 20 mm	14 mm in 20 mm	12 mm in 20 mm	[54]
							Staphylococcus aureus	Bacteriostasis			0 mm in 20 mm	10 mm in 20 mm	14 mm in 20 mm	
Ti_3C_2/BiOBr	Electrostatic self-assembly	Ti_3C_2	NaF + HCl	BiOBr	Chemical reaction	300 W Xe lamp	Cr(VI)	Removal	10 $ml·L^{-1}$	0.2 $g·L^{-1}$	- -	8.7% in 40 min	47.5% in 40 min	[58]
(3D) Ti_3C_2/BiOI	Solvothermal method (160 °C, 6 h)	Ti_3C_2	HF	BiOI	---	300 W Xe lamp	Cr (VI)	Removal	10 $ml·L^{-1}$	0.2 $g·L^{-1}$	- -	~25% in 40 min	93.7% in 40 min	[64]
Ti_3C_2/Bi_2MoO_6	*In-situ* growth + Hydrothermal (180 °C, 16 h)	Ti_3C_2	HF	Bi_2MoO_6	Hydrothermal (180 °C, 16 h)	50 W white LED	Cr(VI)	Removal	15 $ml·L^{-1}$	0.5 $g·L^{-1}$	- -	32% in 1 h	100% in 1 h	[68]
$Cs_3Bi_2Br_9/Ti_3C_2T_x$	Electrostatic adsorption	$Ti_3C_2T_x$	LiF + HCl	$Cs_3Bi_2Br_9$	Chemical reaction	5W blue LED	Tuloene	Oxidation			- -	850 $μmol·g^{-1}·h^{-1}$	4011 $μmol·g^{-1}·h^{-1}$	[97]
$Ti_3C_2/TiO_2/Bi_2S_3$	Hydrothermal	Ti_3C_2	HF	---	---	300 W Xe lamp	Staphylococcus aureus	Sterilization			- -	- -	100% in 2 h	[110]
							Escherichia coli	Sterilization			- -	- -	100% in 2 h	
$Ti_3C_2/BiPO_4$/Ag	*In-situ* growth	Ti_3C_2	---	---	---	250 W MW oven	Escherichia coli	Bacteriostasis			- -	- -	~40%* in 5 min	[119]
Ti_3C_2/CeO_2/BiOI	*In-situ* growth + Hydrothermal (160 °C, 18 h)	Ti_3C_2	LiF + HCl	---	---	100 W Xe lamp	Escherichia coli	Bacteriostat			- -	- -	99.76%	[120]
							Staphylococcus aureus	Bacteriostat			- -	- -	99.89%	
$BiOI@CeO_2/Ti_3C_2$	Hydrothermal (160 °C, 4 h)	Ti_3C_2	HF	---	---	Energy-saving lamp	Escherichia coli	Bacteriostasis			- -	- -	99.76 % in 20 h	[121]
							Staphylococcus aureus	Bacteriostasis			- -	- -	99.89% in 20 h	
$Ti_3C_2T_x/TiO_2/BiVO_4$	Electrostatic adsorption	$Ti_3C_2T_x$	---	$BiVO_4$	---	300 W Xe lamp	CD44 proteins	Sensitive detection			- -	- -	0.014 $pg·mL^{-1}$	[122]
$Ti_3C_2T_x/Bi_2WO_6$	*In-situ* growth + Hydrothermal (160 °C, 24 h)	Ti_3C_2	HF	Bi_2WO_6	Hydrothermal (160 °C, 24 h)	20W LED	Benzyl alcohol	Oxidation			- -	0.70 $mmol·g^{-1}·h^{-1}$	5 $mmol·g^{-1}·h^{-1}$	[158]

Table 2 Overpotential (η) and "electrocatalytic-towards" materials (ETMs) used for illustrating the electrocatalytic applications of MXene/Bi-rcs, where the production efficiencies (NEs) and faradaic efficiencies (FEs) are also shown in this table.

MXene/Bi-rcs	Synthesis methods	ETMs	NEs	FEs (%)	MXene	Etchant	Yield rate	Bi compounds	routes	Yield rate	*Refs.*
BiOCl@$Ti_3C_2T_x$	*In-situ* hydrothermal growth (150 °C, 2 h)	Conversion of N_2 to NH_3	4.06 $\mu g \cdot h^{-1} \cdot cm^{-2}$ at -0.10 V (*vs.* RHE)	11.98%	$Ti_3C_2T_x$	HF	1.05 $\mu g \cdot h^{-1} \cdot cm^{-2}$	BiOCl	Hydrotherrmal (160 °C, 12 h)	2.06 $\mu g \cdot h^{-1} \cdot cm^{-2}$	[82]
(2D) Ti_3C_2/Bi	*In-situ* growth	Conversion of N_2 to NH_3	28.3 $\mu g \cdot h^{-1} \cdot cm^{-2}$ at -0.40 V (*vs.* RHE)	27.2%	Ti_3C_2	HF	- -	---	---	- -	[38]
$Ti_3C_2T_x/Bi_2S_{3-x}$	Microwave-assisted chemical reaction	Conversion of N_2 to NH_3	68.3 $\mu g \cdot h^{-1} \cdot mg^{-2}$ at -0.6 V	22.5% at -0.4 V	Ti_3C_2	LiF + HCl	5.7 $\mu g \cdot h^{-1} \cdot mg^{-2}$	---	---	7.6 $\mu g \cdot h^{-1} \cdot mg^{-2}$	[95]
$Ti_3C_2T_x/Bi_2O_3$	*In-situ* hydrothermal growth	Conversion of nitrate to NH_3	~7.00 $mg \cdot h^{-1} \cdot cm^{-2}$ at -1.80 V (*vs.* SCE)	91.1%	$Ti_3C_2T_x$	LiF + HCl	<2.5 $mg \cdot h^{-1} \cdot cm^{-2}$	---	---	<1 $mg \cdot h^{-1} \cdot cm^{-2}$	[83]
2D V_2C/2D $BiVO_4$	*In-situ* hydrothermal growth (200 °C, 4 h)	Conversion of N_2 to NH_3	40.5 $\mu g \cdot h^{-1} \cdot cm^{-2}$ at 0.50 V (*vs.* RHE)	5.45%	V_2C	NaF + HCl	<50 $\mu g \cdot h^{-1} \cdot cm^{-2}$	---	---		[41]
2D V_2C/0D BiNPs	Solid-state annealing	Conversion of N_2 to NH_3	88.6 $\mu g \cdot h^{-1} \cdot cm^{-2}$ at -0.50 V (*vs.* RHE)	8%							[41]
Bi/$Ti_3C_2T_x$	Electrostatic adsorption / Photodeposotion	Conversion of nitroarenes to H_2	100% in 6 min	---	$Ti_3C_2T_x$	LiF + HCl		---	---	58.12% in 6 min	[36]
			η	**Tafel slope**			**Tafel slope**			**Tafel slope**	
2D V_2C/2D $BiVO_4$	*In-situ* hydrothermal growth (200 °C, 4 h)	HER	384 mV at 10 mA cm^{-2}	160 $mV \cdot dec^{-1}$	V_2C	NaF + HCl	204 $mV \cdot dec^{-1}$				[41]
2D V_2C/0D BiNPs	Solid-state annealing (500 °C, 24 h)	HER	663 mV at 10 mA cm^{-2}	173 $mV \cdot dec^{-1}$							
$BiFeO_3/Cr_2CT_x$	Assembly	HER	128 mV at 10 mA cm^{-2}	53.3 $mV \cdot dec^{-1}$	Cr_2CT_x	HF		$BiFeO_3$	Hydrotherrmal (200 °C, 6 h)	218 $mV \cdot dec^{-1}$	[86]
			Removal efficiency								
$BiFeO_3/Ti_3C_2T_x$	*In-situ* hydrothermal growth (200 °C, 6 h)	Sulfadiazine removal	61.6% in ultrapure water	---	$Ti_3C_2T_x$	HF		---	---		[87]
		Sulfadathiazole removal	43.9% in ultrapure water								
		Sulfamerazine removal	72.8% in ultrapure water								
		Sulfamethazine removal	59.43% in ultrapure water								
		Sulfamethoxazole removal	82.5% in ultrapure water								
		Sulfisoxazole removal	43.09% in ultrapure water								

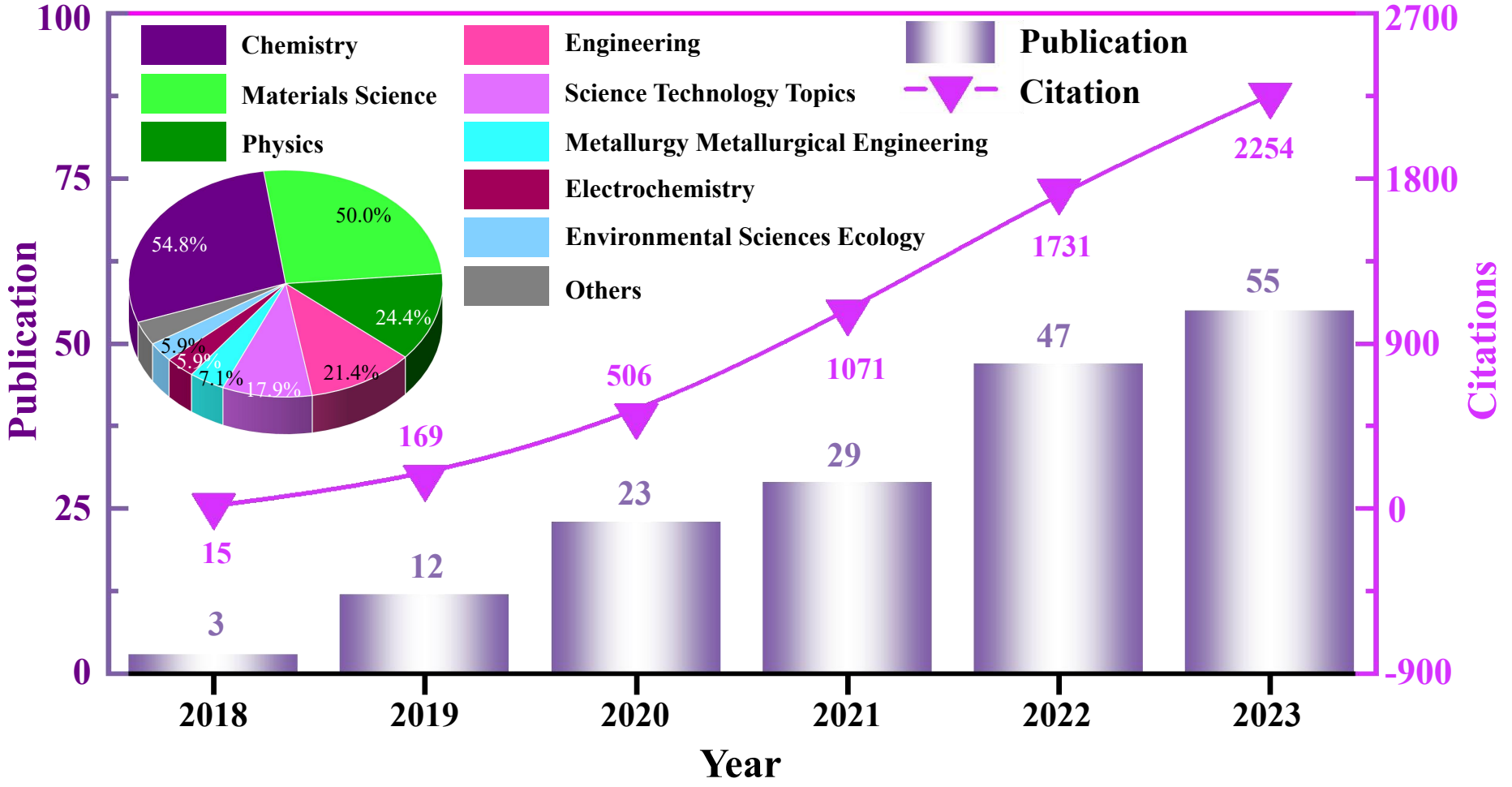
Chemistry
Materials Science
Physics
Engineering
Science Technology Topics
Metallurgy Metallurgical Engineering
Electrochemistry
Environmental Sciences Ecology
Others
54.8%
50.0%
24.4%
21.4%
17.9%
7.1%
5.9%
5.9%
Publication
Citation
Publication
Citations
Year
100
75
50
25
0
2700
1800
900
0
-900
2018
2019
2020
2021
2022
2023
3
12
23
29
47
55
15
169
506
1071
1731
2254

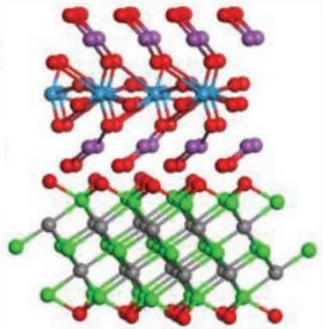

First synthesis of 2D /2D Ti_3C_2/Bi_2WO_6 heterohunction

2018.4

2018.10

Gd^{3+} and Sn^{4+} co-doped $BiFeO_3$/MXene for photograding CR dye

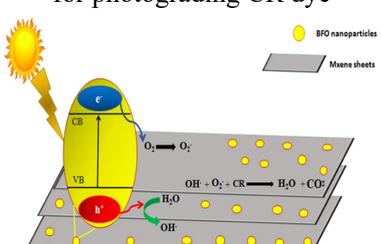

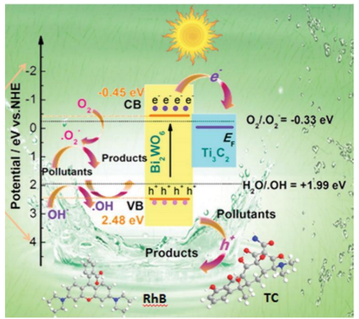

Ti_3C_2/Bi_2WO_6 synthesized by hydrothermal method

2019.9

2019.5

La- and Mn co-doped $BiFeO_3/Ti_3C_2$ for photograding CR dye

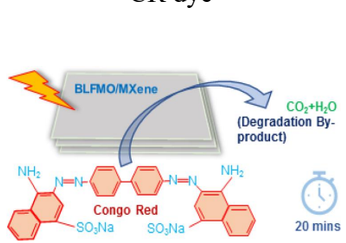

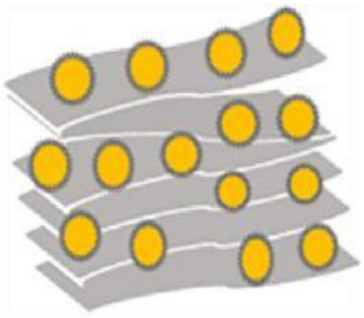

Binary Ti_3C_2/Bi/BiOCl

2020.8

2020.2

Electrostatic assembly Ti_3C_2/Bi_2WO_6 for photodegradation

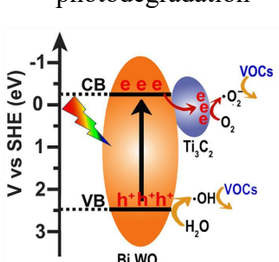

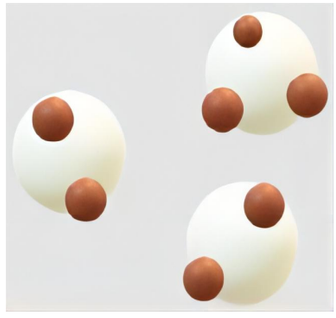

Ti_3C_2/Bi_2O_3 for photodegrading Tetracycline

2021.10

2021.12

Ti_3C_2/Bi@OVs-BiOI synthesized by solvothermal method

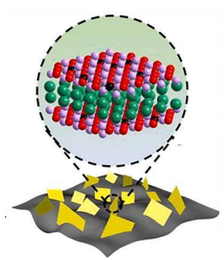

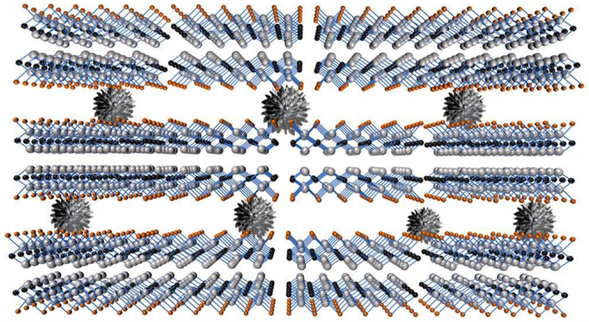

2D $Ti_3C_2T_x/Bi_2O_2CO_3$ for efficient photocatalytic wastewater treatment

2022.1

2022.9

$Ti_3C_2/Cs_2AgBiBr_6$ for photocatalytic CO_2 reduction

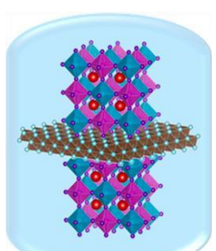

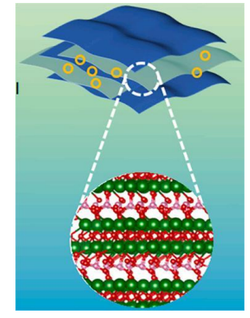

$Ti_3C_2T_x/Bi_2O_2CO_3$ for levofloxacin degradation

2023.1

2023.2

BiOBr/Bi_2MoO_6/Ti_3C_2/exfoliated -montmorillonite for quinolone abtibiotics photodegradation

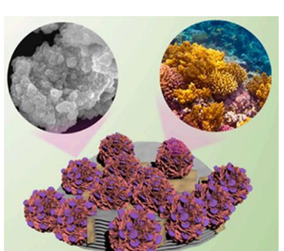

2023.7

V_2C/BiNPs electrolyte for HER and NRR

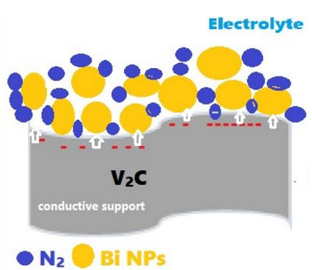

2018 2019 2020 2021 2022 2023

Recent advances in the synthesis, photo-/electrocatalytic properties and applications of MXenes/bismuth-related composites

1. Introduction

Backgroud introduction for MXenes

Development trace and archival literature survey for MXenes and MXenes/Bi-related composites

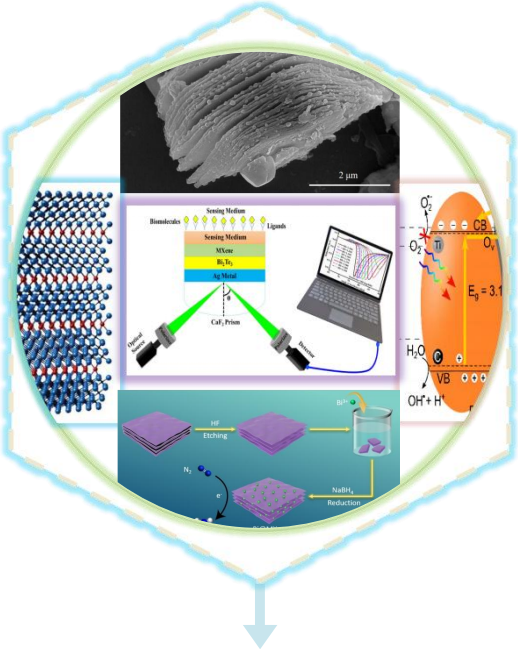

2. Synthesis routes of MXenes/Bi-rcs

2.1 Hydrothermal method

2.2 Coprecipitation strategy

2.3 *In-situ* growth strategy

2.4 Others

3. Photocatalytic properties and applications of MXenes/Bi-rcs

3.1 Photocatalytic CO_2 conversion

3.2 Production of oxygen (O_2), hydrogen (H_2), and ammonia (NH_3) gases

3.3 Degradation of NO_x (de-NO_x)

3.4 Degradation of organic dyes

3.5 Degradation of medicinal substances

4. Electrocatalytic properties and applications of MXenes/Bi-rcs

4.1 Properties and applications of NRR

4.2 Properties and applications of HER

5. Conclusion and perspectives

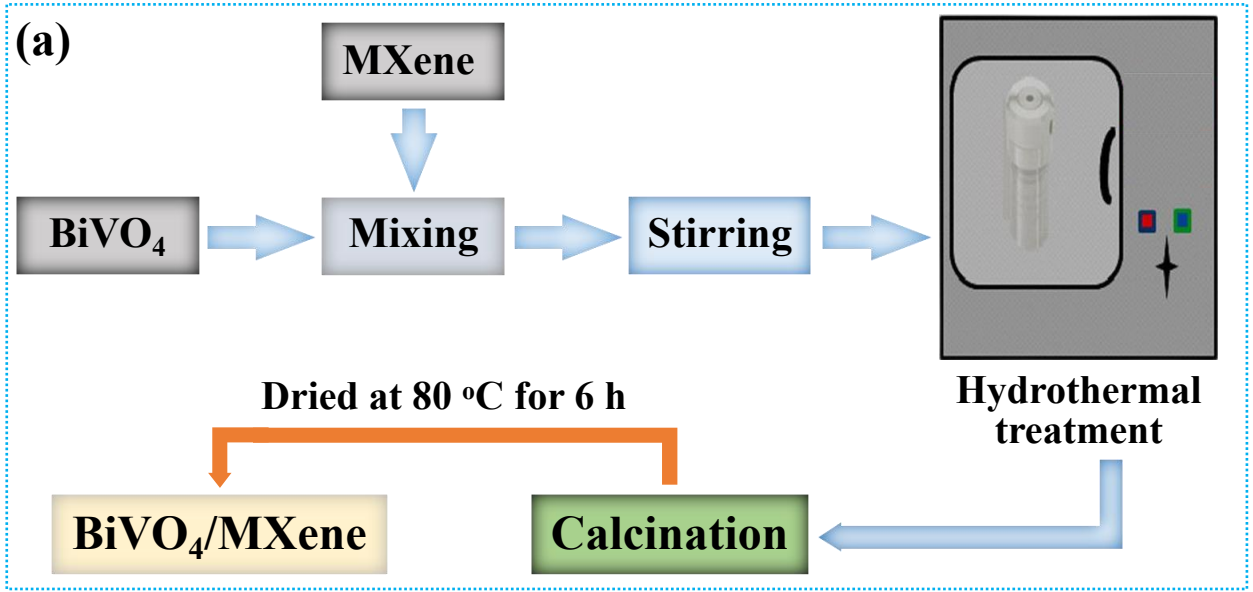
(a)
MXene
BiVO4
Mixing
Stirring
Hydrothermal treatment
Dried at 80 °C for 6 h
BiVO4/MXene
Calcination

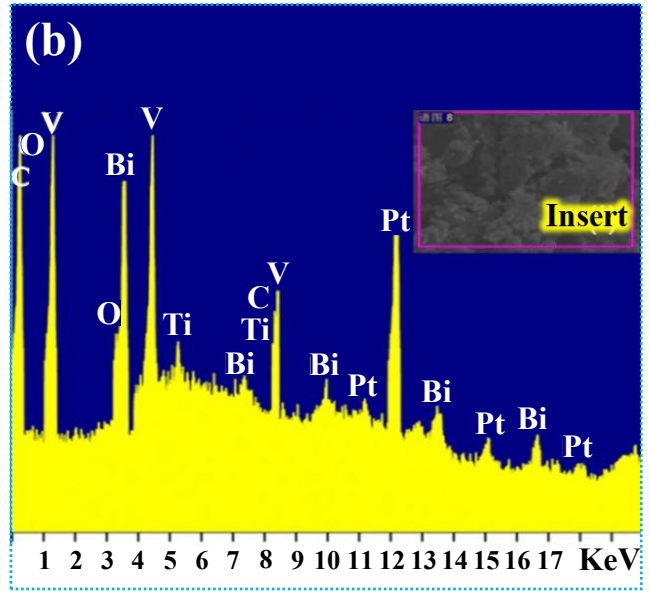
(b)
O
C
V
Bi
O
V
Ti
Bi
C
Ti
V
Bi
Pt
Pt
Bi
Pt
Bi
Pt
Insert
1 2 3 4 5 6 7 8 9 10 11 12 13 14 15 16 17 KeV

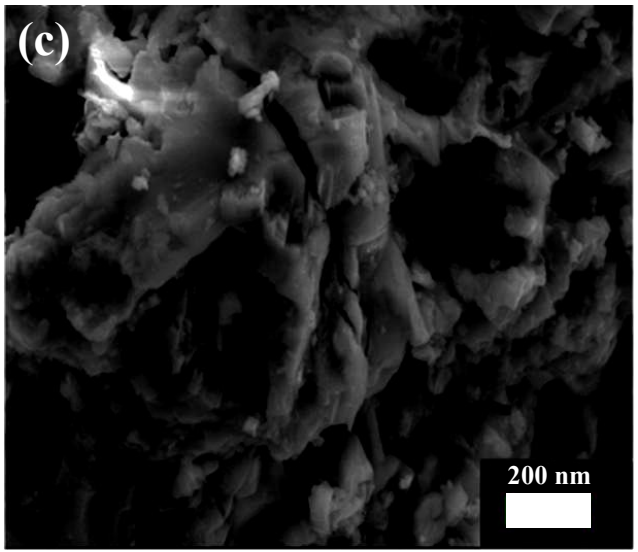
(c)
200 nm

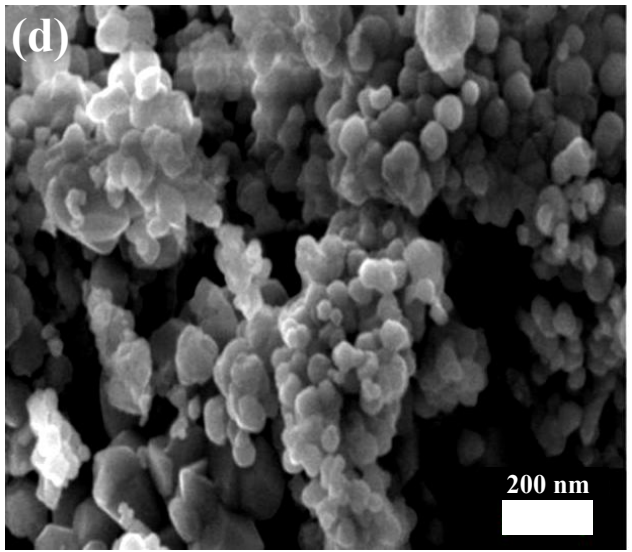
(d)
200 nm

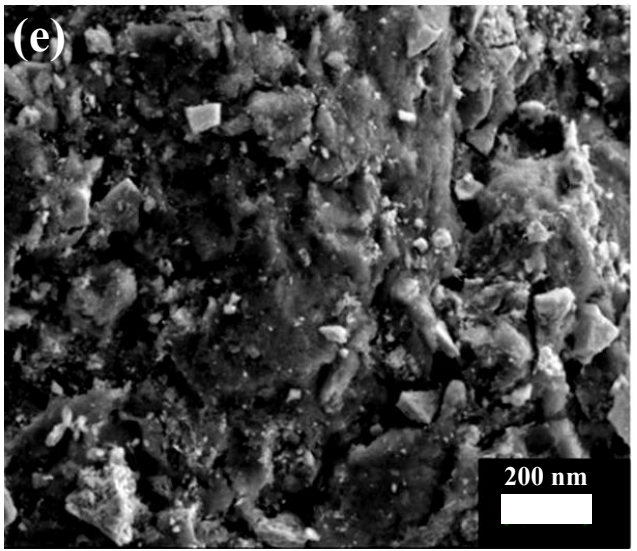
(e)
200 nm

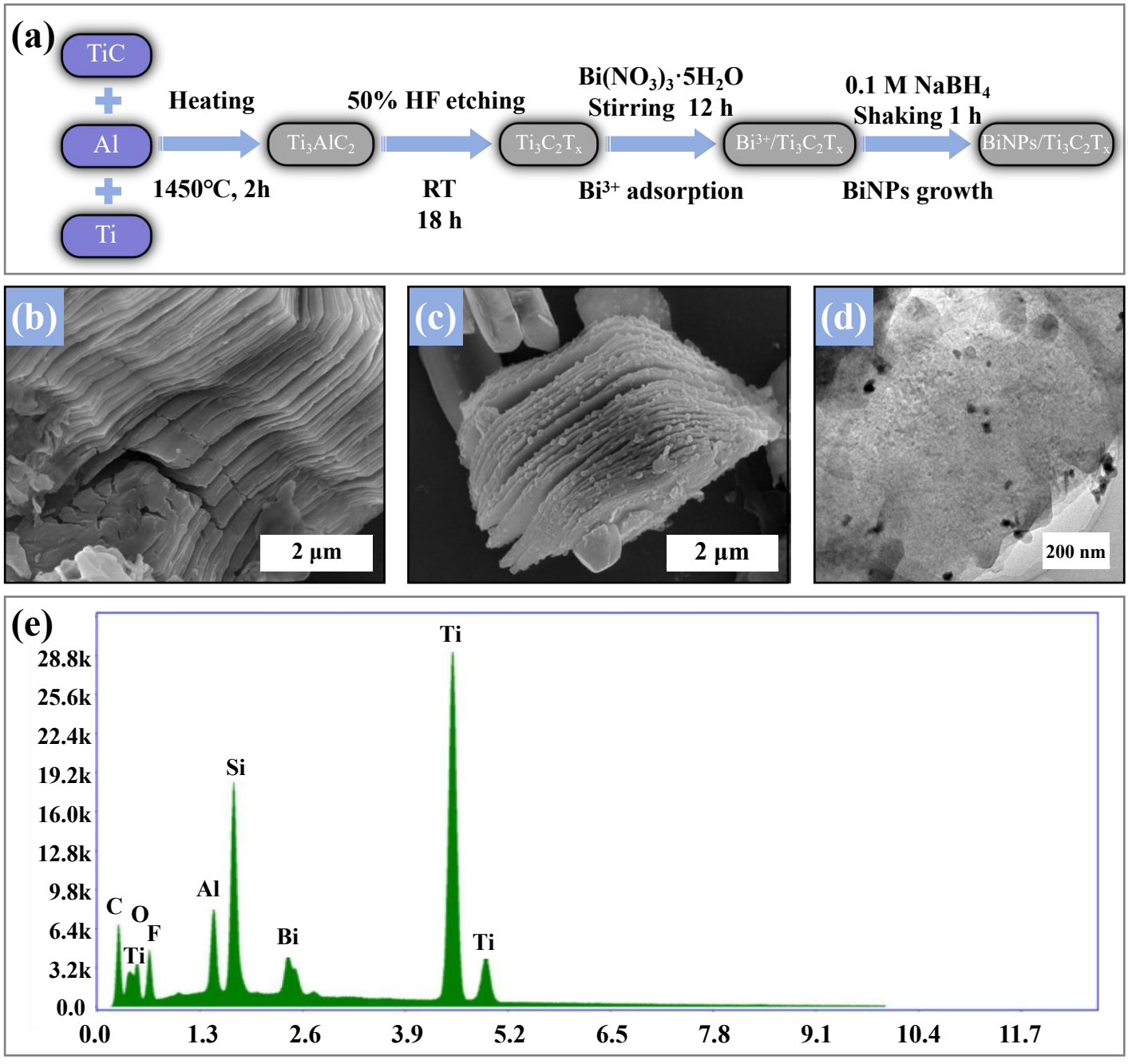
(a)
TiC
Al
Ti
Heating
1450°C, 2h
Ti3AlC2
50% HF etching
RT
18 h
Ti3C2Tx
Bi(NO3)3·5H2O
Stirring 12 h
Bi3+ adsorption
Bi3+/Ti3C2Tx
0.1 M NaBH4
Shaking 1 h
BiNPs growth
BiNPs/Ti3C2Tx
(b)
2 μm
(c)
2 μm
(d)
200 nm
(e)
28.8k
25.6k
22.4k
19.2k
16.0k
12.8k
9.8k
6.4k
3.2k
0.0
C
O
F
Ti
Al
Si
Bi
Ti
Ti
0.0
1.3
2.6
3.9
5.2
6.5
7.8
9.1
10.4
11.7

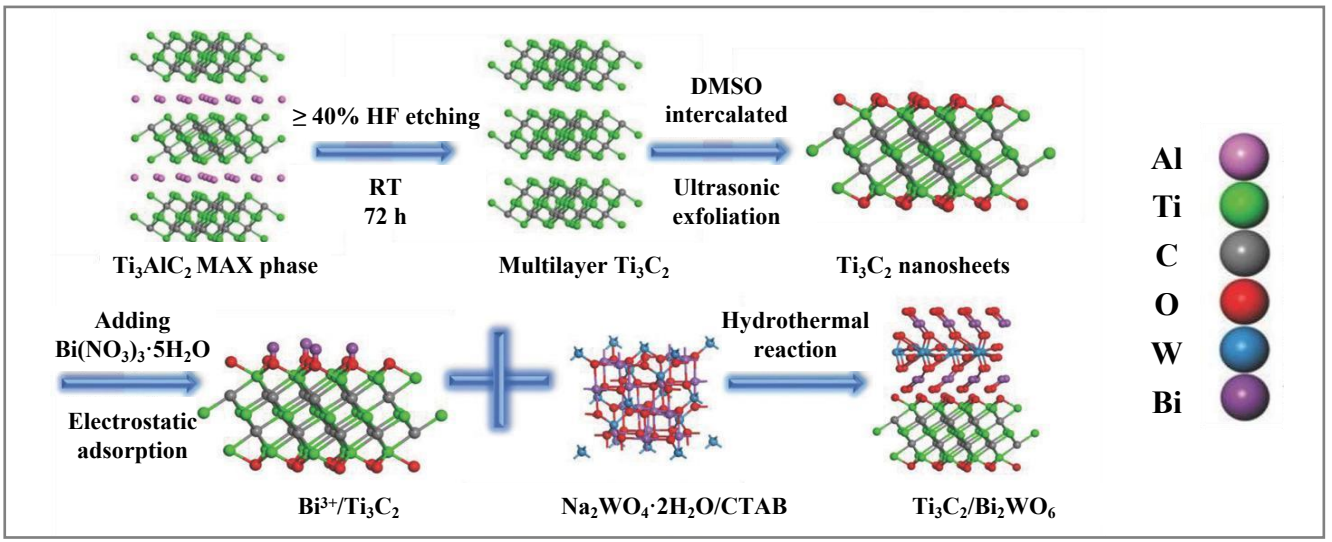

(a)

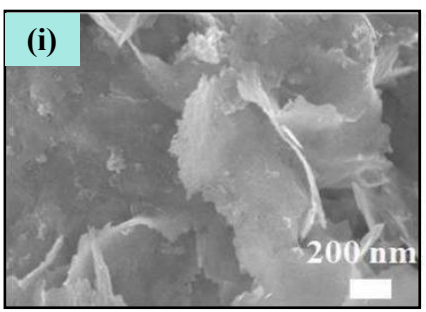

FESEM

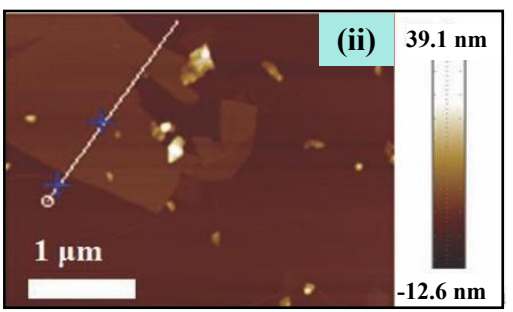

AFM

(b)

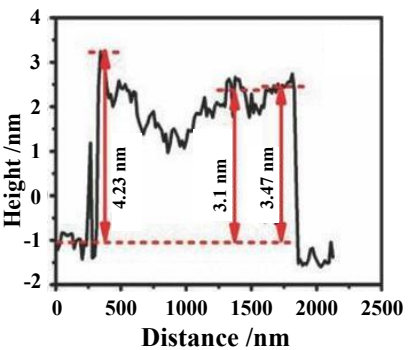

(c)

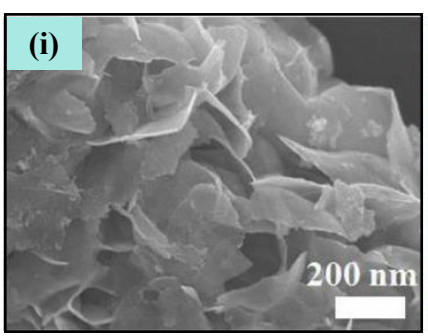

FESEM

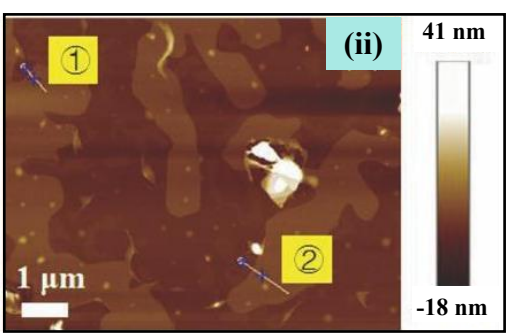

AFM

(d)

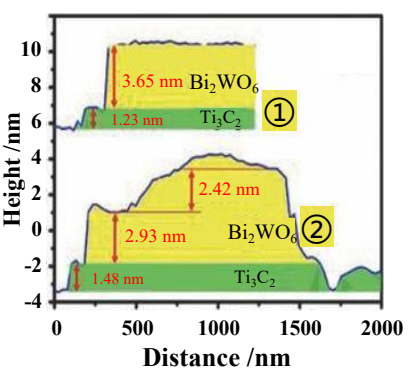

(e)

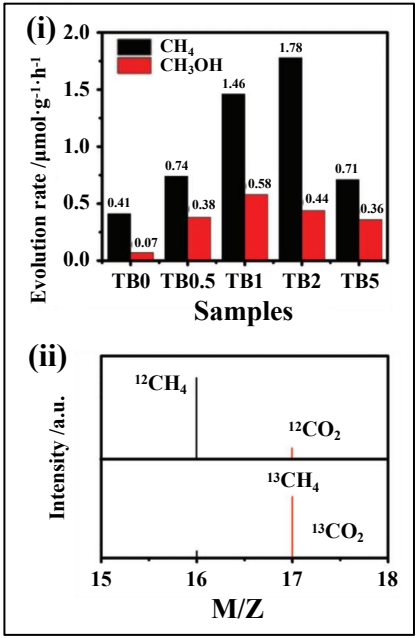
(i)
CH4
CH3OH
Evolution rate /μmol·g-1·h-1
0.41
0.07
0.74
0.38
1.46
0.58
1.78
0.44
0.71
0.36
TB0 TB0.5 TB1 TB2 TB5
Samples
(ii)
12CH4
12CO2
13CH4
13CO2
Intensity /a.u.
15 16 17 18
M/Z

(a)

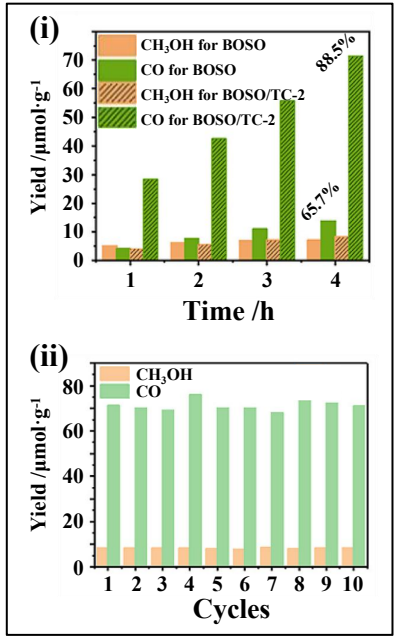
(i)
CH3OH for BOSO
CO for BOSO
CH3OH for BOSO/TC-2
CO for BOSO/TC-2
88.5%
65.7%
Yield /μmol·g-1
Time /h
(ii)
CH3OH
CO
Yield /μmol·g-1
Cycles

(b)

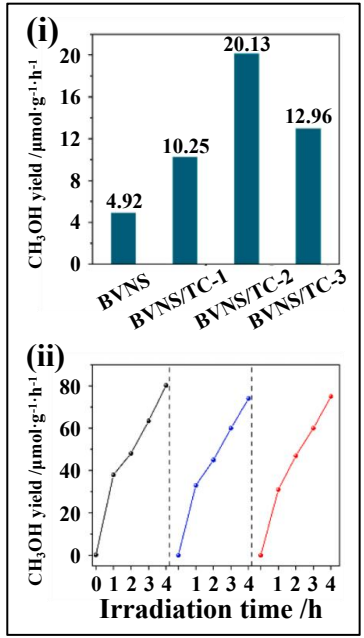
(i)
CH3OH yield /μmol·g-1·h-1
4.92
10.25
20.13
12.96
BVNS
BVNS/TC-1
BVNS/TC-2
BVNS/TC-3
(ii)
CH3OH yield /μmol·g-1·h-1
Irradiation time /h

(c)

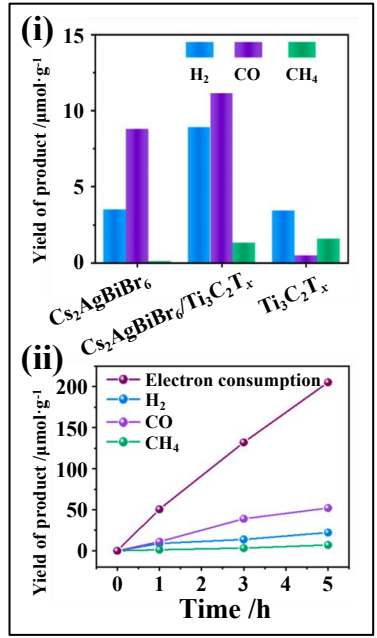
(i)
H2
CO
CH4
Yield of product /μmol·g-1
Cs2AgBiBr6
Cs2AgBiBr6/Ti3C2Tx
Ti3C2Tx
(ii)
Electron consumption
H2
CO
CH4
Yield of product /μmol·g-1
Time /h

(d)

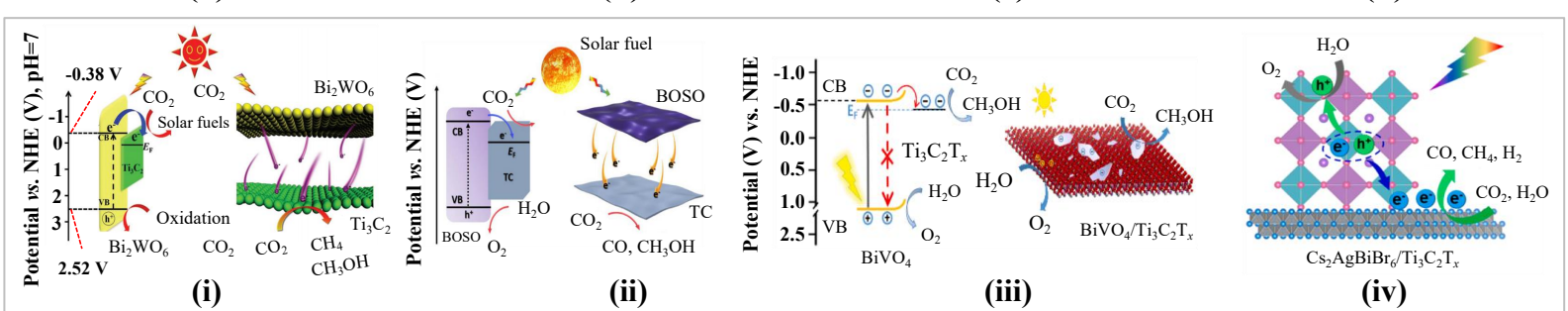
Potential vs. NHE (V), pH=7
-0.38 V
2.52 V
CO2
Solar fuels
Oxidation
Bi2WO6
Ti3C2
CH4
CH3OH
(i)
Potential vs. NHE (V)
Solar fuel
BOSO
TC
H2O
O2
CO, CH3OH
(ii)
Potential (V) vs. NHE
CB
VB
BiVO4
Ti3C2Tx
BiVO4/Ti3C2Tx
(iii)
H2O
O2
CO, CH4, H2
CO2, H2O
Cs2AgBiBr6/Ti3C2Tx
(iv)

(e)

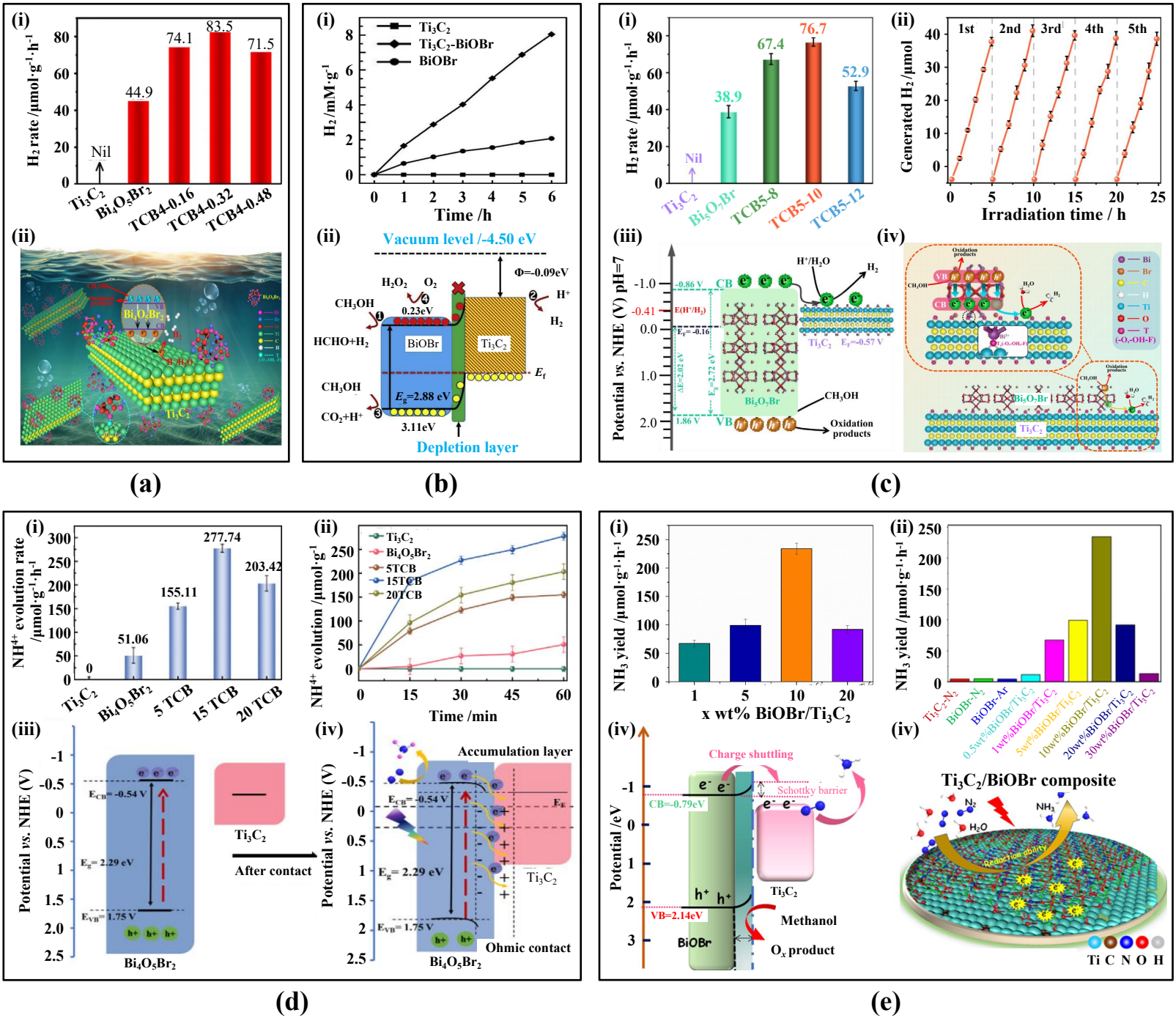
(i)
H2 rate /μmol·g-1·h-1
Nil
44.9
74.1
83.5
71.5
Ti3C2
Bi4O5Br2
TCB4-0.16
TCB4-0.32
TCB4-0.48
(ii)
Bi4O5Br2
Ti3C2
(a)
(i)
H2 /mM·g-1
Time /h
Ti3C2
Ti3C2-BiOBr
BiOBr
(ii)
Vacuum level /-4.50 eV
Φ=-0.09eV
H2O2
O2
CH3OH
0.23eV
HCHO+H2
BiOBr
Ti3C2
Ef
Eg=2.88 eV
CO2+H+
3.11eV
Depletion layer
(b)
(i)
H2 rate /μmol·g-1·h-1
Nil
38.9
67.4
76.7
52.9
Ti3C2
Bi4O5Br
TCB5-8
TCB5-10
TCB5-12
(ii)
Generated H2 /μmol
1st
2nd
3rd
4th
5th
Irradiation time / h
(iii)
Potential vs. NHE (V) pH=7
-0.86 V
CB
-0.41
E(H+/H2)
Eg=-0.16
0.0
1.0
2.0
ΔE=2.02 eV
Eg=2.72 eV
1.86 V
VB
H+/H2O
H2
Ti3C2 EF=-0.57 V
Bi4O5Br
CH3OH
Oxidation products
(iv)
Oxidation products
CH3OH
VB
CB
Bi4O5Br
Ti3C2
Bi
Br
C
H
Ti
O
T
(-O,-OH-F)
(c)
(i)
NH4+ evolution rate /μmol·g-1·h-1
0
51.06
155.11
277.74
203.42
Ti3C2
Bi4O5Br2
5 TCB
15 TCB
20 TCB
(ii)
NH4+ evolution /μmol·g-1
Ti3C2
Bi4O5Br2
5TCB
15TCB
20TCB
Time /min
(iii)
Potential vs. NHE (V)
ECB= -0.54 V
Eg= 2.29 eV
EVB= 1.75 V
Bi4O5Br2
Ti3C2
After contact
(iv)
Accumulation layer
ECB= -0.54 V
EF
Eg= 2.29 eV
EVB= 1.75 V
Ti3C2
Ohmic contact
Bi4O5Br2
(d)
(i)
NH3 yield /μmol·g-1·h-1
x wt% BiOBr/Ti3C2
(ii)
NH3 yield /μmol·g-1·h-1
Ti3C2-N2
BiOBr-N2
BiOBr-Ar
0.5wt%BiOBr/Ti3C2
1wt%BiOBr/Ti3C2
5wt%BiOBr/Ti3C2
10wt%BiOBr/Ti3C2
20wt%BiOBr/Ti3C2
30wt%BiOBr/Ti3C2
(iv)
Charge shuttling
Potential /eV
CB=-0.79eV
Schottky barrier
Ti3C2
VB=2.14eV
Methanol
BiOBr
Ox product
(iv)
Ti3C2/BiOBr composite
N2
NH3
H2O
Reduction ability
Ti C N O H
(e)

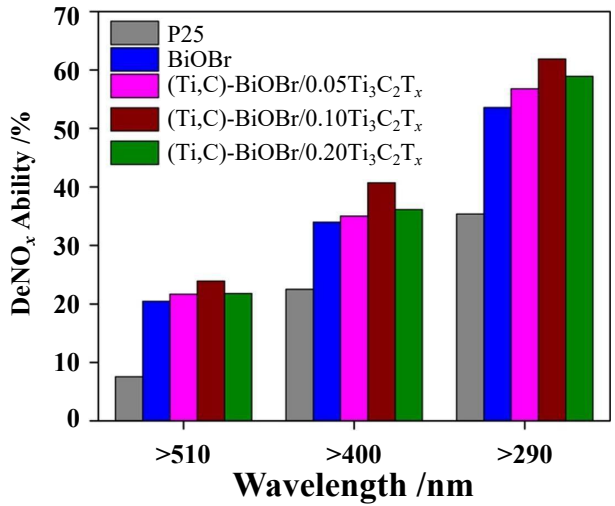
P25
BiOBr
(Ti,C)-BiOBr/0.05Ti3C2Tx
(Ti,C)-BiOBr/0.10Ti3C2Tx
(Ti,C)-BiOBr/0.20Ti3C2Tx
DeNOx Ability /%
Wavelength /nm
>510
>400
>290
(a)

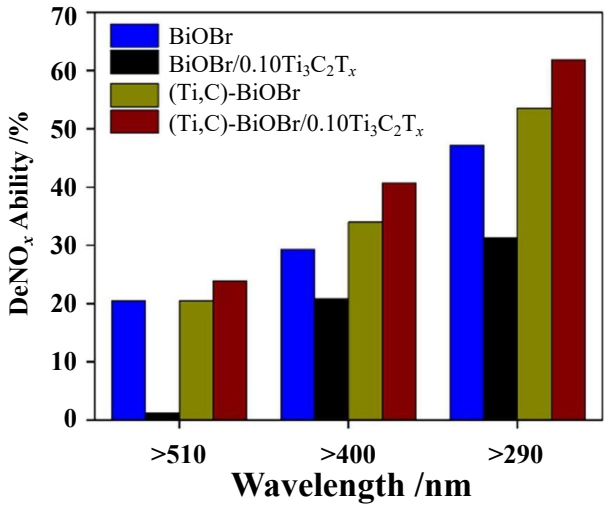
BiOBr
BiOBr/0.10Ti3C2Tx
(Ti,C)-BiOBr
(Ti,C)-BiOBr/0.10Ti3C2Tx
DeNOx Ability /%
Wavelength /nm
>510
>400
>290
(b)

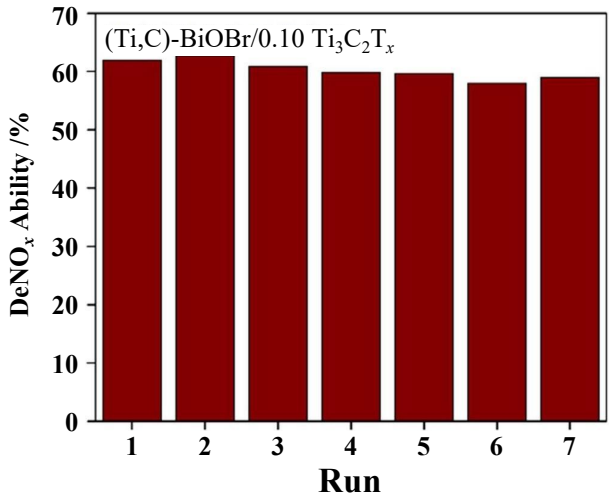
(Ti,C)-BiOBr/0.10 Ti3C2Tx
DeNOx Ability /%
Run
(c)

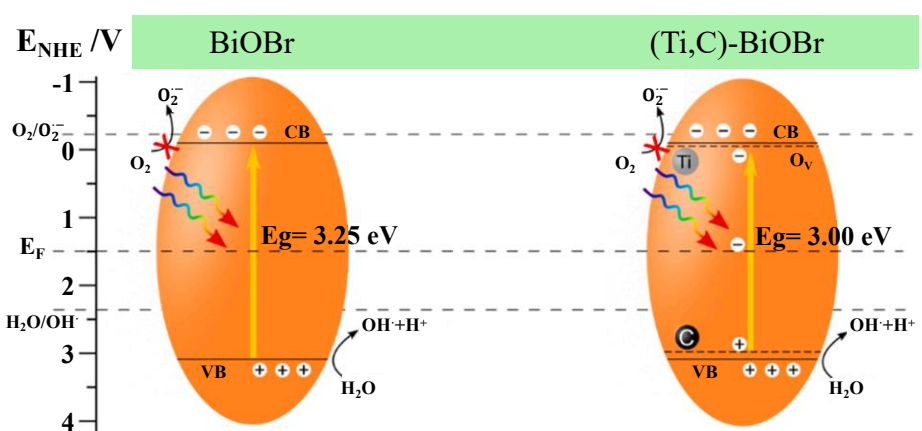
ENHE /V
BiOBr
(Ti,C)-BiOBr
O2/O2-
EF
H2O/OH-
CB
VB
Eg= 3.25 eV
Eg= 3.00 eV
Ti
OV
C
OH-+H+
H2O
(d)

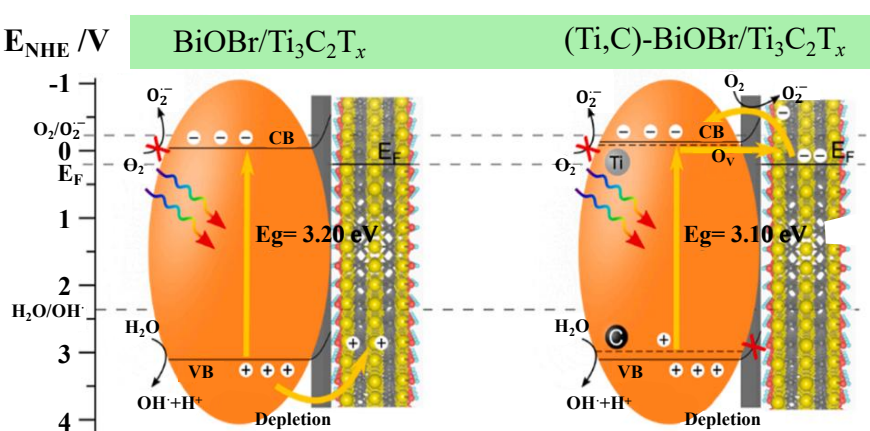
ENHE /V
BiOBr/Ti3C2Tx
(Ti,C)-BiOBr/Ti3C2Tx
O2/O2-
EF
H2O/OH-
CB
VB
Eg= 3.20 eV
Eg= 3.10 eV
Depletion
OH-+H+
H2O
(e)

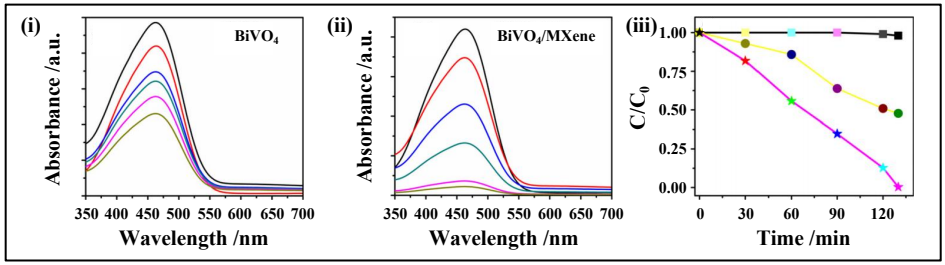
(i)
BiVO4
Absorbance /a.u.
Wavelength /nm
(ii)
BiVO4/MXene
Absorbance /a.u.
Wavelength /nm
(iii)
C/C0
Time /min

(a)

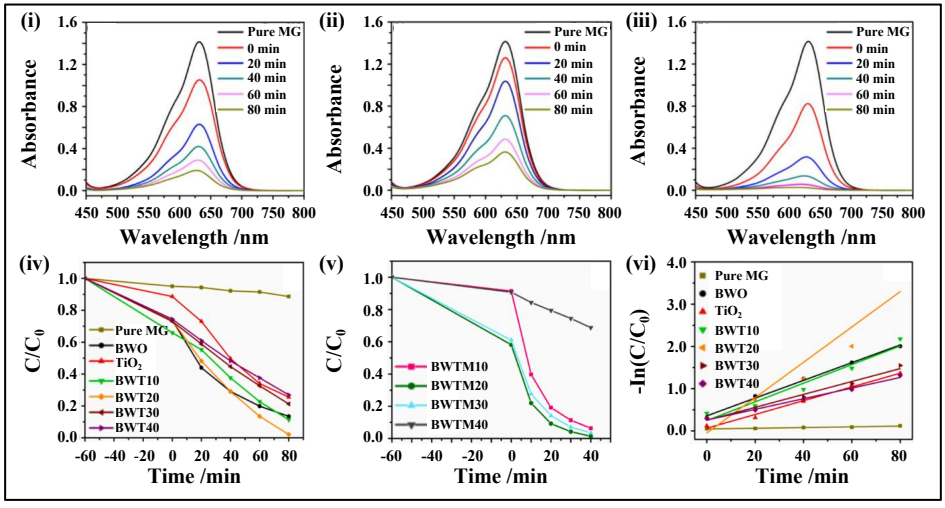
(i)
(ii)
(iii)
Absorbance
Wavelength /nm
Pure MG
0 min
20 min
40 min
60 min
80 min
(iv)
C/C0
Pure MG
BWO
TiO2
BWT10
BWT20
BWT30
BWT40
Time /min
(v)
C/C0
BWTM10
BWTM20
BWTM30
BWTM40
Time /min
(vi)
-ln(C/C0)
Pure MG
BWO
TiO2
BWT10
BWT20
BWT30
BWT40
Time /min

(b)

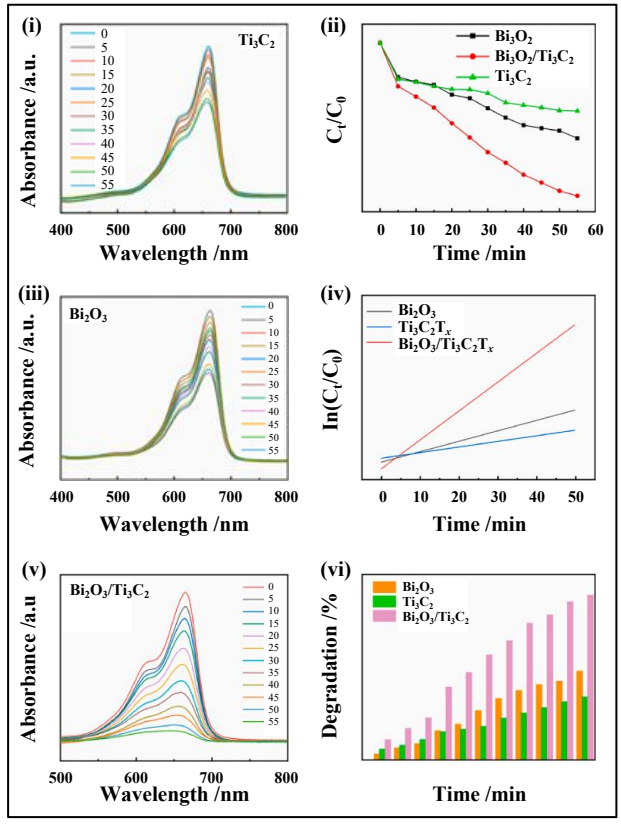
(i)
Ti3C2
Absorbance /a.u.
Wavelength /nm
(ii)
Bi2O3
Bi2O3/Ti3C2
Ti3C2
Ct/C0
Time /min
(iii)
Bi2O3
Absorbance /a.u.
Wavelength /nm
(iv)
Bi2O3
Ti3C2Tx
Bi2O3/Ti3C2Tx
ln(Ct/C0)
Time /min
(v)
Bi2O3/Ti3C2
Absorbance /a.u
Wavelength /nm
(vi)
Bi2O3
Ti3C2
Bi2O3/Ti3C2
Degradation /%
Time /min

(c)

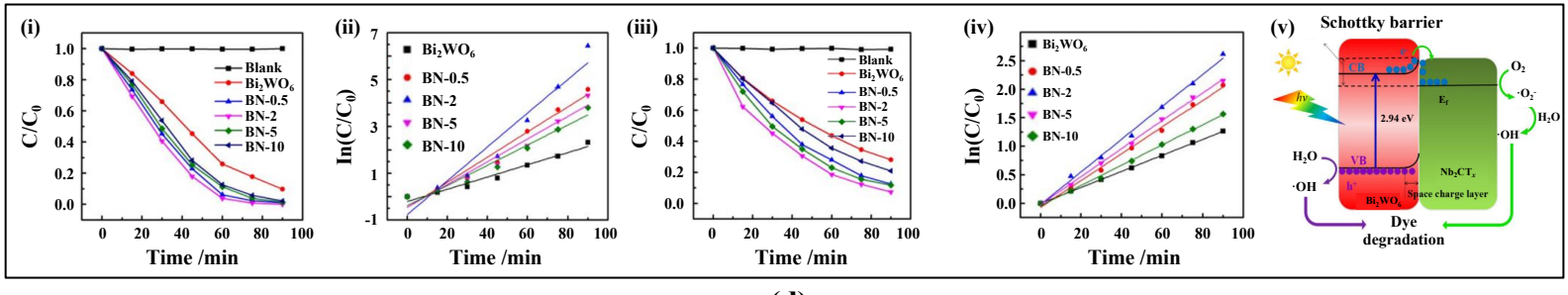
(i)
C/C0
Blank
Bi2WO6
BN-0.5
BN-2
BN-5
BN-10
Time /min
(ii)
ln(C/C0)
Bi2WO6
BN-0.5
BN-2
BN-5
BN-10
Time /min
(iii)
C/C0
Time /min
(iv)
ln(C/C0)
Time /min
(v)
Schottky barrier
CB
VB
2.94 eV
Ef
Nb2CTx
Bi2WO6
Space charge layer
O2
·O2-
H2O
·OH
Dye degradation

(d)

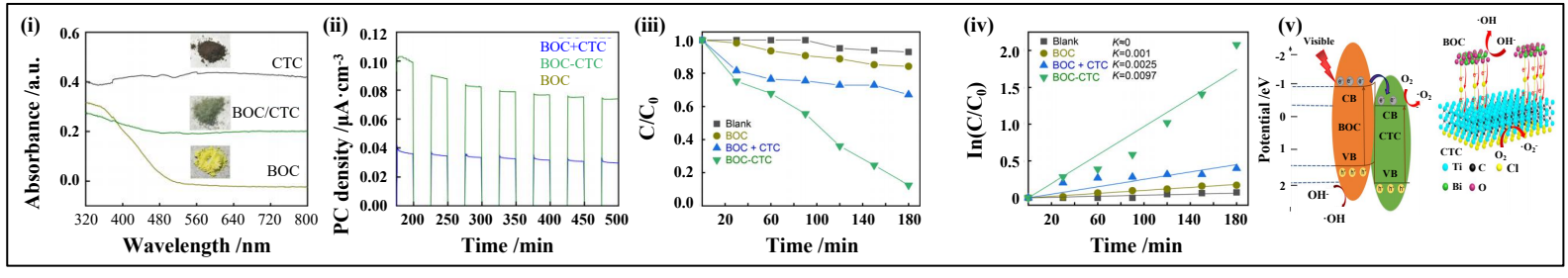
(i)
Absorbance /a.u.
CTC
BOC/CTC
BOC
Wavelength /nm
(ii)
PC density /μA·cm-2
BOC+CTC
BOC-CTC
BOC
Time /min
(iii)
C/C0
Blank
BOC
BOC + CTC
BOC-CTC
Time /min
(iv)
ln(C/C0)
Blank K=0
BOC K=0.001
BOC + CTC K=0.0025
BOC-CTC K=0.0097
Time /min
(v)
Potential /eV
Visible
CB
VB
BOC
CTC
O2
·O2-
OH-
·OH
Ti
C
Cl
Bi
O

(e)

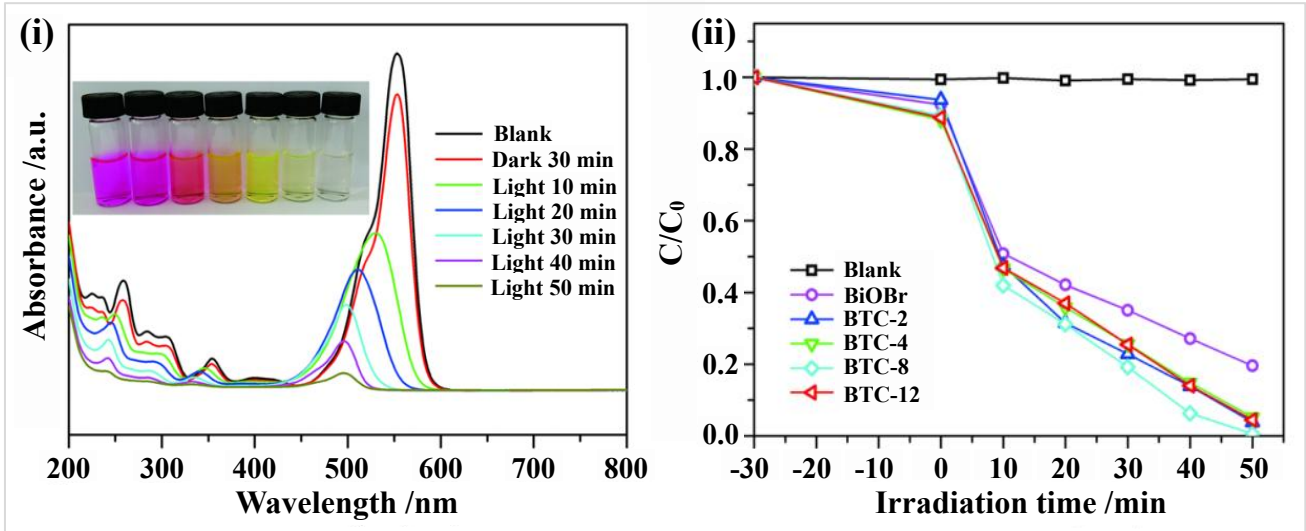
(i)
Absorbance /a.u.
Wavelength /nm
Blank
Dark 30 min
Light 10 min
Light 20 min
Light 30 min
Light 40 min
Light 50 min
(ii)
C/C0
Irradiation time /min
Blank
BiOBr
BTC-2
BTC-4
BTC-8
BTC-12

(a)

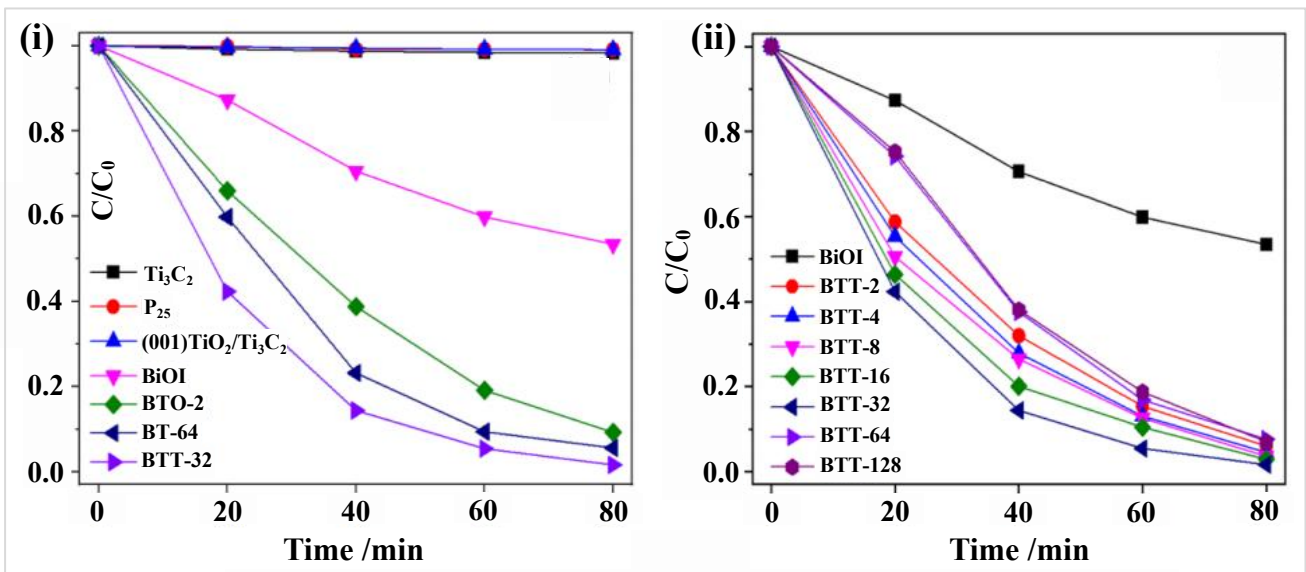
(i)
C/C0
Time /min
Ti3C2
P25
(001)TiO2/Ti3C2
BiOI
BTO-2
BT-64
BTT-32
(ii)
C/C0
Time /min
BiOI
BTT-2
BTT-4
BTT-8
BTT-16
BTT-32
BTT-64
BTT-128

(b)

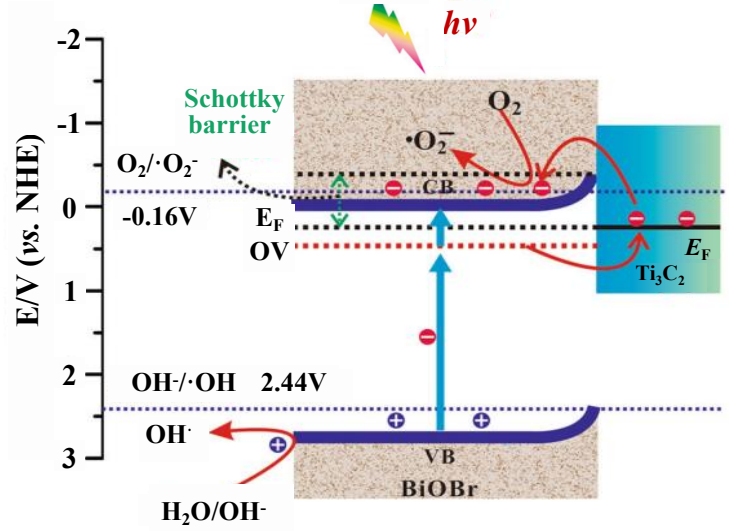
hv
Schottky barrier
O2
·O2−
O2/·O2-
-0.16V
EF
CB
OV
Ti3C2
OH-/·OH 2.44V
OH·
VB
BiOBr
H2O/OH-
E/V (vs. NHE)

(c)

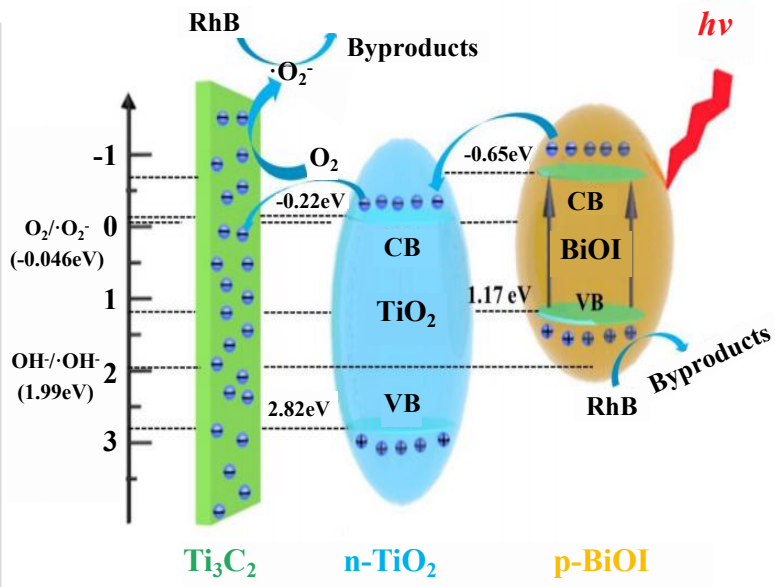
RhB
Byproducts
·O2-
O2
hv
-0.65eV
-0.22eV
CB
BiOI
O2/·O2-
(-0.046eV)
CB
TiO2
1.17 eV
VB
OH-/·OH-
(1.99eV)
2.82eV
VB
RhB
Byproducts
Ti3C2
n-TiO2
p-BiOI

(d)

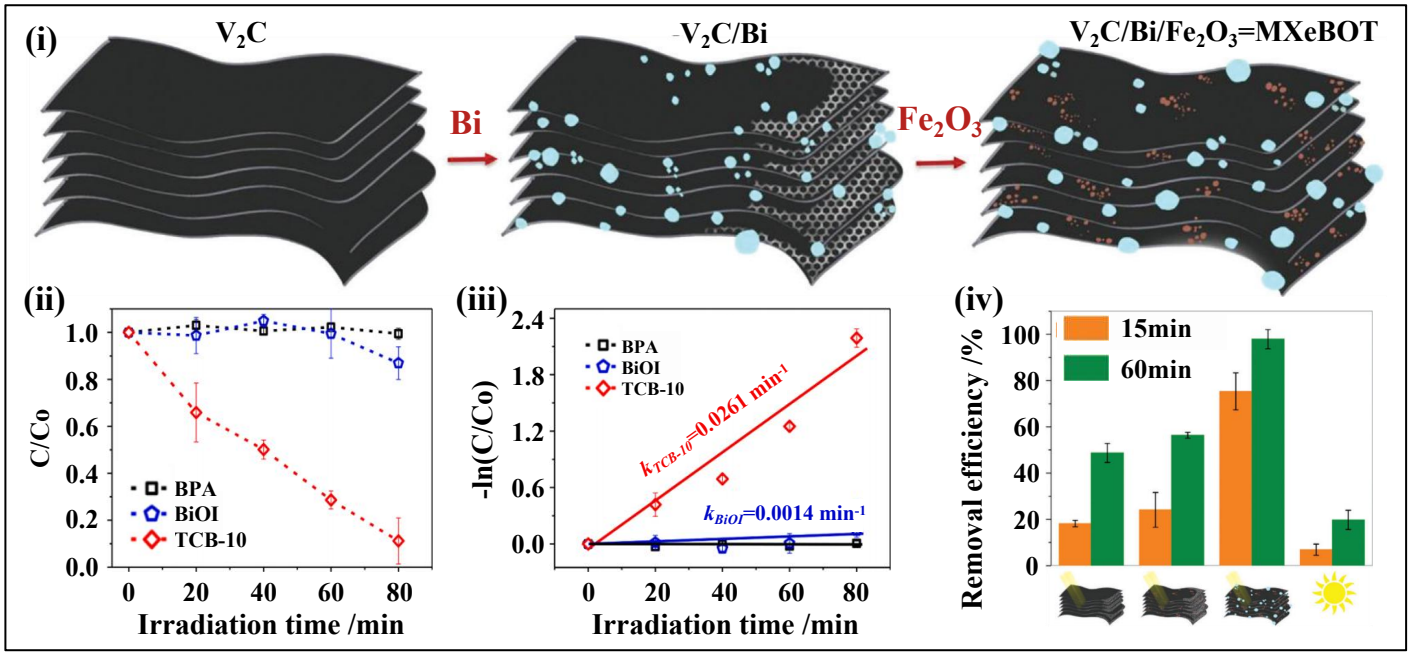
(i)
V2C
V2C/Bi
V2C/Bi/Fe2O3=MXeBOT
Bi
Fe2O3
(ii)
C/Co
BPA
BiOI
TCB-10
Irradiation time /min
(iii)
-ln(C/Co)
BPA
BiOI
TCB-10
kTCB-10=0.0261 min-1
kBiOI=0.0014 min-1
Irradiation time /min
(iv)
Removal efficiency /%
15min
60min

(a)

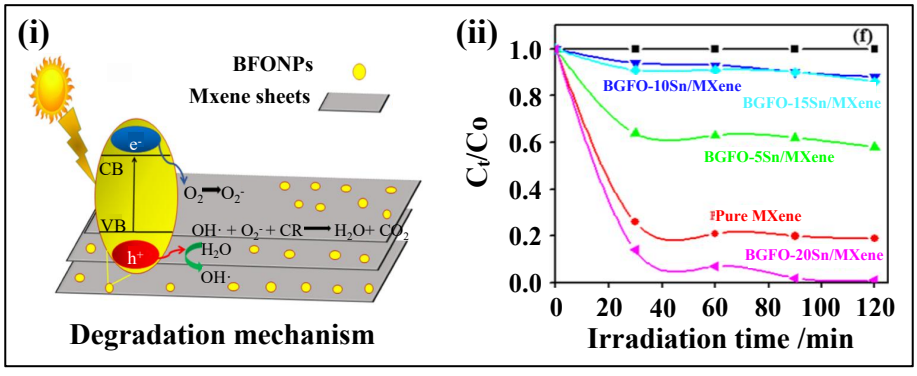
(i)
BFONPs
Mxene sheets
CB
VB
e-
h+
O2→O2-
OH· + O2- + CR → H2O + CO2
H2O
OH·
Degradation mechanism
(ii)
Ct/Co
BGFO-10Sn/MXene
BGFO-15Sn/MXene
BGFO-5Sn/MXene
Pure MXene
BGFO-20Sn/MXene
Irradiation time /min

(b)

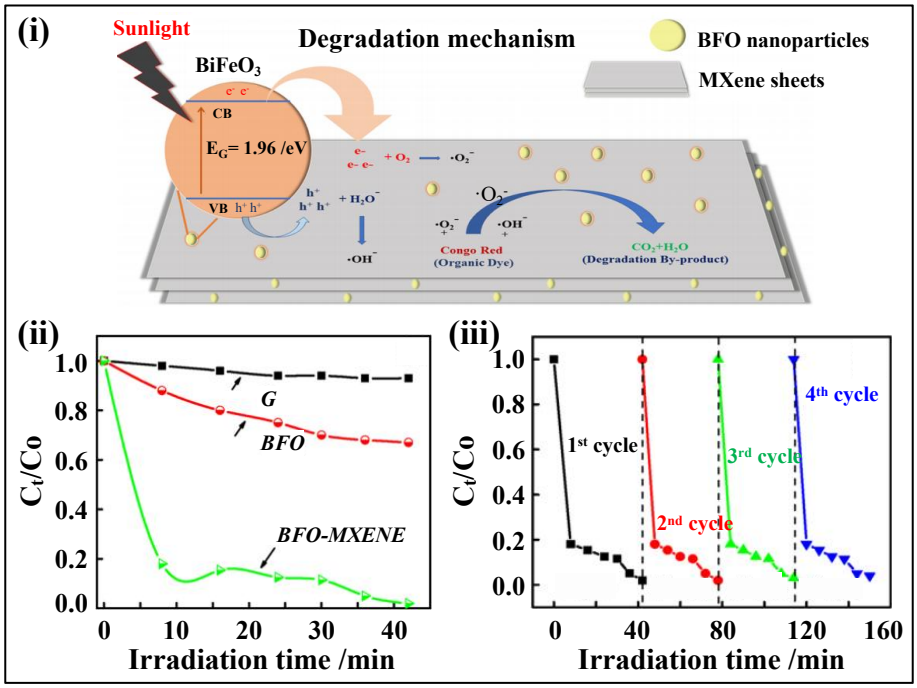
(i)
Sunlight
Degradation mechanism
BFO nanoparticles
MXene sheets
BiFeO3
CB
EG= 1.96 /eV
VB
Congo Red
(Organic Dye)
CO2+H2O
(Degradation By-product)
(ii)
Ct/Co
G
BFO
BFO-MXENE
Irradiation time /min
(iii)
Ct/Co
1st cycle
2nd cycle
3rd cycle
4th cycle
Irradiation time /min

(c)

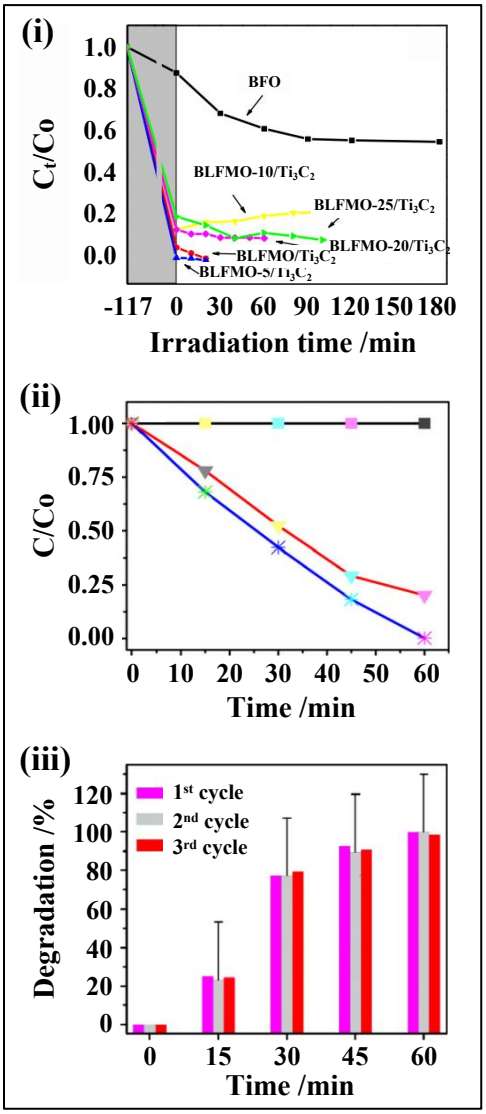
(i)
Ct/Co
BFO
BLFMO-10/Ti3C2
BLFMO-25/Ti3C2
BLFMO-20/Ti3C2
BLFMO/Ti3C2
BLFMO-5/Ti3C2
Irradiation time /min
(ii)
C/Co
Time /min
(iii)
Degradation /%
1st cycle
2nd cycle
3rd cycle
Time /min

(d)

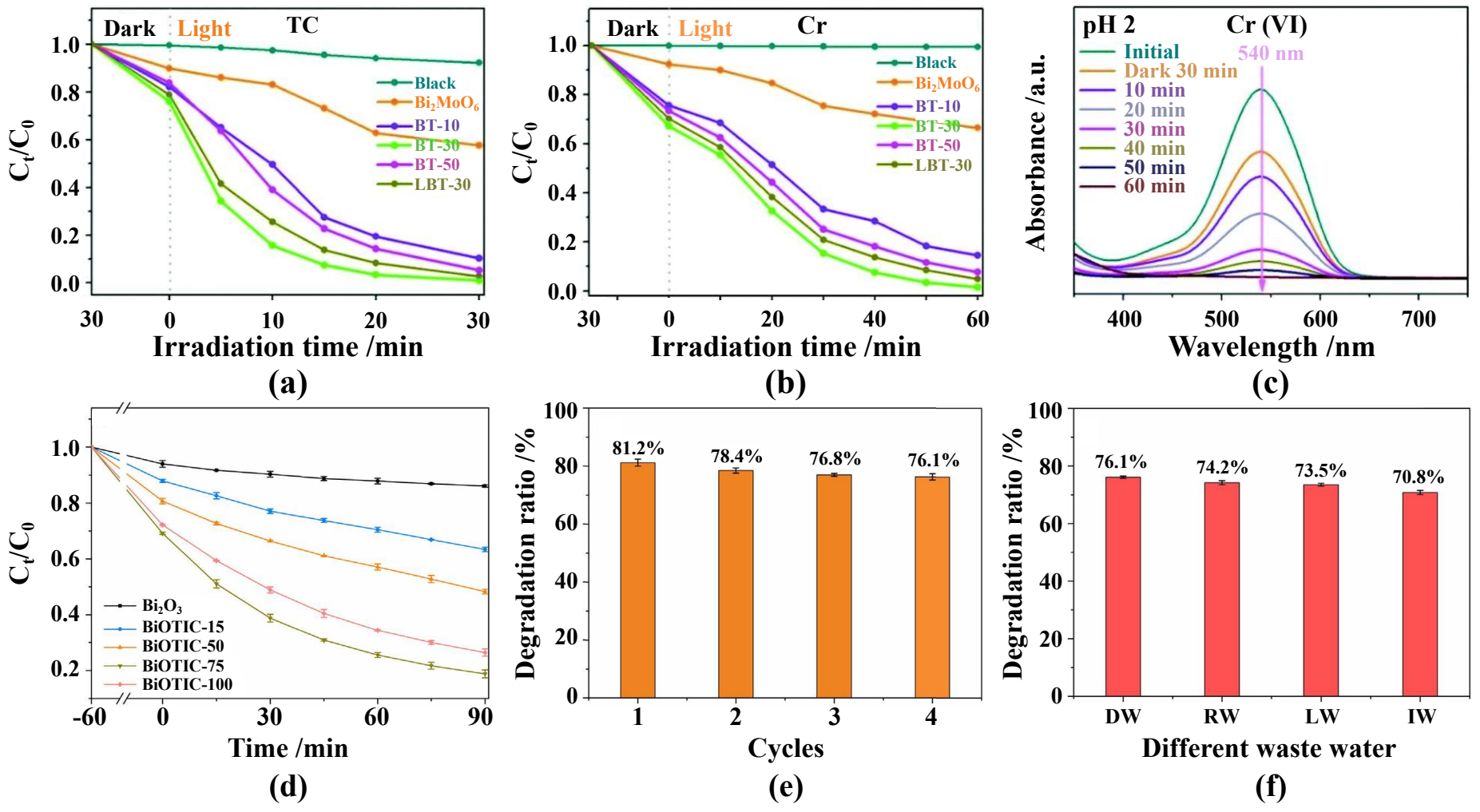
Dark
Light
TC
Black
Bi2MoO6
BT-10
BT-30
BT-50
LBT-30
Ct/C0
Irradiation time /min
(a)
Dark
Light
Cr
Black
Bi2MoO6
BT-10
BT-30
BT-50
LBT-30
Ct/C0
Irradiation time /min
(b)
pH 2
Cr (VI)
Initial
Dark 30 min
10 min
20 min
30 min
40 min
50 min
60 min
540 nm
Absorbance /a.u.
Wavelength /nm
(c)
Bi2O3
BiOTIC-15
BiOTIC-50
BiOTIC-75
BiOTIC-100
Ct/C0
Time /min
(d)
81.2%
78.4%
76.8%
76.1%
Degradation ratio /%
Cycles
(e)
76.1%
74.2%
73.5%
70.8%
Degradation ratio /%
DW
RW
LW
IW
Different waste water
(f)

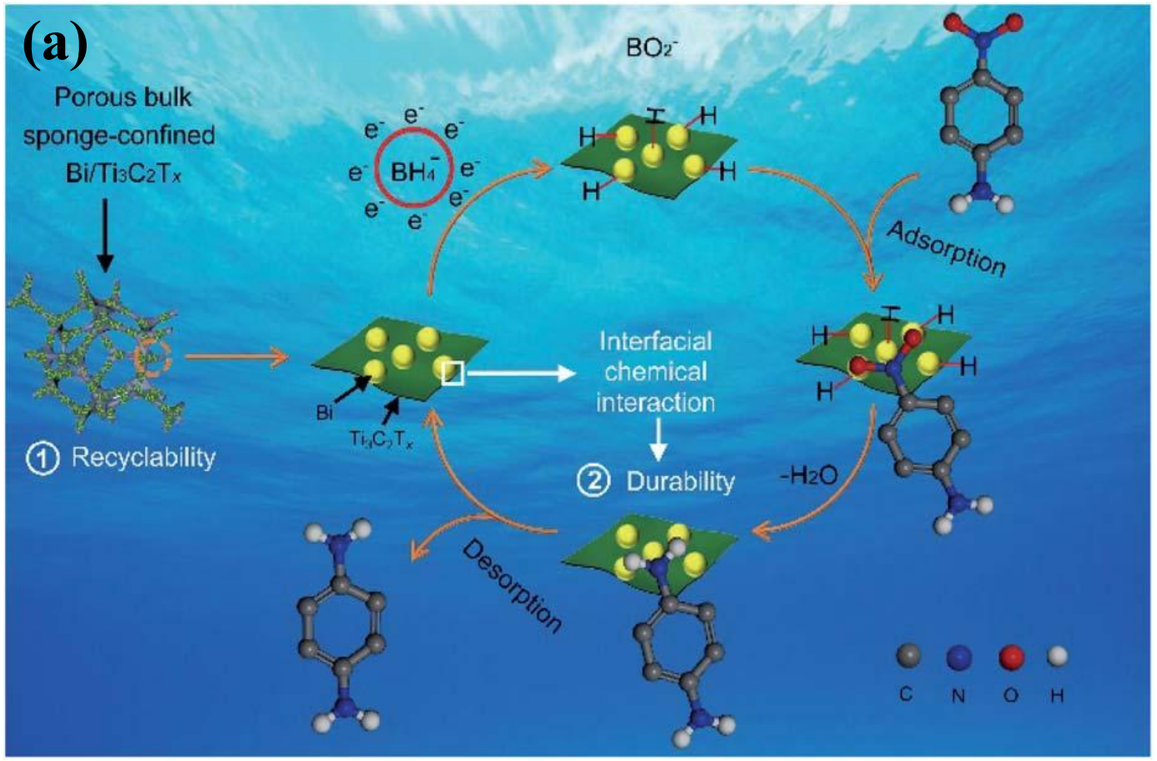
(a)
Porous bulk
sponge-confined
Bi/Ti3C2Tx
BO2-
BH4-
e-
H
Adsorption
Bi
Ti3C2Tx
① Recyclability
Interfacial
chemical
interaction
② Durability
-H2O
Desorption
C
N
O
H

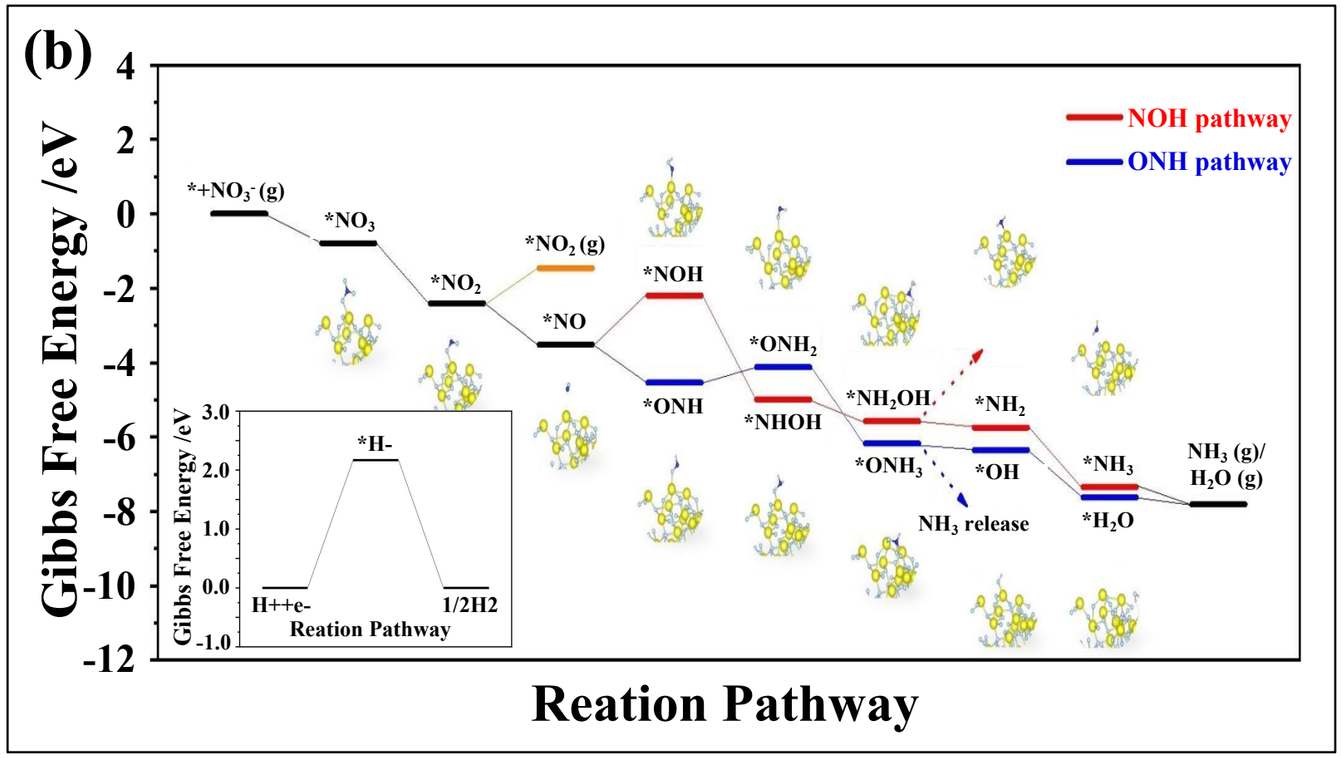
(b)
Gibbs Free Energy /eV
Reation Pathway
NOH pathway
ONH pathway
*+NO3- (g)
*NO3
*NO2
*NO2 (g)
*NO
*NOH
*ONH
*ONH2
*NHOH
*NH2OH
*ONH3
NH3 release
*NH2
*OH
*NH3
*H2O
NH3 (g)/
H2O (g)
Gibbs Free Energy /eV
*H-
H++e-
1/2H2
Reation Pathway

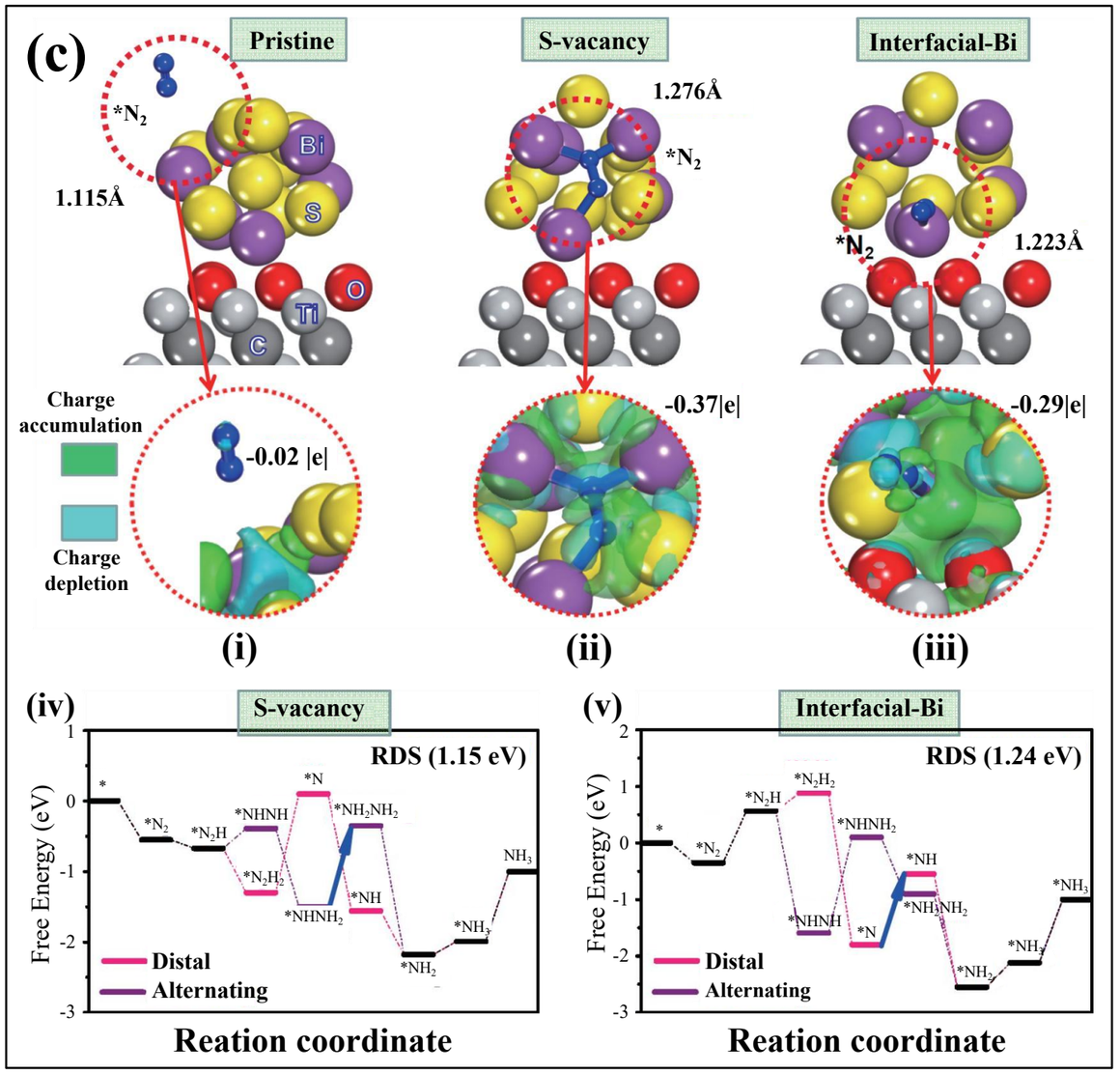
(c)
Pristine
S-vacancy
Interfacial-Bi
*N2
1.115Å
1.276Å
1.223Å
Bi
S
Ti
O
C
Charge
accumulation
Charge
depletion
-0.02 |e|
-0.37|e|
-0.29|e|
(i)
(ii)
(iii)
(iv)
S-vacancy
RDS (1.15 eV)
Free Energy (eV)
Distal
Alternating
Reation coordinate
(v)
Interfacial-Bi
RDS (1.24 eV)
Free Energy (eV)
Distal
Alternating
Reation coordinate

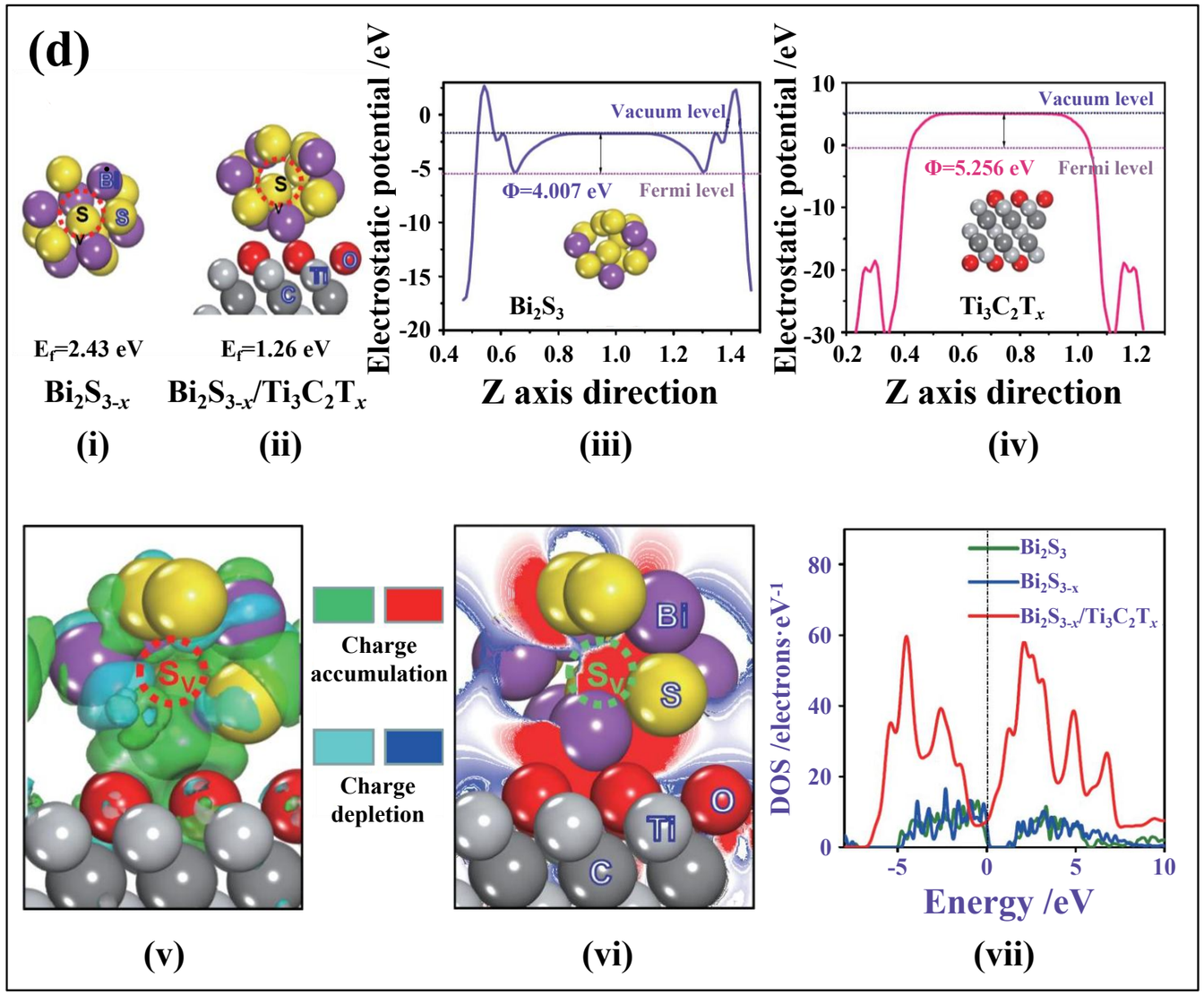
(d)
Bi
S
Sv
Ti
O
C
Ef=2.43 eV
Bi2S3-x
(i)
Ef=1.26 eV
Bi2S3-x/Ti3C2Tx
(ii)
Electrostatic potential /eV
Vacuum level
Φ=4.007 eV
Fermi level
Bi2S3
Z axis direction
(iii)
Vacuum level
Φ=5.256 eV
Fermi level
Ti3C2Tx
Z axis direction
(iv)
Charge
accumulation
Charge
depletion
(v)
(vi)
Bi2S3
Bi2S3-x
Bi2S3-x/Ti3C2Tx
DOS /electrons·eV-1
Energy /eV
(vii)

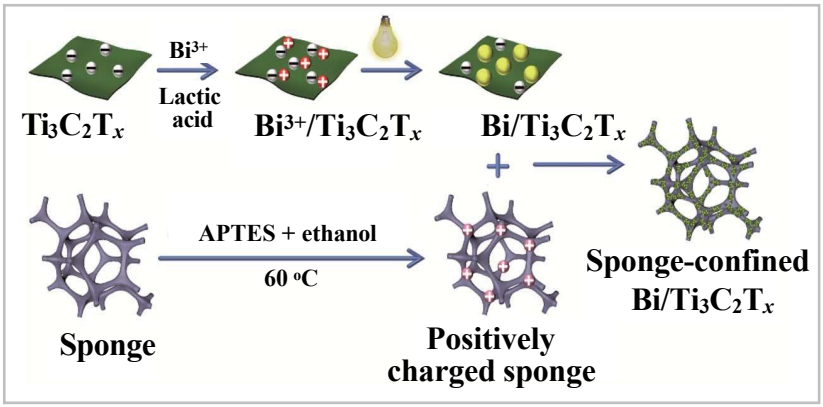
Bi3+
Lactic acid
Ti3C2Tx
Bi3+/Ti3C2Tx
Bi/Ti3C2Tx
APTES + ethanol
60 °C
Sponge
Positively charged sponge
Sponge-confined Bi/Ti3C2Tx

(a)

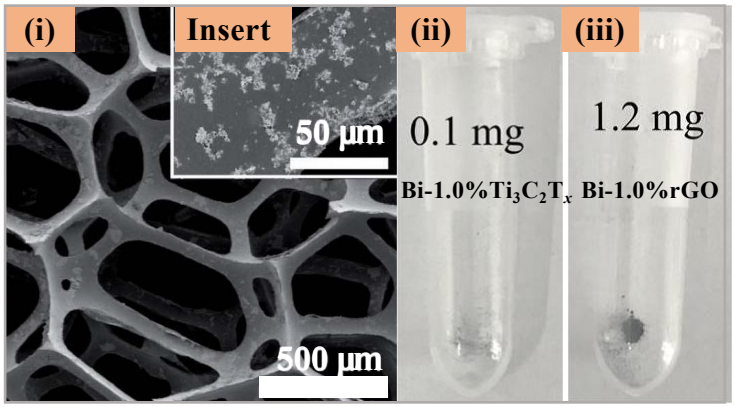
(i)
Insert
50 μm
500 μm
(ii)
0.1 mg
Bi-1.0%Ti3C2Tx
(iii)
1.2 mg
Bi-1.0%rGO

(b)

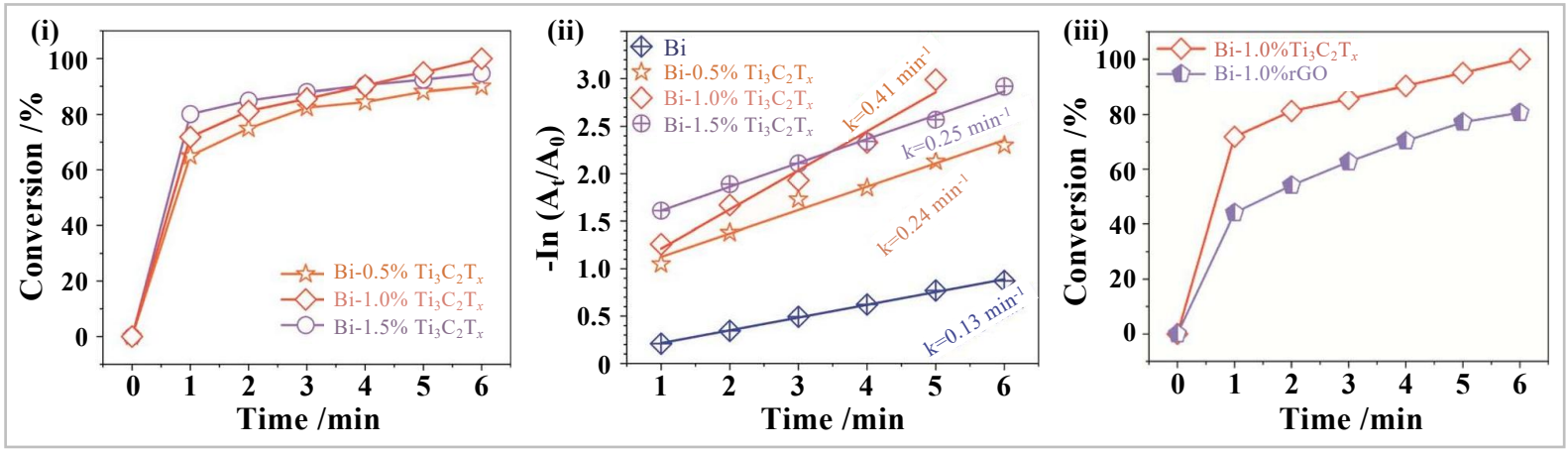
(i)
Conversion /%
Time /min
Bi-0.5% Ti3C2Tx
Bi-1.0% Ti3C2Tx
Bi-1.5% Ti3C2Tx
(ii)
-ln (At/A0)
Bi
k=0.41 min-1
k=0.25 min-1
k=0.24 min-1
k=0.13 min-1
(iii)
Bi-1.0%Ti3C2Tx
Bi-1.0%rGO

(c)

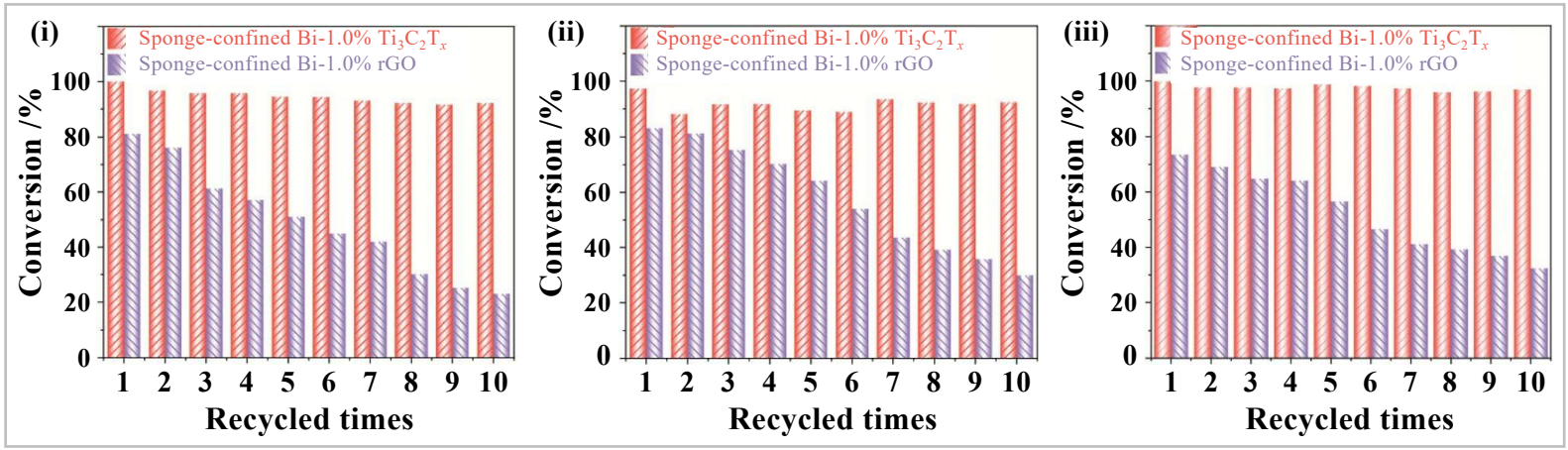
(i)
Sponge-confined Bi-1.0% Ti3C2Tx
Sponge-confined Bi-1.0% rGO
Conversion /%
Recycled times
(ii)
(iii)

(d)

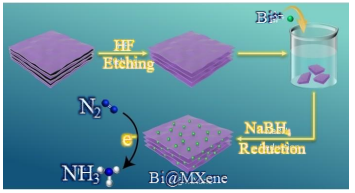
HF
Etching
Bi3+
NaBH4
Reduction
N2
e-
NH3
Bi@MXene

(a)

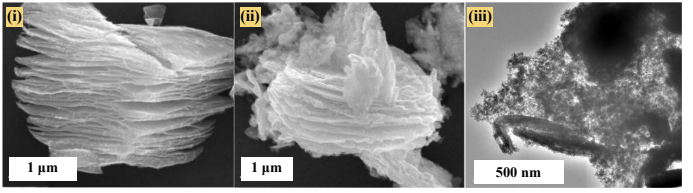
(i)
1 μm
(ii)
1 μm
(iii)
500 nm

(b)

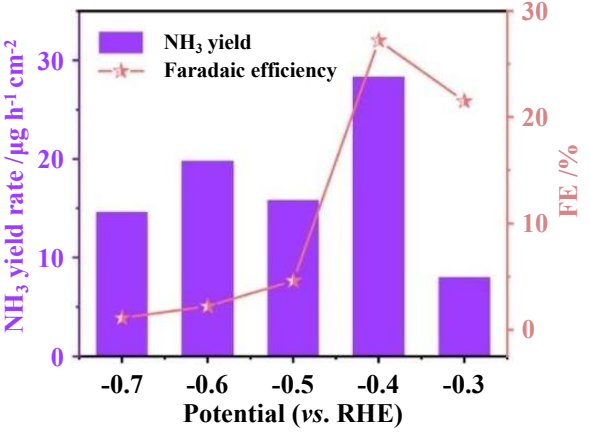
NH3 yield
Faradaic efficiency
NH3 yield rate /μg h-1 cm-2
FE /%
0
10
20
30
0
10
20
30
-0.7
-0.6
-0.5
-0.4
-0.3
Potential (vs. RHE)

(c)

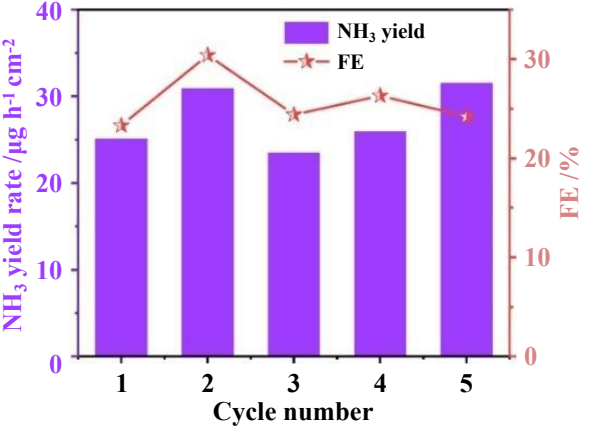
NH3 yield
FE
NH3 yield rate /μg h-1 cm-2
FE /%
0
10
20
30
40
0
10
20
30
1
2
3
4
5
Cycle number

(d)

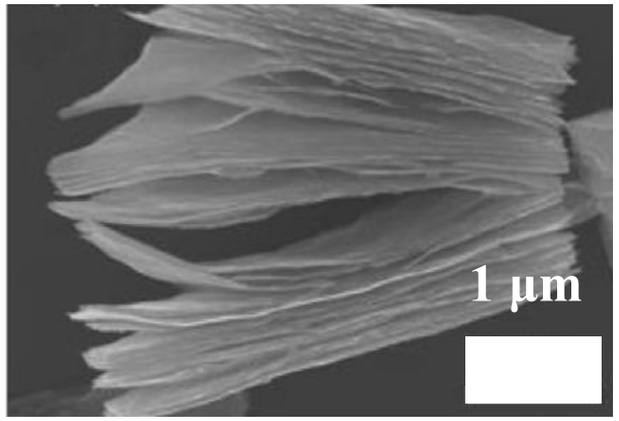

$Ti_3C_2T_x$

(a)

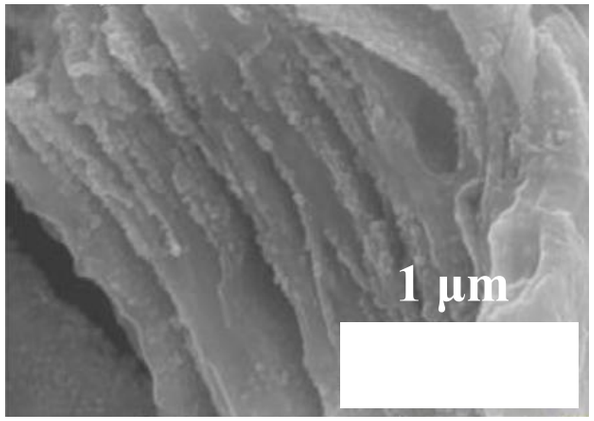

$Ti_3C_2T_x$/BiOCl

(b)

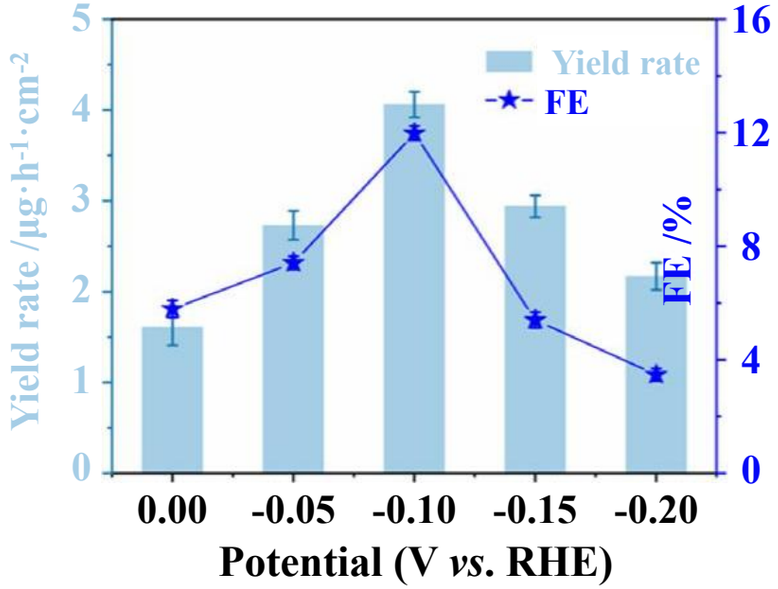

(c)

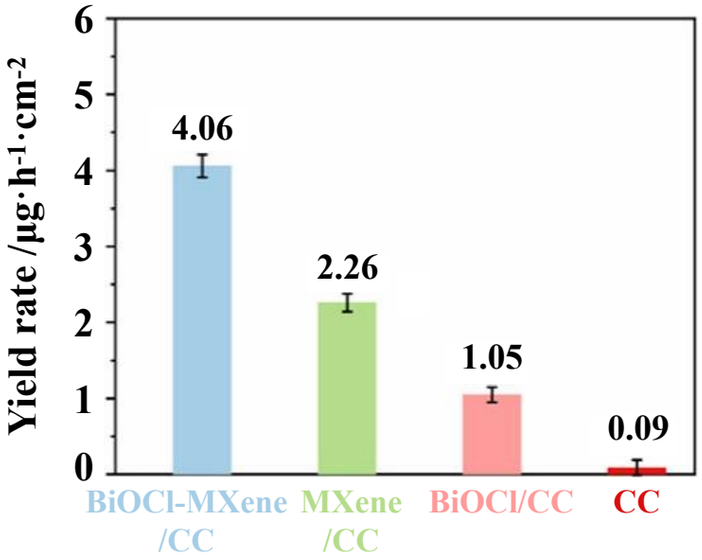

(d)

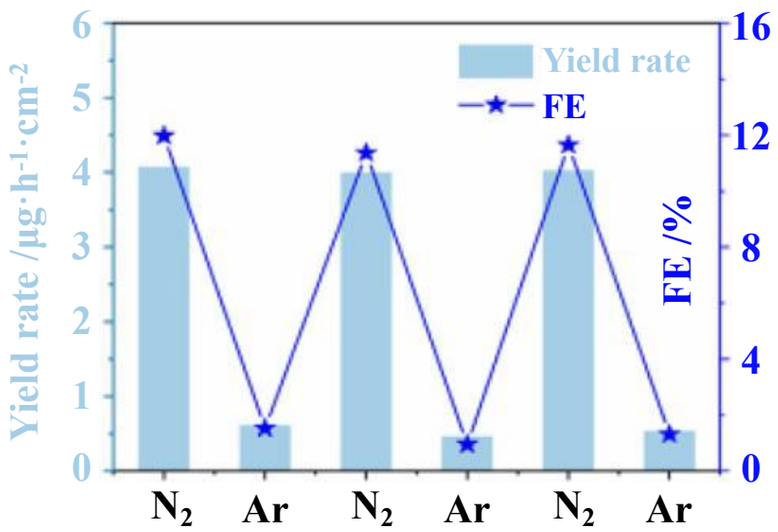

(e)

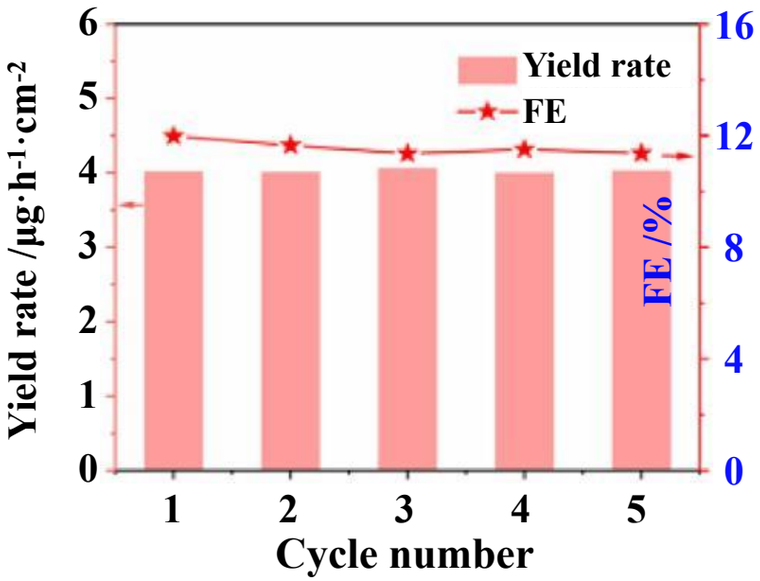

(f)

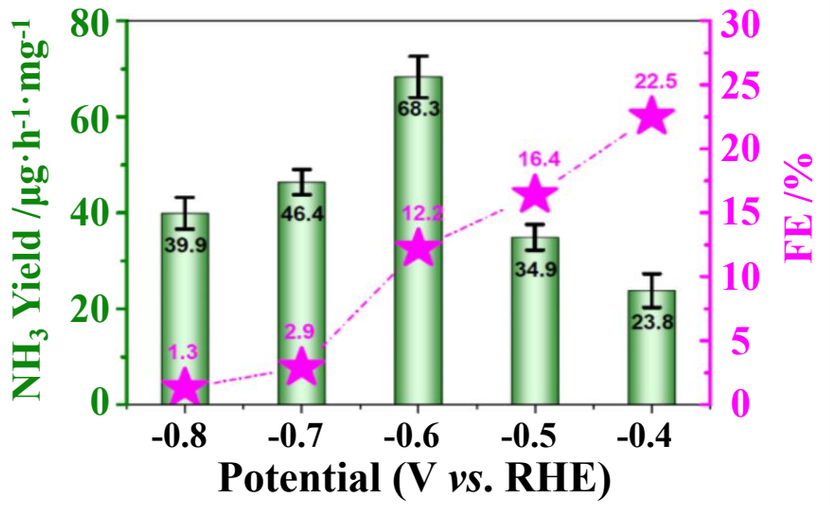

(g)

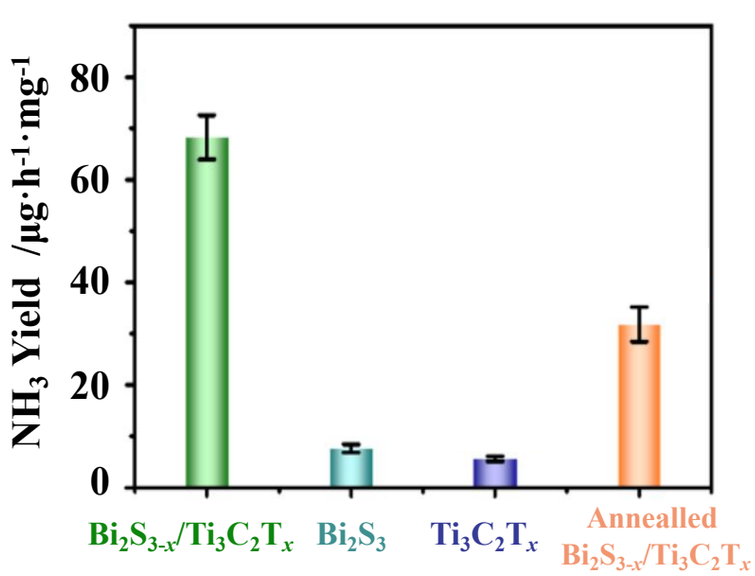

(h)

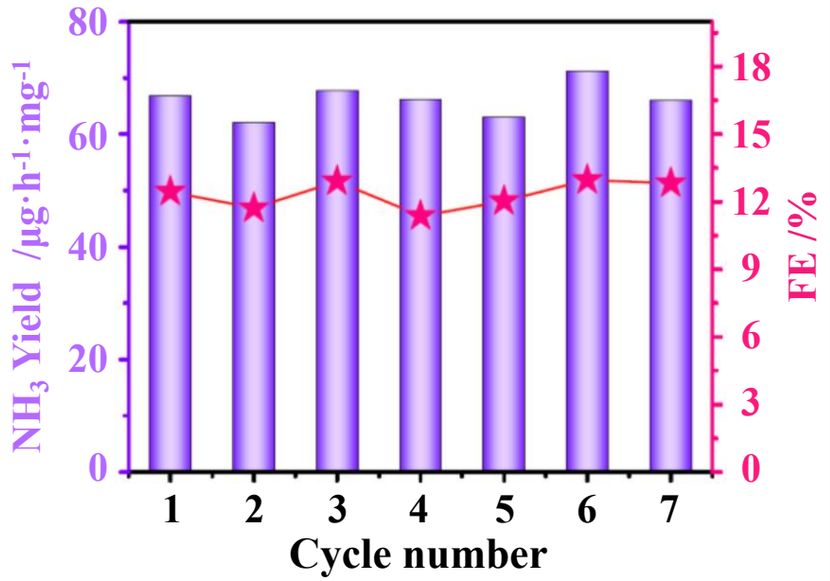

(i)

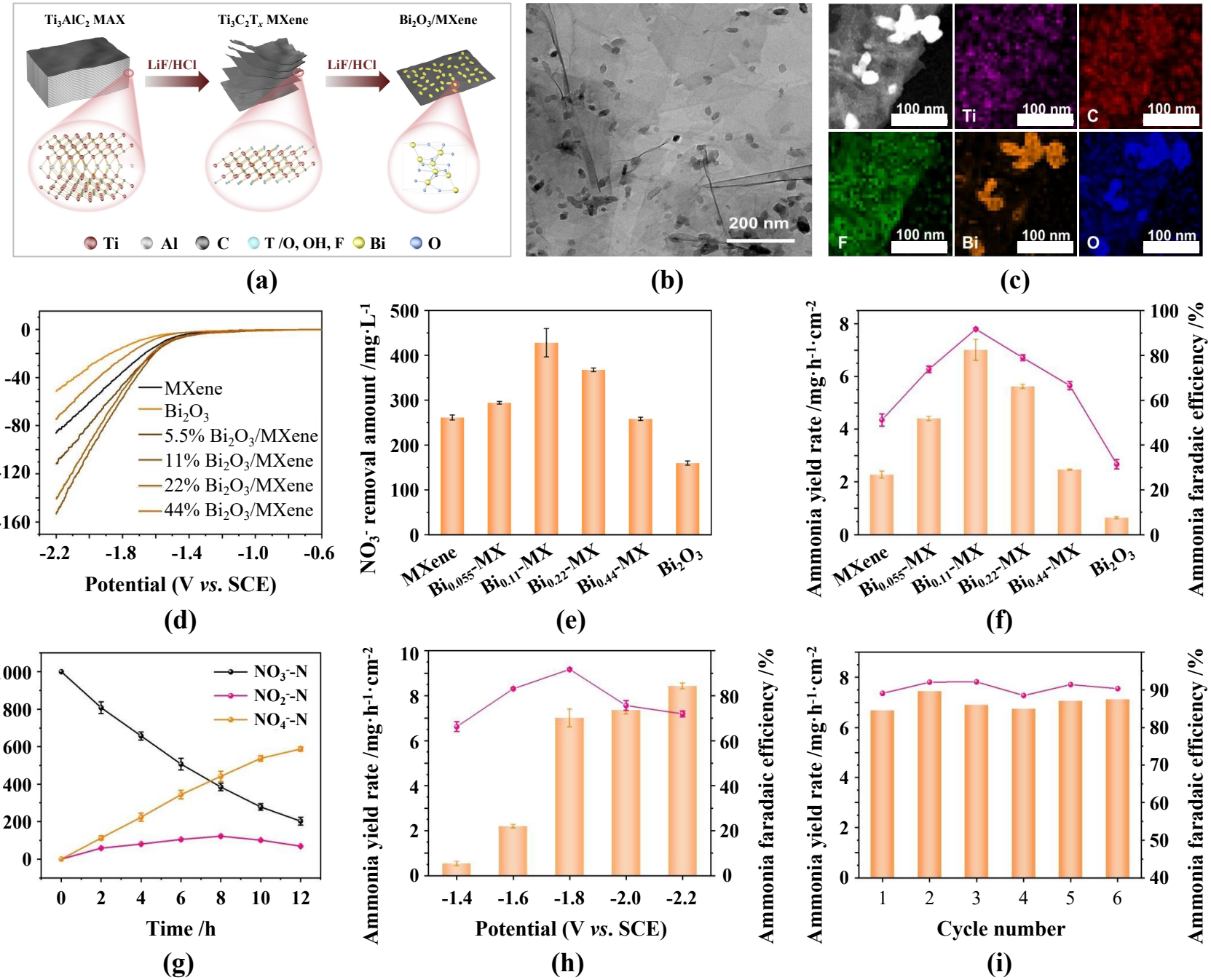
Ti3AlC2 MAX
Ti3C2Tx MXene
Bi2O3/MXene
LiF/HCl
LiF/HCl
Ti
Al
C
T /O, OH, F
Bi
O
(a)
200 nm
(b)
100 nm
Ti
C
F
Bi
O
(c)
j /mA·Cm-2
MXene
Bi2O3
5.5% Bi2O3/MXene
11% Bi2O3/MXene
22% Bi2O3/MXene
44% Bi2O3/MXene
Potential (V vs. SCE)
(d)
NO3- removal amount /mg·L-1
MXene
Bi0.055-MX
Bi0.11-MX
Bi0.22-MX
Bi0.44-MX
Bi2O3
(e)
Ammonia yield rate /mg·h-1·cm-2
Ammonia faradaic efficiency /%
(f)
Concentration /mg·L
NO3--N
NO2--N
NO4--N
Time /h
(g)
Potential (V vs. SCE)
(h)
Cycle number
(i)

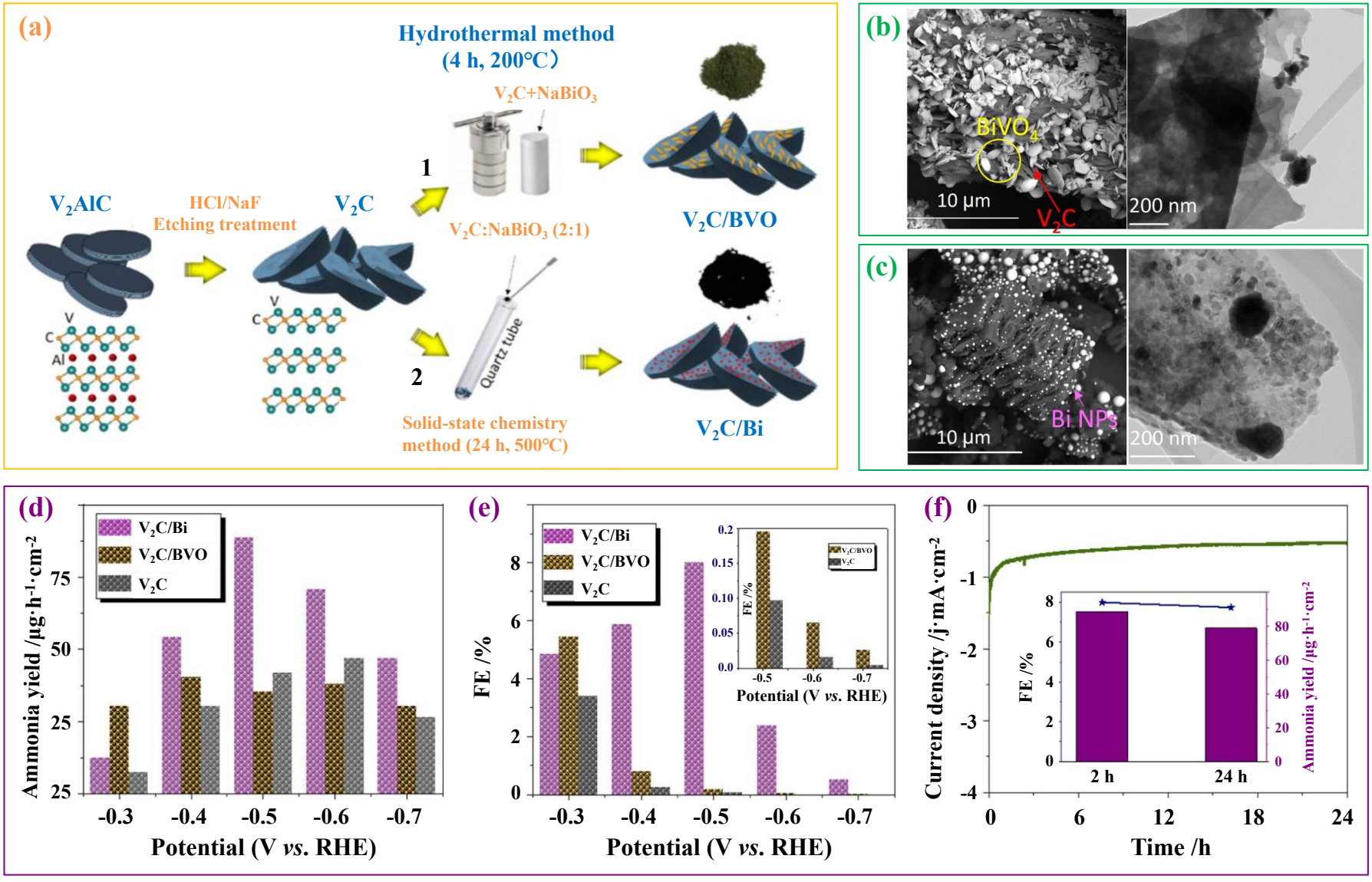
(a)
Hydrothermal method
(4 h, 200℃)
V2C+NaBiO3
1
V2AlC
HCl/NaF
Etching treatment
V2C
V2C:NaBiO3 (2:1)
V2C/BVO
2
Quartz tube
Solid-state chemistry
method (24 h, 500℃)
V2C/Bi
(b)
BiVO4
10 μm
V2C
200 nm
(c)
10 μm
Bi NPs
200 nm
(d)
V2C/Bi
V2C/BVO
V2C
Ammonia yield /μg·h-1·cm-2
Potential (V vs. RHE)
(e)
V2C/Bi
V2C/BVO
V2C
FE /%
Potential (V vs. RHE)
(f)
Current density /j·mA·cm-2
Time /h
FE /%
Ammonia yield /μg·h-1·cm-2
2 h
24 h

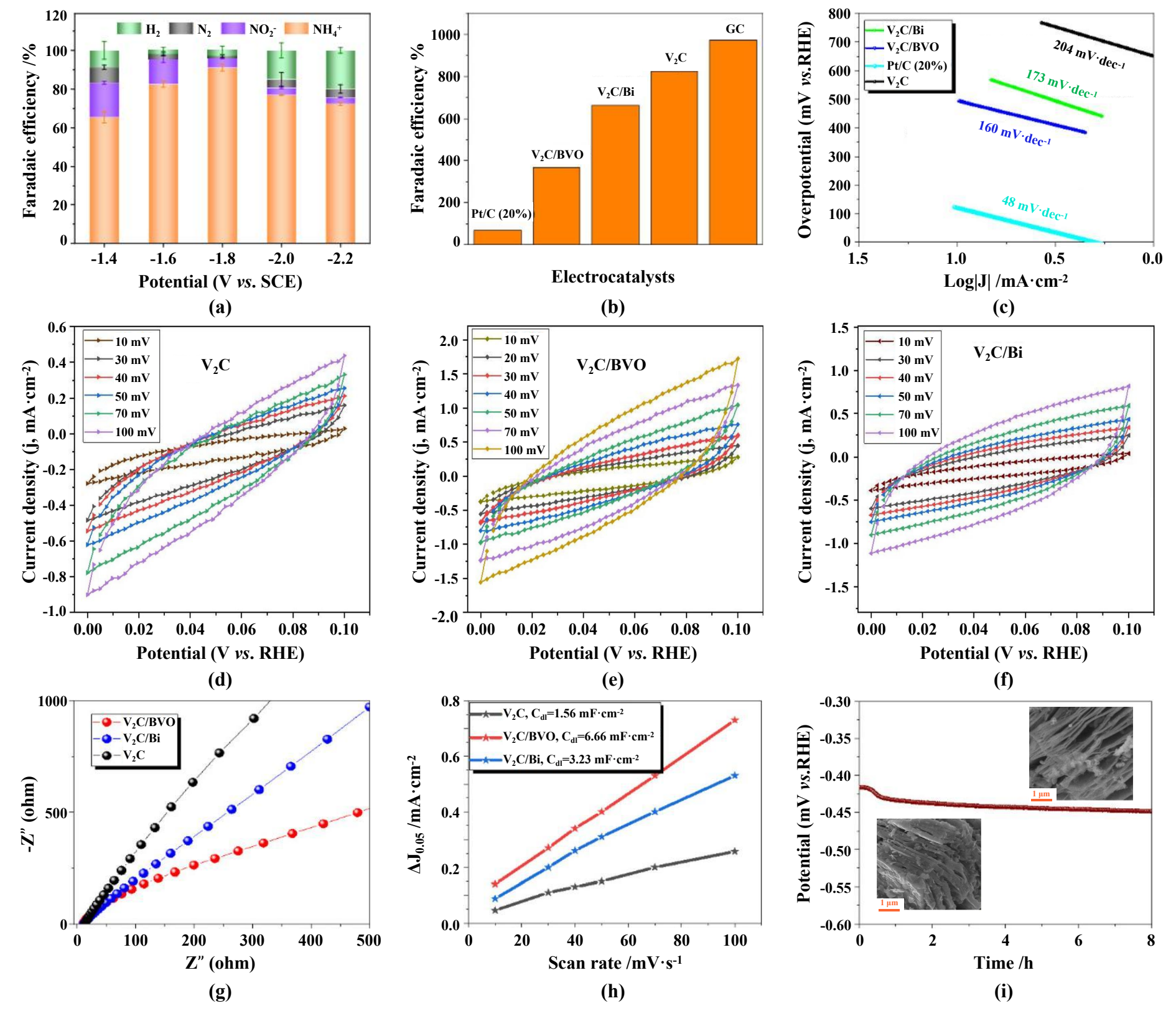
Faradaic efficiency /%
H2
N2
NO2-
NH4+
Potential (V vs. SCE)
(a)
Faradaic efficiency %
Pt/C (20%)
V2C/BVO
V2C/Bi
V2C
GC
Electrocatalysts
(b)
Overpotential (mV vs.RHE)
V2C/Bi
V2C/BVO
Pt/C (20%)
V2C
204 mV·dec-1
173 mV·dec-1
160 mV·dec-1
48 mV·dec-1
Log|J| /mA·cm-2
(c)
Current density (j, mA·cm-2)
V2C
10 mV
30 mV
40 mV
50 mV
70 mV
100 mV
Potential (V vs. RHE)
(d)
V2C/BVO
20 mV
(e)
V2C/Bi
(f)
-Z'' (ohm)
Z'' (ohm)
(g)
ΔJ0.05 /mA·cm-2
V2C, Cdl=1.56 mF·cm-2
V2C/BVO, Cdl=6.66 mF·cm-2
V2C/Bi, Cdl=3.23 mF·cm-2
Scan rate /mV·s-1
(h)
Potential (mV vs.RHE)
1 μm
Time /h
(i)